Title

Efficient Terahertz Transmitters and Receivers in Silicon for Broadband Sensing and High-Speed Wireless Communication

Permalink

https://escholarship.org/uc/item/5jg5j61h

Author

Razavian, Seyedmohammadreza

Publication Date

2022

Peer reviewed|Thesis/dissertation

UNIVERSITY OF CALIFORNIA
Los Angeles

Efficient Terahertz Transmitters and Receivers in Silicon for Broadband Sensing and High-Speed Wireless Communication

A dissertation submitted in partial satisfaction
of the requirements for the degree
Doctor of Philosophy in Electrical and Computer Engineering

by

Seyedmohammadreza Razavian

2022

ABSTRACT OF THE DISSERTATION

Efficient Terahertz Transmitters and Receivers in Silicon for Broadband Sensing and High-Speed Wireless Communication

by

Seyedmohammadreza Razavian
Doctor of Philosophy in Electrical and Computer Engineering
University of California, Los Angeles, 2022
Professor Aydin Babakhani, Chair

With the emergence of new IOT and mobile applications, there has been an ever-increasing demand for high-data-rate wireless communication and high-resolution sensing. Researchers have put an extensive effort to push the operating frequency of the communication and sensing systems. Sub-Terahertz (Sub-THz) band offers a wide unlicensed bandwidth that plays a critical role in the realization of high-speed wireless communication links. In addition, THz waves benefit from short wavelengths putting them at advantage compared to lower frequency bands for sensing and short-range high-resolution radars.

Considering that current commercial THz systems are costly and bulky, developing these systems in standard silicon technologies is vital to lower the cost. In addition, this enables the integration of THz systems with other circuit blocks to implement a compact solution. THz generation in standard silicon technologies faces various challenges, including the limited speed of transistors. Since conventional techniques in the RF domain are not practical in the THz band, researchers have proposed new techniques to tackle the limitations of THz generation in silicon. Despite recent advancements, state-of-the-art THz systems still suffer from low efficiency and low radiated power.

This study proposes a novel technique based on PIN diode reverse recovery to improve the power, bandwidth, and efficiency of the generated THz waves. Using the concept of reverse recovery, a PIN-diode-based pulse radiator is introduced that generates pulses with 1.7-ps Full Width at Half Maximum (FWHM). In the frequency domain, the generated pulses correspond to a frequency comb. The tones of the frequency comb are received using a harmonic mixer in the frequency range 220-1125 GHz. On the receiver side, a low-power heterodyne frequency comb receiver using Schottky Barrier Diode (SBD) is demonstrated. The receiver is used in conjunction with the broadband pulse radiator to implement a dual-comb spectroscopy system operating up to 550 GHz. By extending the idea of PIN reverse recovery into Continuous-Wave (CW) domain, a PIN diode-based CW 2×3 array source is designed that radiates at 430 GHz with 18.1-dBm Effective Isotropic Radiated Power (EIRP). Finally, the custom-built THz chips are employed for different applications, including micro-Doppler sensing of sound vibrations, long-distance THz communication, plasma physics characterization, imaging, and gas spectroscopy.

My research on THz circuit design and techniques has resulted in innovations and advancements in THz field by introducing new techniques for broadband efficient THz generation in low-cost silicon technologies. The proposed techniques pave the way for utilizing THz systems for different applications in applied physics, healthcare, and networks.

The dissertation of Seyedmohammadreza Razavian is approved.

Gregory J. Pottie

Yuanxun Ethan Wang

Danijela Cabric

Aydin Babakhani, Committee Chair

University of California, Los Angeles

2022

To My Family . . .

TABLE OF CONTENTS

LIST OF FIGURES

LIST OF TABLES

ACKNOWLEDGMENTS

I would like to express my gratitude to those who supported me during this long amazing journey and made this chapter of my life unforgettable.

Firstly, I would like to thank my wonderful advisor, Professor Aydin Babakhani, for providing me with valuable knowledge and experience. Not only has he been a professional advisor, but also his support as an understanding friend will never be forgotten. I have obtained various skills under his supervision, which will certainly pave the way for success in my future career.

Also, I should thank Professor Danijela Cabric, Professor Yuanxun Ethan Wang, and Professor Greg Pottie for serving on my Ph.D. defense committee and providing feedback to further improve the quality of my dissertation and research. Their comments have greatly helped me in preparing this thesis.

During my graduate studies at UCLA, I took various courses that gave me a unique profound experience and knowledge in the field of electrical engineering, especially RF and analog design. The knowledge that I obtained will play an important role in my professional life and will help me contribute more to this intriguing field of engineering. I thank Professors Asad Abidi, Bahram Jalali, Shervin Moloudi, Hooman Darabi, Behzad Razavi for their comprehensive courses and the wonderful learning experience.

Moreover, in my research, I am fortunate to have collaborated with Jia Han, Patrick Pribyl, and Walter Gekelman on utilizing THz radiator chips for the plasma characterization project.

I am grateful for having amazing co-members during my Ph.D. studies at UCLA Integrated Sensors Laboratory. I thank Mahdi Assefzadeh, Babak Jamali, Hamed Rahmani, Jaeeun Jang, Mahdi Forghani, Mostafa Hosseini, Yash Mehta, Sidharth Thomas, Hongming Lyu, Hanni Alhowri, and Arkaprova Ray for their support in research and also for being wonderful friends over all these years. I especially should thank Mahdi Assefzadeh and Babak

Jamali for helping me in the early stages of my research.

Most of all, I thank my family, Sassan, Fariba, and Salar. My family has played an important role in this path and to become who I am today by being patient and supporting me in every way possible. Although I have not seen them for years, it is difficult to put my gratitude for them in words and impossible to return their favor and kindness. Moreover, I should thank Armine Ter-Avetysian for being an amazing friend and always persuading me through my path.

VITA

2016	B.Sc. in Electrical Engineering Sharif University of Technology, Tehran, Iran.
2016	Rice Electrical and Computer Engineering Fellowship Rice University, Houston, TX.
2016–2017	Graduate Research Assistant Rice University, Houston, TX.
2019	M.Sc. in Electrical Engineering University of California, Los Angeles.
2019	Advanced to PhD Candidacy University of California, Los Angeles.
2020	RFIC Design Engineering Intern Qualcomm Technologies, Inc., San Jose, California.
2021	RFIC Design Engineering Intern Qualcomm Technologies, Inc., San Jose, California.
2021	IEEE SSCS Predoctoral Achievement Award University of California, Los Angeles.
2022	Microwave Theory and Techniques Society Graduate Fellowship University of California, Los Angeles.
2018–2022	Graduate Student Researcher University of California, Los Angeles.

PUBLICATIONS

1- **S. Razavian**, A. Babakhani “9.4 A Highly Power Efficient 2×3 PIN-Diode-Based Intercoupled THz Radiating Array at 425GHz with 18.1dBm EIRP in 90nm SiGe BiCMOS,” in *IEEE Int. Solid-State Circuits Conf. (ISSCC) Dig. Tech. Papers*, Feb. 2022, pp. 1-3

2- **S. Razavian** and A. Babakhani, “Silicon Integrated THz Comb Radiator and Receiver for Broadband Sensing and Imaging Applications,” in *IEEE Trans. Microw. Theory Techn.*, vol. 69, no. 11, pp. 4937-4950, Nov. 2021.

3- **S. Razavian**, M. Hosseini, Y. Mehta and A. Babakhani, “Terahertz Channel Characterization Using a Broadband Frequency Comb Radiator in 130-Nm SiGe BiCMOS,” *IEEE Trans. THz Sci. Technol.*, vol. 11, no. 3, pp. 269-276, May. 2021.

4- **S. Razavian** and A. Babakhani, “Multi-Spectral THz Micro-Doppler Radar Based on a Silicon-Based Picosecond Pulse Radiator,” in *IEEE MTT-S Int. Microw. Symp. Dig.*, Aug. 2020, pp. 787-790.

5- **S. Razavian** and A. Babakhani, “A Fully Integrated Coherent 50–500-GHz Frequency Comb Receiver for Broadband Sensing and Imaging Applications,” *Proc. Radio Freq. Integr. Circuits Symp.*, Aug. 2020, pp. 231-234.

6- **S. Razavian** et al., “Plasma Characterization Using a Silicon-Based Terahertz Frequency Comb Radiator,” in *IEEE Sensors Lett.*, vol. 4, no. 9, pp. 1-4, Sept. 2020.

7- **S. Razavian** and A. Babakhani, “A THz Pulse Radiator Based on PIN Diode Reverse Recovery,” in *Proc. IEEE BiCMOS Compound Semicond. Integr. Circuits Technol. Symp.*, Nov. 2019, pp. 1-4.

8- **S. Razavian**, M. M. Assefzadeh, M. Hosseini and A. Babakhani, “THz Micro-Doppler Measurements Based On A Silicon-Based Picosecond Pulse Radiator,” *IEEE MTT-S Int. Microw. Symp. Dig.*, Jun. 2019, pp. 309-311.

CHAPTER 1

Introduction

1.1 THz Band and Potential Applications

THz band consists of waves with a wavelength in the range of 0.03-3 mm with the corresponding frequency range of 0.1-10 THz(Fig. 1.1). This band falls between infrared and microwave/mm-wave bands. It is commonly referred to as the THz gap because this frequency range is too high in electronics and too low in optics. Therefore, conventional electronic or optical techniques cannot be used for THz design. With the recent advances in high-frequency circuit design and demand for higher, faster systems, researchers and engineers have developed new techniques to utilize millimeter-wave (mm-wave) and sub-THz bands for various applications, including imaging, wireless communication, high-resolution radar, and localization [1, 2]. Fig. 1.2 summarizes the main applications.

The speed of wireless communication systems has been increasing continuously. With the current trend (Fig. 1.3), the data rates of wireless local area networks and cellular links are expected to surpass 1 TB/s and 100 Gb/s, respectively, by the end of this decade [3]. According to Shannon–Hartley's ideal communication theorem, these data rates require a large bandwidth, which is feasible to allocate only in frequencies above the mm-wave band. Terahertz (THz) band offers wide unregulated bandwidth, which is vital for the realization of broadband multi-Gbps communication links. Therefore, THz systems can be a good replacement for optical communication systems especially for short to medium range point to point communication. Silicon-based THz communication systems can be employed to

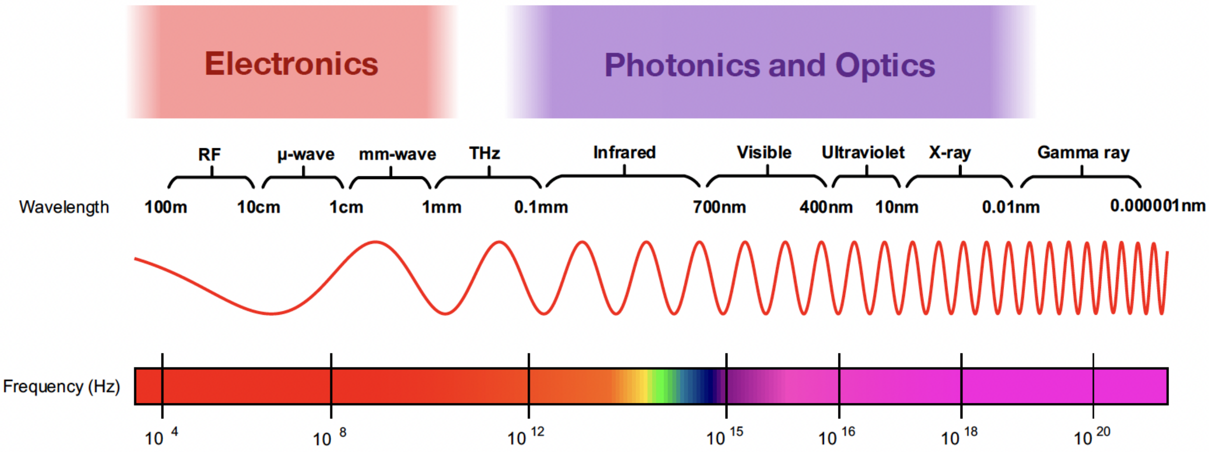

Figure 1.1: Overview of electromagnetic waves spectrum in different frequency regimes

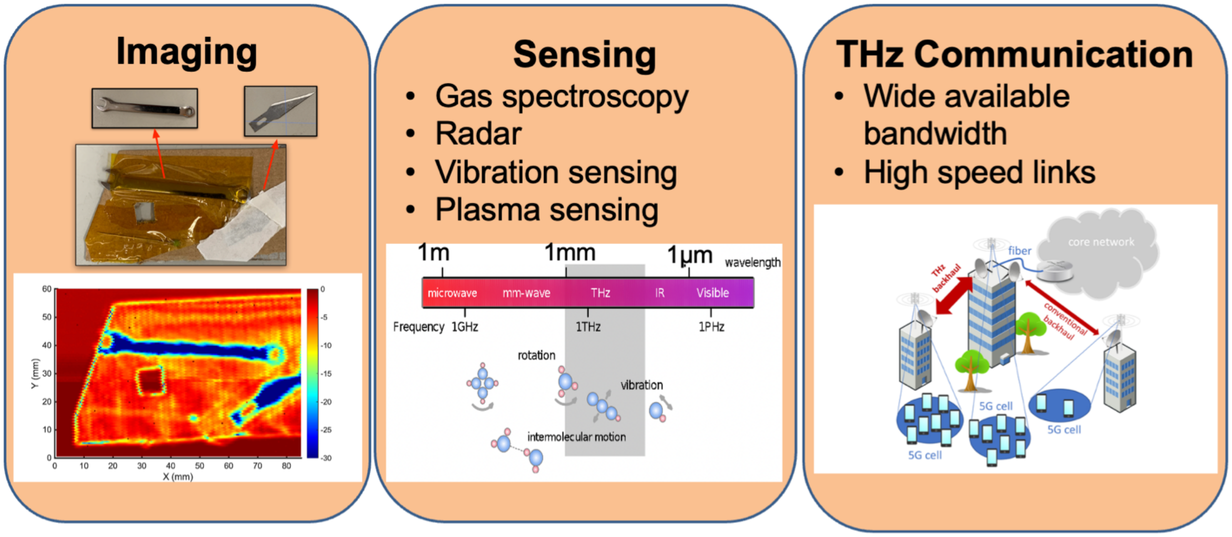

Figure 1.2: Potential applications of THz band.

realize muli-Gbps links at a low cost while benefiting from high integration in contrast to optical communication systems. Yet, employing THz band for communication purposes face different challenges. One of the main limiting factors for medium-range and long-range applications is atmospheric absorption, which limits propagation distance. Fig. 1.4[4] shows the atmospheric absorption loss. As shown, atmospheric absorption is stronger in sub-THz range compared to mm-wave band, thereby enabling communication only for short-range

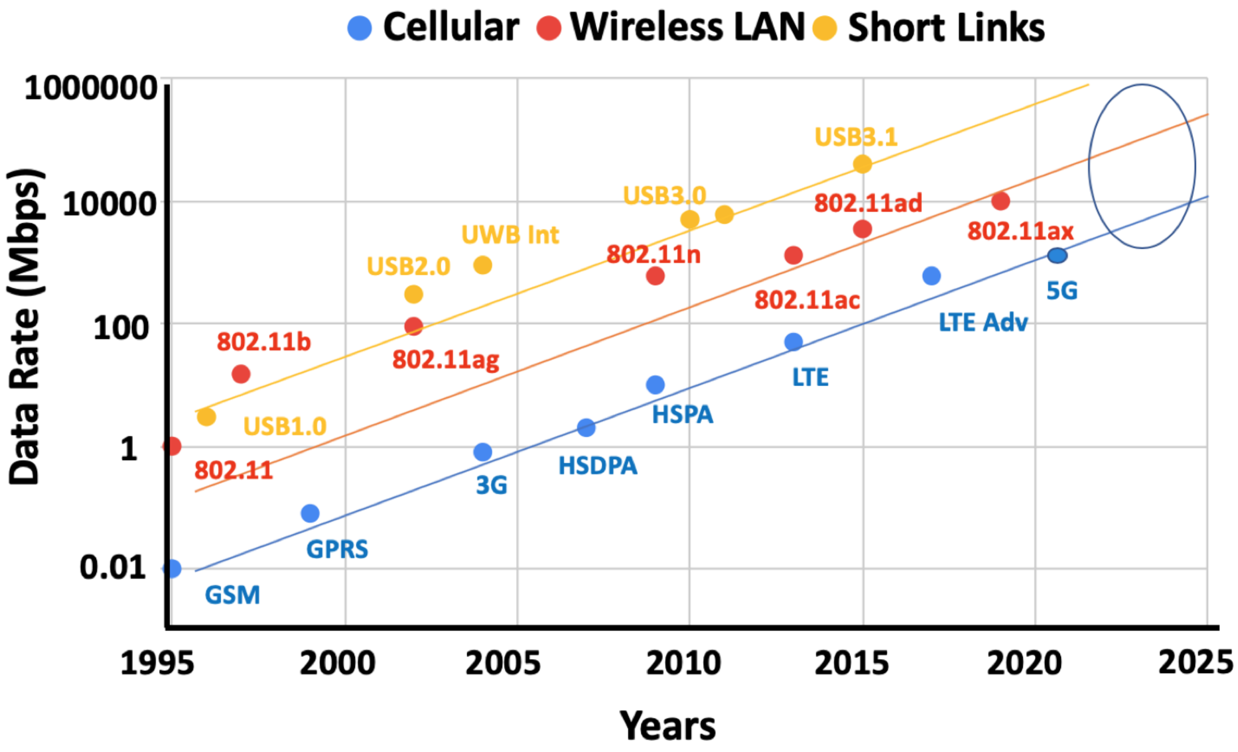

Figure 1.3: Projection for future wireless data rates.

links or point-to-point medium and long-range distances. However, sub-THz regions offer wide unlicensed bandwidth making it an attractive choice for broadband communication. Particularly, low-absorption frequency bands in sub-THz region are of interest for the next generations of high-speed communication systems.

Another potential application in the THz band is hyperspectral imaging, where unique properties of materials and objects can be obtained. Particularly, the THz band has been of interest for imaging applications due to its unique features. The short wavelength of THz waves enables high-resolution imaging. In addition, THz waves penetrate through a wide range of non-polar and non-metallic materials that are opaque in optical frequency bands. Also, materials have different absorption (or reflection) across the THz band, which can be used as a signature for material classification in hyperspectral imaging. These features make THz imaging systems a viable choice for security imaging because they can be employed to

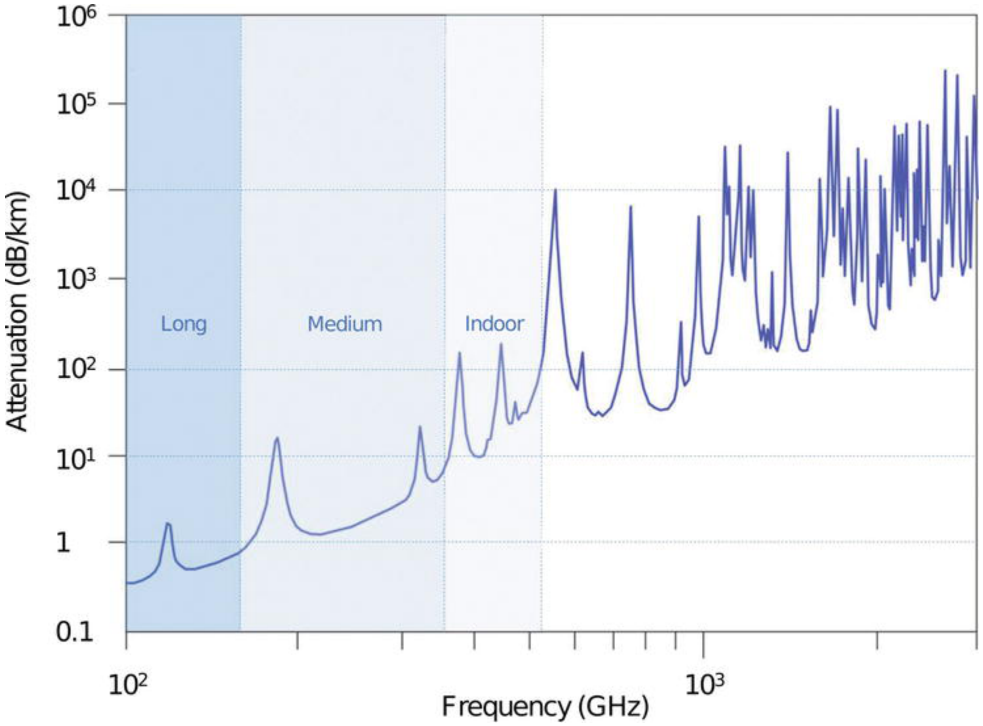

Figure 1.4: Atmospheric absorption of THz radiation.

detect concealed objects, explosives, and hazardous materials. For biomedical applications, THz imaging can be utilized to extract the information about the body tissues and blood samples that only lay in the THz spectrum [5]. For instance, THz-based virus sensing has been developed for Covid detection in [6]. Imaging is performed in two ways: transmission-based and reflection-based. In transmission-based imaging, the waves penetrate through the object of interest and are received on the other side of the object. Whereas, in reflection-based imaging, the reflected waves are received on the same side as the THz source. For instance, in body tissue imaging, where most THz power is either reflected or absorbed, reflection-based imaging is preferred [7]. However, for materials, such as woods and plastics, the transmission of THz waves is higher than reflection. Therefore, in such cases, transmission-based imaging is preferred [8].

THz systems can also be utilized for other emerging sensing applications. Gas spectroscopy is another potential application in the THz band. Various polar gases, especially hazardous ones, have unique absorption lines in THz due to distinct rotational and vibrational transitions. Broadband THz systems are suitable for spectroscopy, as they can be used to detect widely spaced absorption lines of a gas, whereas, narrow-band THz systems are only capable of detecting absorption lines in a narrow band and identifying a small group of materials. Compared to RF and mm-wave frequency bands, THz systems provide a higher resolution due to shorter wavelength in radar applications. In Doppler radars, THz signals enable the detection and characterization of small movements of an object. For the case of weak vibrations, the Doppler effect is referred to as micro-Doppler. THz signals can be used to characterize and measure the signature of the vibration. In [9, 10], audio vibrations are recorded and characterized using THz waves to reconstruct the original audio signal. Moreover, in [11], THz waves go through a plasma medium that changes the propagation speed of THz waves and causes phase shift. By analyzing this shift, distinct information about the physics of a plasma medium is obtained.

1.2 THz Generation Techniques and Challenges

To utilize the sub-THz band for the aforementioned applications, as a vital part of a THz system, reliable sources/transmitters and detectors/receivers are required. Commercial THz optical systems, specifically THz time-domain spectroscopy (THz-TDS) systems, have been used conventionally for sensing applications. These systems utilize two main techniques for THz pulse generation: 1) Optical rectification, and 2) Photoconductive antenna (Fig. 1.5). In the optical rectification approach, femtosecond optical pulses go through a non-linear medium that produces THz picosecond pulses. In the second technique, sharp optical pulses from a femtosecond laser are emitted at a photoconductive antenna that increases the carrier concentration momentarily between two sides of the antenna and generates THz pulses. Generally, optical THz systems are costly and bulky, which limits their use for many applications. Thus, there has been a tendency to implement these systems in electronics,

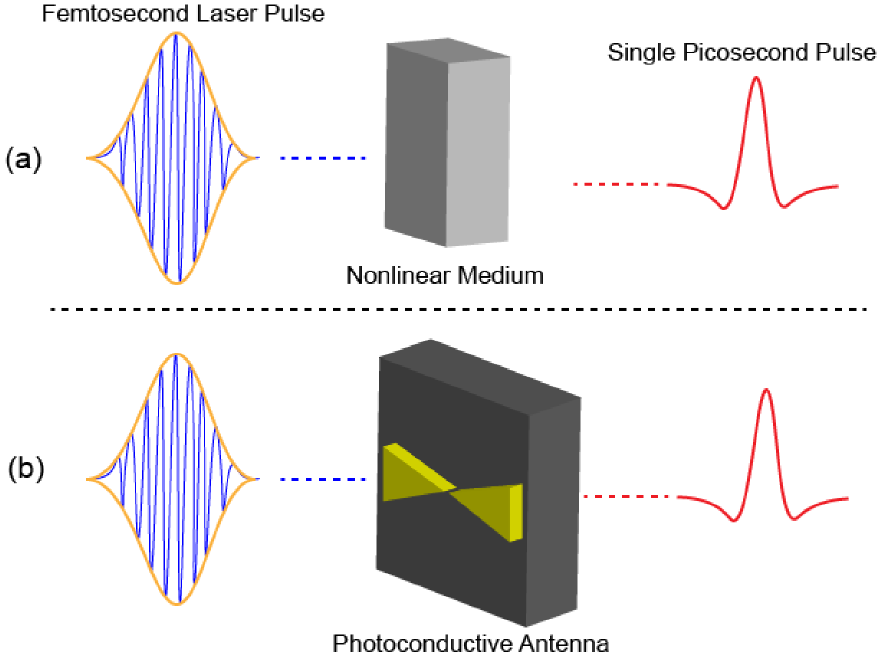

Figure 1.5: Illustration of two main approaches for THz pulse generation in optics.

specifically in silicon-based technologies. Since THz systems in electronics can significantly lower the cost and allow a compact THz design. Electronic THz systems based on III-V semiconductors offer better performance compared to silicon-based processes. However, III-V semiconductors have higher fabrication costs and also suffer from a low level of integration in contrast to standard silicon processes. Different approaches have been proposed for THz generation on silicon. Fig. 1.6 summarizes the most common approaches for THz generation. Based on the method of generation, electronic THz systems can be divided into two main categories: 1) Pulse-based and 2) Continuous-Wave (CW).

In the pulse-based approach, a low-frequency CW RF signal goes through a pulse generator block that generates pulses with the repetition rate set by the frequency of the input RF signal. Different design approaches have been developed for pulse generation, including but not limited to PIN diode reverse recovery, ON-OFF keying, nonlinear T-line structure, and Q-switching [12, 13, 14, 15]. Generally, such systems cover a wide frequency range and high frequency stability, which makes them an ideal choice for broadband sensing applications.

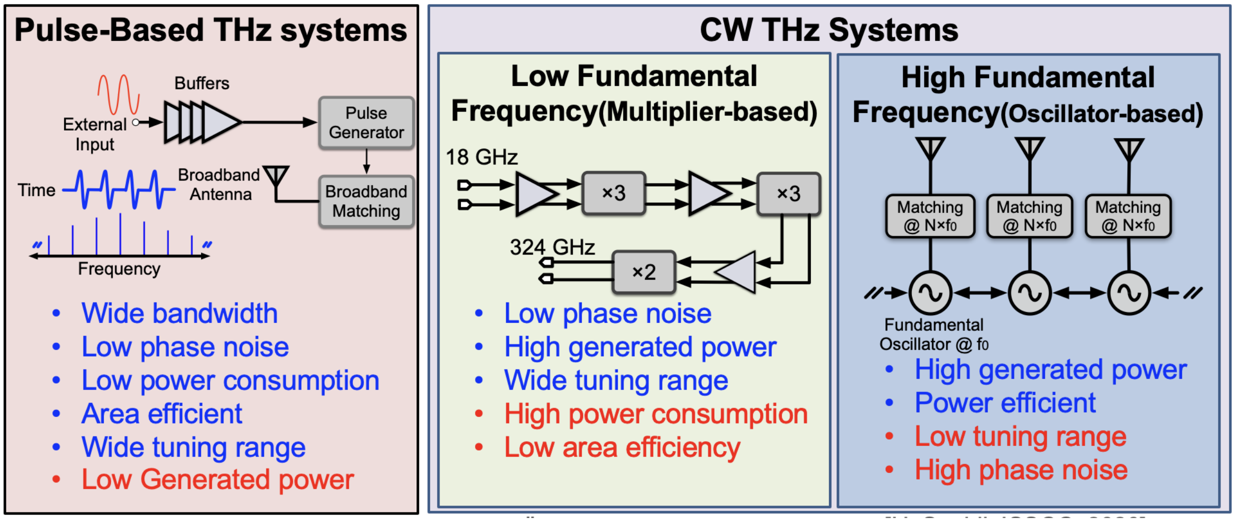

Figure 1.6: Comparison of various THz generation approaches and corresponding pros and cons.

CW-based systems can be divided into two sub-categories based on the frequency of the fundamental tone. In the multiplier-based approach (Fig. 1.6)[16], an RF signal goes through a chain of multipliers and amplifiers to generate a high-frequency THz signal. This approach benefits from a wide frequency tuning range and low phase noise, as the output frequency is locked to the frequency of a stable low-phase-noise RF input. However, the main drawback is high power consumption due to the utilization large number of blocks, which results in low DC-to-RF efficiency. Another approach for CW THz generation is to use high fundamental frequencies rather than a low-frequency RF input. For this purpose, mm-wave and sub-THz oscillators can be employed to directly generate a high-frequency output. Such systems require less number of circuit blocks compared to the multiplier-based approach, since the fundamental frequency is already at high frequencies, thus multiplier chains are not needed. Due to the nonlinearity of active elements in an oscillator, the output signal contains harmonics of the fundamental tone. By extracting these harmonics, THz power can be extracted at frequencies far above $f_{t/max}$ of transistors. These systems generally have high DC-to-RF efficiency and are quite area efficient compared to other techniques.

Because in contrast to multiplier-based systems, they do not require a chain of multipliers and amplifiers. Whereas, The main disadvantage is low frequency tuning range and high phase noise, which is attributed to the low quality factor of passive components used in mm-wave and sub-THz oscillators.

Despite recent advancements in the design of silicon-based THz systems, such systems still suffer from low generated power, which limits their practicality. Therefore, there is an ongoing effort to develop new techniques with the goal of improving the efficiency of these systems. In this dissertation, I have introduced a novel technique based on PIN diode reverse recovery for THz generation in CW and pulse domains. PIN diode has been used conventionally as switches and variable resistors before; whereas, in this work, This device is utilized for a different application in the THz domain. THz generation using PIN diode is demonstrated in this dissertation, but the research on this device for this specific application is still in the early stages and requires further work to fully understand the potential of this device for THz harmonic generation.

1.3 Dissertation Overview

Having provided the background on THz applications and techniques, in the remainder of this dissertation, I provide an in-depth overview of my research, which includes THz circuit design, measurements, and utilizing custom-designed THz chips for different novel applications. In addition, I will elaborate on how each of these designs mitigates the existing challenges in the THz domain. In chapter 2, I introduce a comprehensive theory on PIN diode reverse recovery and how I utilized it for frequency comb[1] generation [12, 17]. The same concept is utilized for the design of a frequency comb receiver [12, 18]. The broadband custom-designed comb receiver in conjunction with the comb transmitter is employed to realize the dual-comb technique over the widest bandwidth ever reported using electronic THz

---

[1] "Frequency comb" and "pulse" are used interchangeably in this dissertation

systems. The presented chip-to-chip dual-comb system provides a low-cost compact solution for broadband sensing applications. As one of the main applications of the presented dual-comb system, hyperspectral imaging is demonstrated. This comb transmitter and receiver are fabricated in 90nm SiGe BiCMOS GlobalFoundries, where each has an active area of 0.48 mm^2 .

In the third chapter, the concept of PIN diode reverse recovery is extended into the CW domain. The first section of this chapter is based on [19]. Rather than using an off-chip low-frequency input signal, as in the case of pulse radiator of chapter 2, an array of on-chip mm-wave oscillators are employed to push the PIN diode into reverse recovery and generate a strong THz harmonic at 425 GHz. Using this technique, the radiation power and efficiency have been improved. In addition, the proposed structure benefits from scalability enabling a large THz radiator array implementation. The results of this work can be utilized for narrowband sensing and communication applications. Moreover, a single element THz radiator in the CW domain at 0.4 THz is employed to perform up to 3-Gbps data communication with OOK and FSK modulations over a 20-meter distance. To the best of my knowledge, this is the longest communication link ever demonstrated using a low-power silicon-based THz radiator. This illustrates the potential of THz communication for point-to-point communication and also provides a low-cost replacement for optical communication links.

In chapter 4, I cover various applications of the custom-designed THz chips of chapters 2 and 3. First, THz waves are used to capture the micro-Doppler vibrations to obtain different features of the vibrations and the vibrating surface. As a novel application, micro-Doppler signatures of audio vibrations are captured and recorded, which is used to reconstruct the original audio signal. A THz interferometry setup is also demonstrated for high-resolution vibration sensing that enables capturing sub-μm displacements caused by audio vibrations. Second, THz frequency comb radiator is employed to perform CO gas spectroscopy and absorption lines of CO gas in the sub-THz band are detected with a high resolution for different gas pressures. Note that the same measurement setup can be used to perform spectroscopy for other gas types. Moreover, as a novel application in the THz domain, the custom-designed frequency comb is employed to probe a pulsed inductively coupled plasma (ICP). This approach enables a compact solution for broadband characterization of pulsed plasma and a low-cost alternative to interferometry. Finally, a long-distance measurement setup is demonstrated using the comb radiator chip over 100 m. In this work, the channel is characterized across in the frequency range 320-1100 GHz and the atmospheric absorption lines are detected. The results of this work pave the way for future long and medium-range communication links in the sub-THz band.

CHAPTER 2

Silicon Integrated THz Comb Radiator and Receiver for Broadband Sensing and Imaging Applications

2.1 Introduction

the recent advances in high-frequency circuit design, Millimeter wave (mm-wave) and sub-THz bands have been of great interest for many applications, such as imaging, wireless communication, high-resolution radar[20], and localization[21, 22]. THz band offers wide unregulated bandwidth, which is vital for the realization of broadband multi-Gbit/s communication links [23, 24]. Moreover, short wavelength of THz waves enables high-resolution imaging for biomedical applications [25]. THz waves have also been used as micro-Doppler radars to pick up the doppler signature of vibrating targets [9]. As a novel application for THz sensing, a broadband THz pulse radiator has been used in [11] to probe a pulsed Inductively Coupled Plasma (ICP). A wide range of materials, including hazardous gases, have unique absorption signatures in the THz band. Therefore, broadband THz systems can be utilized in rotational spectroscopy for detecting different types of gas molecules [26, 27, 28].

However, efficient THz power generation in silicon-based technologies has been challenging, due to the limited maximum oscillation frequency (f_{max}) of the transistors and large parasitics. Therefore, traditional techniques in RF are impractical and inefficient in the THz band. Various techniques have been proposed to tackle the challenge of THz generation beyond f_t/f_{max}. These methods can be divided into two main categories: 1) Continuous Wave (CW) and 2) pulse. CW THz works in recent years have been mainly based on the harmonic extraction of a fundamental oscillator[29] and frequency multiplier chain [30]. In general, oscillator-based CW THz systems are efficient and can generate decent THz power; however, they have limited bandwidth and frequency tuning range. Although a viable solution for applications that need high radiated power such as communication, they are not practical for broadband sensing applications, which require 100s of GHz bandwidth. A large number of CW radiators with different oscillation frequencies can be integrated on a single chip to cover a broad frequency range; however, high DC power consumption and low area-efficiency limit their use in broadband sensing applications [31]. In contrast, for broadband applications, such as spectroscopy and hyperspectral imaging, THz pulse systems generate power across 100s of GHz, while occupying less area. In terms of spectral purity, pulse-based radiators, similar to multiplier-based THz radiators[30], have significantly lower phase noise and less spurs than the oscillator-based CW counterparts [32]. This is due to the fact that mm-wave and sub-THz oscillators suffer from low quality factor (Q) compared to low-frequency oscillators, because of poor performance of varactors at high frequencies. In addition, mm-wave/THz Phase Locked Loops (PLLs) have lower performance than low-frequency ones, which results in further deterioration of phase noise. Therefore, pulse and multiplier-based systems are more practical and offer higher frequency resolution in spectroscopy and sensing [10].

Various THz pulse generation approaches have been proposed in electronics and optics. Conventionally, a THz pulse is generated by emitting a femtosecond laser to a III-V photoconductive antenna [33, 34, 35]. Such systems typically have high power consumption and require a bulky setup to run the laser. In addition, optical THz systems suffer from high jitters and poor phase noise due to using lasers as the source. In electronics, different techniques have been developed for efficient THz pulse generation, including reflection-based and digital-to-impulse (D2I) techniques [36]. The reflection-based short pulse generation (RSPG) technique has been used in [37] to generate pulses with full-width at half maximum (FWHM) of 6.8 ps in a standard 0.11-μm CMOS process, where pulses are generated by pumping pulsed current into a ground-terminated transmission line. Switching a CW source is another technique for generating THz pulses. For instance, in [38], by applying pulse modulation to oscillators, the power of the main tone is spread in the form of side tones, with null-to-null bandwidth of 21 GHz. It is known from Fourier theorem that confinement in the time-domain results in expansion in the frequency domain. Consequently, generating narrow pulses increases the bandwidth. By using D2I technique in [39], 1.9-ps pulses were generated, resulting in a broadband THz comb with detectable tones up to 1.1-THz. At lower frequency bands, step Recovery Diodes (SRD) have been a popular approach for broadband pulse/comb generation. SRDs have been conventionally used in Ultra-Wideband (UWB) systems for different functions, including comb generation, frequency synthesizers, and sampling phase detectors [40]. However, using on-chip SRDs in silicon technologies for THz generation has not been reported, due to challenges in the fabrication of SRDs in silicon processes. PIN diodes, on the other hand, have a similar architecture to SRDs, and benefit from sharp reverse recovery (snappy behavior). Therefore, PIN diodes, although not as efficient as SRDs, can be utilized for narrow pulse generation purposes. PIN diodes are available in silicon processes as custom and standard devices [41]. [17] demonstrates the first THz pulse radiator based on reverse recovery of a PIN diode.

Having explained various approaches for THz pulse/frequency-comb transmitters, compact electronic THz sensing systems are incomplete without a broadband sensitive detector. Similar to THz radiator design, designing THz receivers and detectors faces similar challenges, including limited f_t/f_{max} of transistors [42, 43]. Unconventional approaches have been proposed over recent years to tackle this problem. The plasma-wave effect of FETs has been exploited for the design of THz power detectors, where the electron density of FET channels can be modulated by the incoming THz waves [44]. The FET channel plasma effect has been used in THz heterodyne receivers that can cover a broad frequency range above the transistor f_{max} [45]. Multiplier-based transmitters and receivers are also a viable efficient solution for sensing and imaging applications that can cover the sub-THz band [46]. Passive diode mixers can also be used for broadband heterodyne detection. [18] reports a 50–500-GHz frequency-comb receiver, in which a broadband LO comb is generated to modulate the current of a diode-connected Bipolar-Junction-Transistor (BJT). Schottky Barrier Diodes (SBD) have been quite popular for Square-law detectors due to high cut-off frequency, which can be as high as 2 THz [47]. Since the SBDs have a high responsivity in the THz band, they are a suitable choice for broadband detection in THz regime [48].

In this chapter, a fully integrated THz frequency comb/pulse transmitter and receiver in silicon are presented. The THz pulse radiator, which is an extended version of [17], gives details and analysis on utilizing PIN diode reverse recovery for pulse generation. Compared to [17], an additional PIN diode is used to generate bipolar pulses, thereby improving DC-to-RF efficiency and increasing the radiated power. The frequency comb receiver expands on [18], whereby the diode-connected BJT is replaced with an SBD to increase sensitivity and bandwidth. The comb receiver of this work enables detection of broadband THz waves up to 525 GHz with a sensitivity and noise figure comparable to that of state-of-the-art CW THz receivers. The remainder of this chapter is as follows. In section 2.2, PIN diode reverse recovery and the dual-comb approach are explained in detail. In section 2.3, design of the radiator and receiver are discussed. Section 2.4 presents the measurement setup and results. Finally, section 2.5 concludes this work.

2.2 Theoretical Analysis

2.2.1 PIN Diode Reverse Recovery

Structure of a PIN device is shown Fig. 2.1. In 90-nm SiGe BiCMOS, a standard PIN diode is an epitaxial device consisting of doped P, N, and undoped I (intrinsic) regions. PIN diodes have been widely used as RF switches, variable attenuators, and photo-detectors [49, 50]. In this work, PIN devices are utilized in reverse recovery mode for pulse generation. The PIN diode is a high-level injection device. This means that, in the forward mode, the

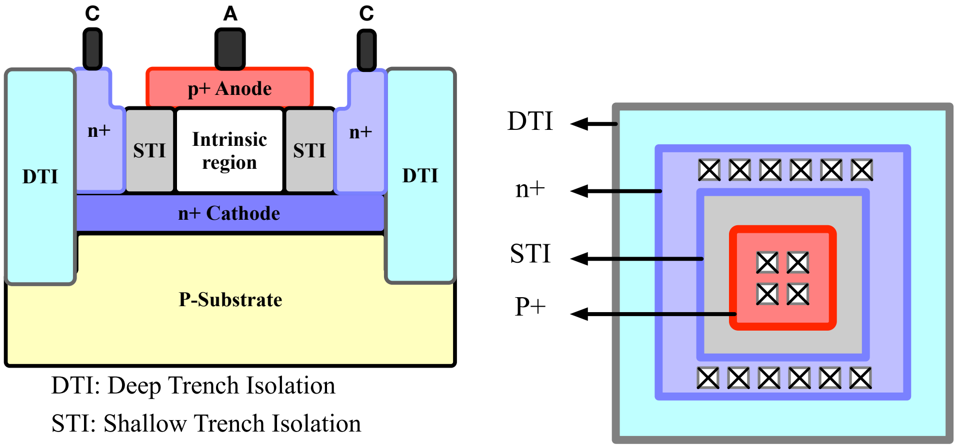

(a) (b)

Figure 2.1: PIN diode in the 90-nm BiCMOS GF technology: (a) cross section and (b) top view.

I-region is filled with a high level of electrons and holes from P and N regions, which reduces the resistance of the I-region and facilitates conduction. This effect is the basis of PIN-diode-based attenuators, wherein the I-region resistance can be tuned by controlling the injection level. The amount of stored charge can be derived by the charge control equation as follows:

$$I = \frac{2dQ_c}{dt} + \frac{2dQ_i}{dt} + \frac{2Q_c}{\tau_c} + \frac{Q_i}{\tau_i} \tag{2.1}$$

where Q_c and Q_i are the stored charge in the doped (P, N) and intrinsic regions respectively. τ represent the carrier lifetime. Note that, in a PIN diode, the carrier lifetime in the intrinsic region (τ_i) is orders of magnitude larger than the carrier lifetime in the doped region (τ_c) [51]. Therefore, the equation of (2.1) can be simplified to:

$$I = \frac{dQ_i}{dt} + \frac{Q_i}{\tau_i} \tag{2.2}$$

In this work, the PIN diode's reverse recovery is of interest, which happens during turning off the diode. To better understand the details of reverse recovery and switching transients,

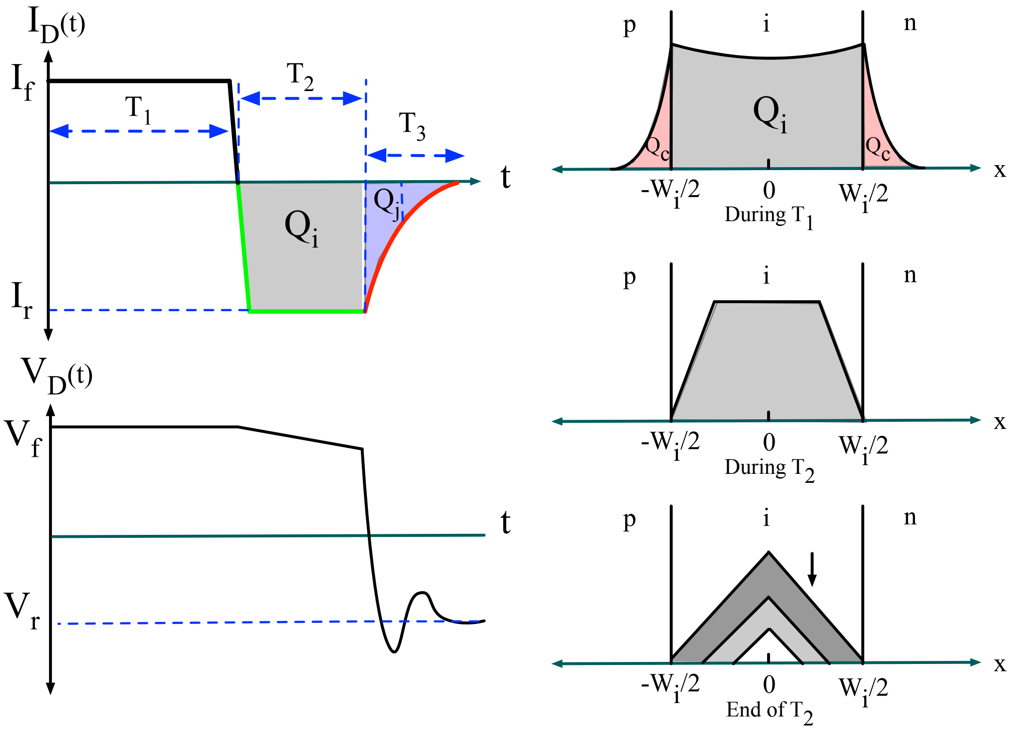

Figure 2.2: Illustration of PIN diode reverse recovery and charge distribution during switching transients.

the case of Fig. 2.2 is considered. During T_1, the diode is in conduction mode, and the I-region is filled with holes and electrons supported by the forward current. In addition to charges in the I-region, minority charges are also present at N and P junctions; however, due to the lower time constant (τ) of these regions, they are negligible. The amount of stored charge in the I-region can be derived as follows:

$$Q_i = I_f \times \tau_i \tag{2.3}$$

When the voltage across the diode drops, the stored charge in the I-region is depleted by means of a reverse current, which is specified as the T_2 time interval. Note that, in this interval, the diode is still ON and the voltage between the P and N junctions is roughly equal to V_f. The reverse current in this mode cannot be sustained infinitely, and it will drop to zero once the I-region is fully depleted. At the beginning of T_3, it can be assumed that most charges are depleted from the I-region. The reverse current drops to zero with a time constant, which depends on reverse capacitance, junction resistances, and the charge mobility in silicon. During this time, the reverse current is split in two parts. One charges the reverse capacitance and the other part recovers the small amount of charges that are left in the I-region. Assuming that the electric field value exceeds the saturation level, the mobility reaches saturation, and the velocity of the charges remains constant and is referred to as the saturation velocity (v_s). Thus, the duration of T_3 can be estimated as:

$$T_3 = \frac{w_i/2}{v_s} \tag{2.4}$$

At the end of T_3, reverse recovery is complete and the diode turns off. In this work, a standard PIN diode device is utilized. Although the details of a PIN diode structure are not shared by the foundry, the depth of I-region can be approximated based on the STI thickness. For the BiCMOS SiGe 90-nm process, the STI region is less than 300 nm. Therefore, using (2.4), $T_3 \approx 1.5ps$. Note that, this is an estimate, and the real value is expected to be smaller, as simulation models suggest.

2.2.2 Dual-Comb Technique

Dual-comb is an emerging tool for spectroscopy and broadband sensing applications. This approach has been used broadly in the optical domain by employing femtosecond mode-locked lasers [52]. In this work, a fully integrated solution for the dual-comb technique is implemented in electronics. The conceptual representation of the dual-comb technique is shown in Fig. 2.3. In the dual-comb approach, two pulse trains with slight difference in the repetition rate are mixed. According to Fourier theory, a pulse train corresponds to a frequency comb in the frequency domain, such that the spacing between two tones is determined by the repetition rate of the pulse train. Therefore, as Fig. 2.3 suggests,

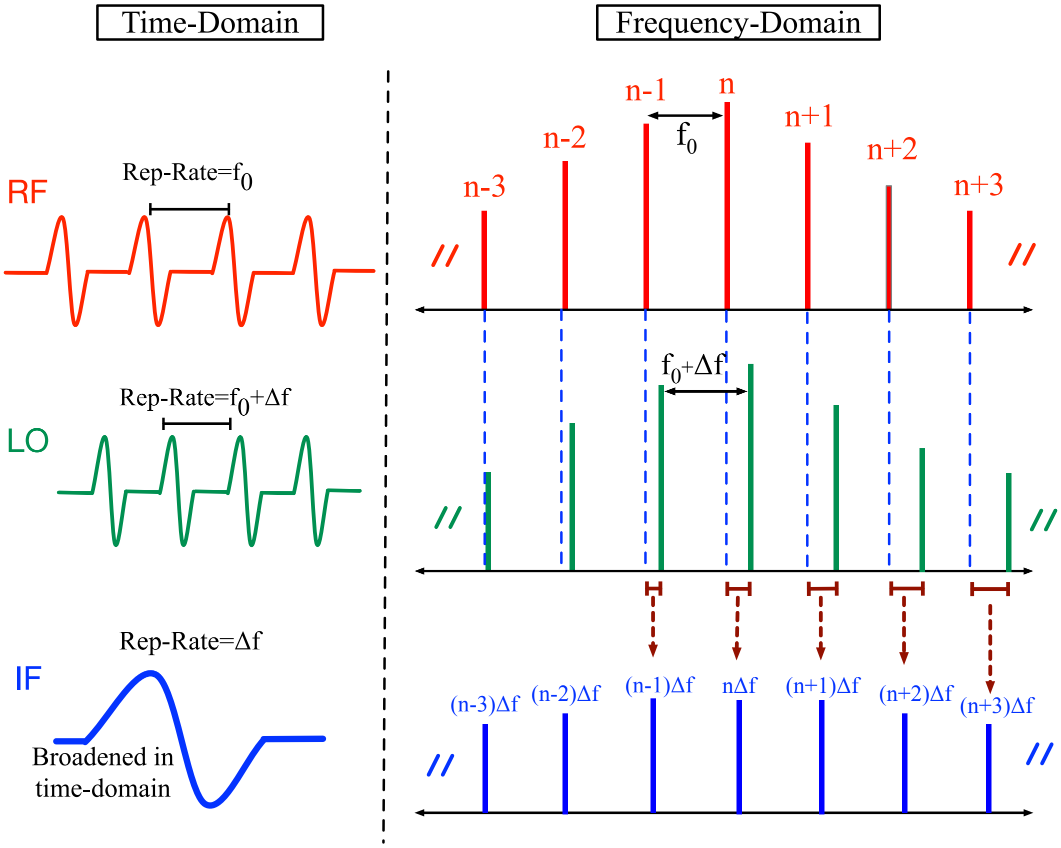

Figure 2.3: Conceptual illustration of dual-comb approach.

mixing two frequency combs with different spacing between tones results in a low-frequency (IF) frequency comb that preserves information of the original combs. Consequently, RF information over a wide band is mapped to a low-frequency IF comb, which can be sampled using low-cost electronic instruments. In the time-domain, the dual-comb is equivalent to sub-sampling method, in which at each cycle, a specific point of the incoming RF signal is sampled. The resultant IF comb is a broadened version of the RF signal. The sub-sampling technique is the basis of most optical THz pulse systems. To implement this technique in electronics, a broadband comb transmitter and receiver with programmable spacing between the tones are required. This technique benefits from high frequency stability, high sensitivity, and large bandwidth. In the following sections, the design of the transmitter and receiver, as the main components of the dual-comb implementation, are discussed in detail.

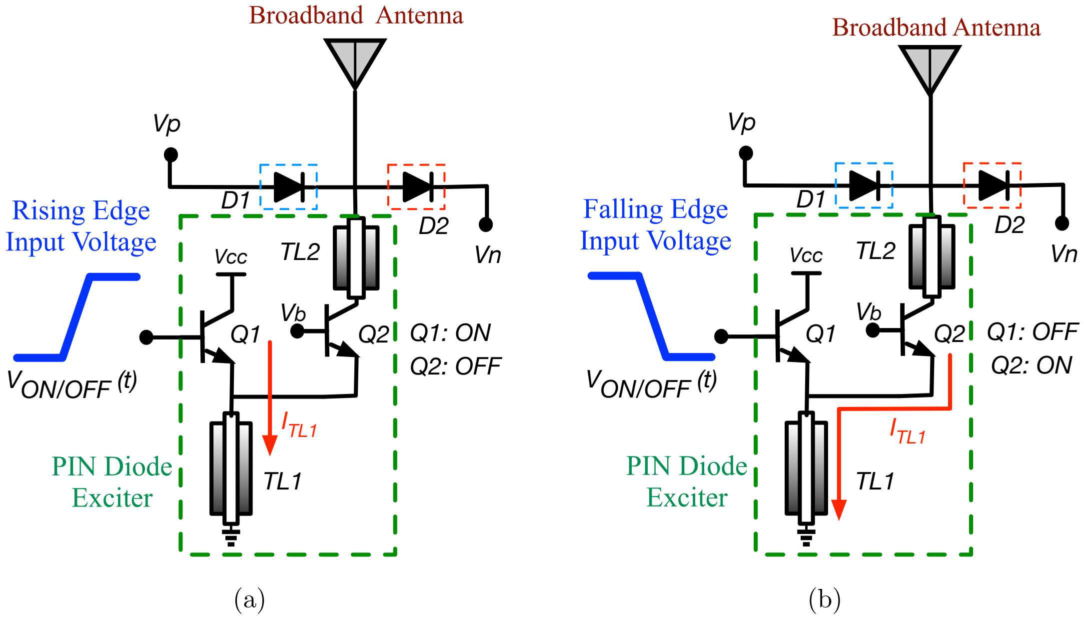

Figure 2.4: (a) Exciter is switched ON, (b) exciter is switched OFF.

2.3 Frequency-Comb Transmitter and Receiver Design

2.3.1 PIN-Diode-Based Pulse Radiator

As discussed in section 2.2, PIN diodes can be nonlinear in reverse recovery mode. A sharp drop in reverse current can be utilized for narrow pulse generation by providing a proper load impedance. To push a PIN diode device into reverse recovery, a PIN diode exciter stage is designed to generate a large voltage swing across the PIN diodes that can force it into reverse recovery. The operation of the exciter can be divided into two time intervals. Fig. 2.4(a) demonstrates the case when the exciter is switched on by the rising edge of the signal at the base of Q_1. During this period, Q_1 is ON and the current that flows through TL_1 keeps increasing. In other words, the energy is stored in $TL1$ in the form of current. In the second interval (Fig. 2.4(b)), Q_1 is switched OFF. Due to the high inductance of TL_1, its current cannot drop abruptly. Consequently, the current, which was stored in TL_1, turns on Q_2 and flows through TL_2. This abrupt flow of current to the second

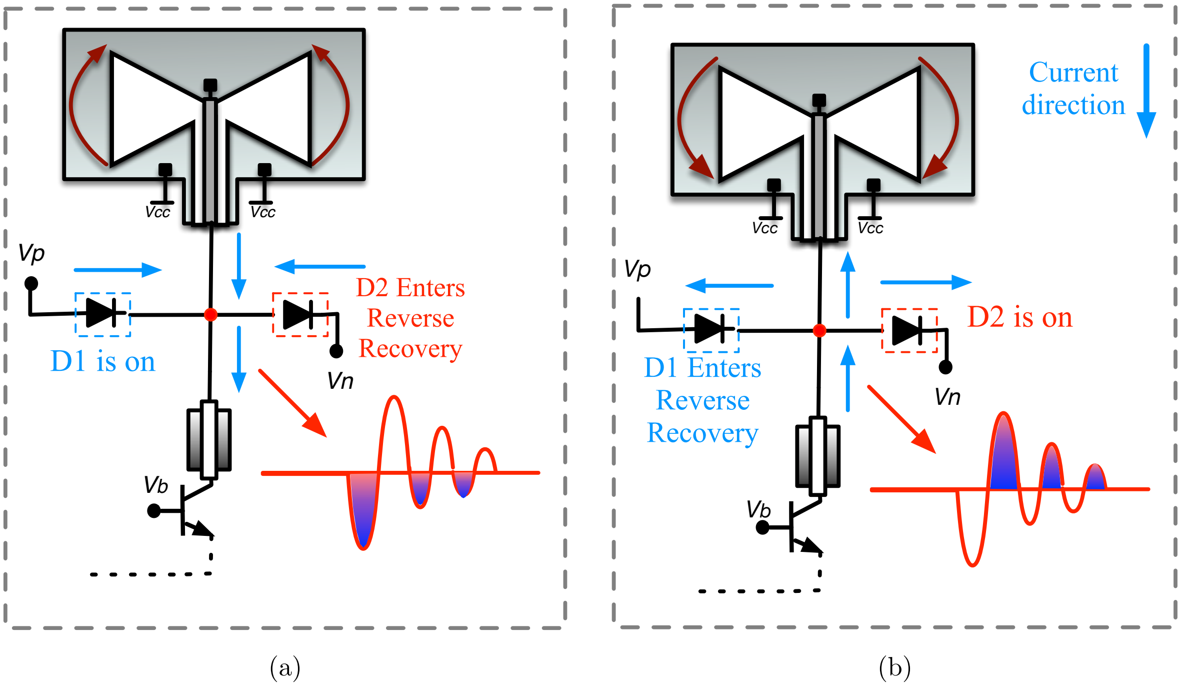

Figure 2.5: Mechanism of bipolar pulse generation using two PIN diodes. (a) During this time interval, D2 cuts the flow of current and generates negative pulses. (b) D1 is in reverse recovery and generates positive pulses.

branch containing Q_2 generates a large damping oscillation at node X that pushes each of the PIN diodes into reverse recovery separately. Two PIN diodes are employed to generate bipolar pulses in each cycle. Fig. 2.5, illustrates how reverse recovery occurs when a damping oscillation occurs across the diodes. In Fig. 2.5(a), D_1 is turned on and the I-region of $D1$ is filled with charges. During this time, D_2 is in reverse mode, and the I-region is being depleted. In fact, D_1 and D_2 function as two fast switches that shut down the current of the broadband slot antenna in opposite directions. As a result, during the damping oscillation period, positive and negative pulses are generated. Note that, the frequency of the damping oscillation is set by the impedance of antenna, parasitics, and matching TLines, which is $\approx 60\ GHz$ in this design.

The choice of the PIN diode size is critical in this design. Larger diodes have better

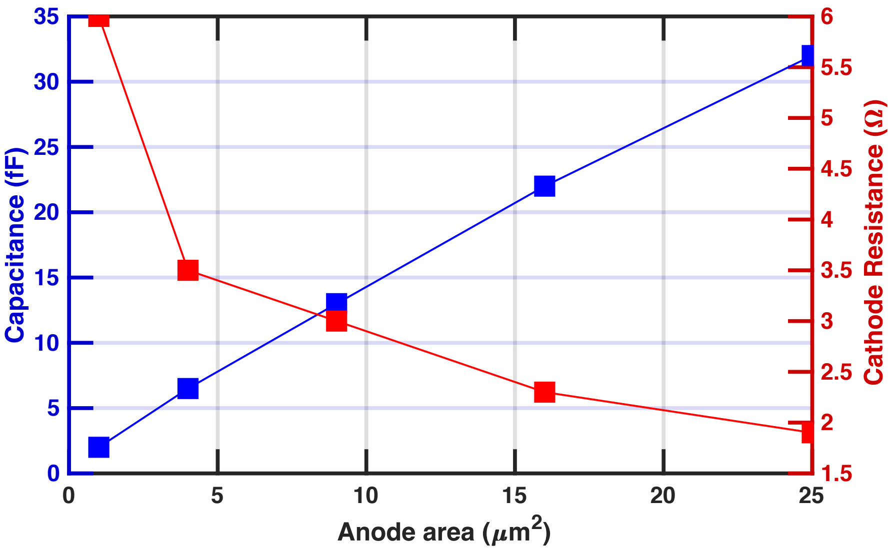

Figure 2.6: Parasitic anode-cathode capacitance and cathode resistance for different sizes of a standard square PIN diode device.

conduction, at the cost of more parasitics that can significantly reduce the generated THz power at high frequencies. Moreover, larger diodes have longer reverse recovery and take longer to charge and deplete the I-region. Therefore, they cannot be driven by a high-frequency signal. Fig. 2.6 demonstrates the trade-off between device size and parasitics, based on the device standard model when the device is biased at 0 V. Although cathode resistance decreases as the diode size increases, the increase in the anode-cathode capacitance is sharper. Additionally, the I-region resistance is greater than the cathode resistance when the diode is entering reverse recovery. To better understand the effect of the PIN diode size on the quality of pulse generation, the case of Fig. 2.7(a) is considered. Fig. 2.7(b) clearly indicates that the smallest diode has the sharpest reverse recovery and presents the shortest time constant (τ) at the final stage of reverse recovery (T3). The time constant of reverse recovery is directly correlated with the pulse width, and determines the amount of the power that is radiated in the sub-THz band. Note that, at each pulse cycle ($1/f_{rep-rate}$), the I-region of PIN diode should be fully depleted, otherwise the amplitude of the generated pulses will be arbitrary at each cycle (unwanted amplitude modulation). Thus, the size of

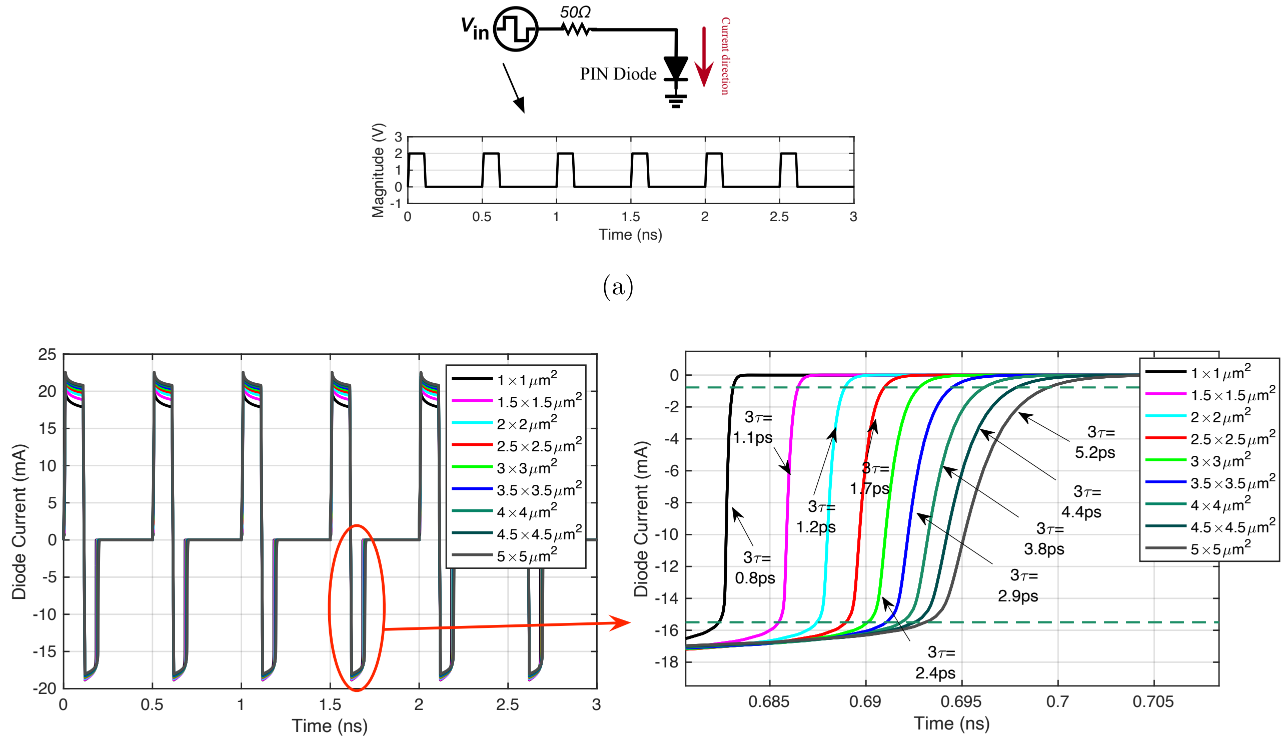

(a)

(b)

Figure 2.7: (a) Test bench for analysis of PIN diode size. (b) Current waveforms of the diodes, which illustrates how the size of the PIN diode affects the final stage of reverse recovery.

transistors in the PIN diode exciter stage should be tuned based on the PIN diode size, to ensure the PIN diode is fully depleted at the end of each pulse cycle. In this design, $1 \times 1 \mu m^2$ PIN diode is used, and the transistor size is chosen based on this PIN diode size to achieve the sharpest reverse recovery.

The simulated time-domain waveforms of the radiated pulses are shown in Fig. 2.8, which is based on a near-field 2nd-order lumped model of the antenna [53]. By adjusting the voltage of the PIN diodes, the position of each pulse can be adjusted, as shown in Fig. 2.8. This allows improving and tuning the generated power for each frequency tone. It is critical to have a sharp driving signal for a proper operation of the exciter stage. The rising and falling

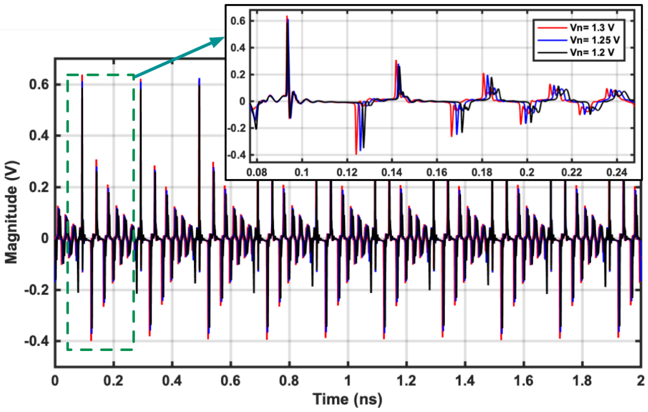

Figure 2.8: Simulated time domain waveform of the radiated pulses for different biasing of PIN diodes.

edge signal that drives the PIN diode exciter is generated by a series of edge sharpening buffers. Fig. 2.9 shows the full pulse radiator schematic. The edge sharpening buffers can operate up to 15 GHz. These buffers are driven via an input trigger signal from an external source.

For efficient THz radiation, a broadband coplanar waveguide (CPW) fed slot-bowtie antenna is employed (Fig. 2.10(a)). A slot-bowtie antenna was chosen over a bowtie antenna for two main reasons. First, for reverse recovery to occur, the antenna must be inductive at the frequency of the damping oscillation (60 GHz). This facilitates the flow of large reverse current through D_1 and injects the forward current through D_2. Below the first resonance, slot-bowtie antenna provides enough inductance to facilitate reverse recovery. Impedance of the antenna is shown in Fig. 2.10(b). The impedance of the antenna shows a small imaginary component from 300 to 650 GHz. In addition, the real part of the impedance is relatively constant. This facilitates broadband impedance matching over this frequency range. Second, in a broadband system, designing a wideband DC path for biasing can be challenging and occupies a large area. Using RF chokes, also is not a viable choice, since it is not reliable at high frequencies and can cause unwanted oscillation. The slot-bowtie antenna provides a DC path for Q_2, eliminating the need to design a biasing matching network.

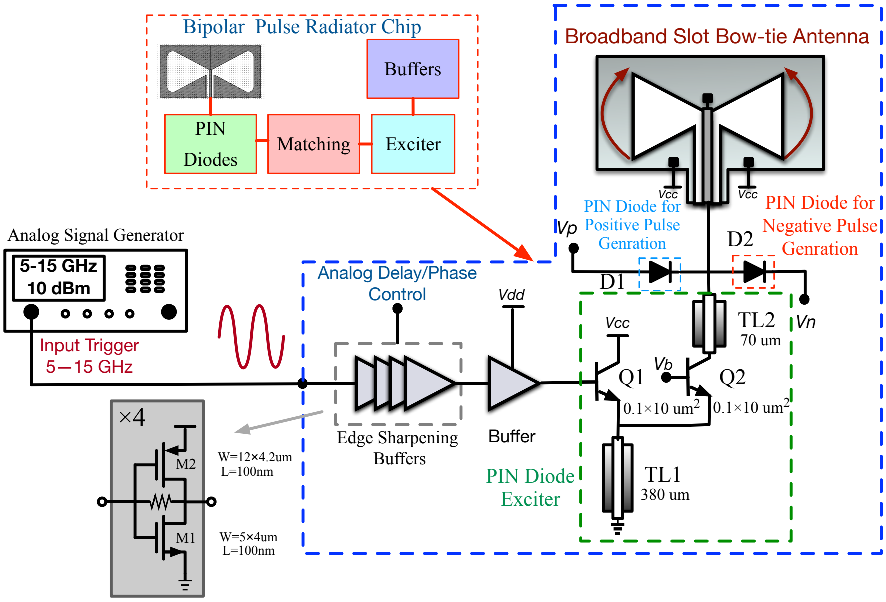

Figure 2.9: Full schematic of the THz comb/pulse radiator based on PIN diode reverse recovery.

On-chip antennas in bulk processes suffer from low efficiency due to the lossy doped silicon substrate. The silicon substrate traps the radiated waves from the antenna in the form of waveguide modes and prevents efficient radiation in air. To address the aforementioned problem, a high-impedance hemispherical silicon lens is attached to the chip via a high resistivity silicon layer with 10 k$\Omega.cm$ resistivity, which mimics the infinite silicon substrate, and eliminates the substrate modes resulting in higher radiation efficiency. The length of silicon layer greatly affects the radiation directivity. Based on [54], the thickness of silicon layer is chosen 3 mm, which is roughly one third of the lens radius. The packaging details are given in Fig. 2.10(a). Moreover, the silicon lens effectively increases the aperture of the radiating antenna, which results in a higher gain and efficiency. Antenna efficiency is depicted in Fig. 2.10(c).

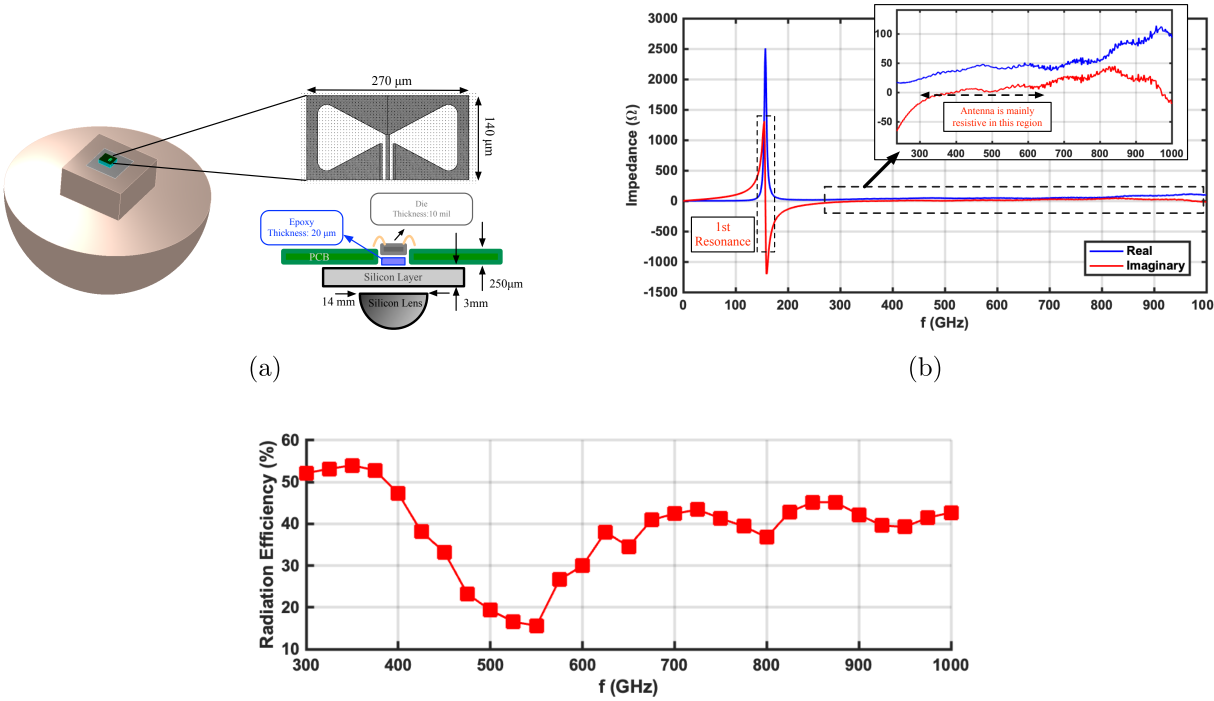

(a)

(b)

(c)

Figure 2.10: (a) Details on the antenna dimensions and system packaging, (b) impedance of the antenna, (c) efficiency of the antenna over the frequency range of radiation.

2.3.2 Frequency-Comb Receiver

For frequency comb detection, the heterodyne detection method is used (Fig. 2.11(b)). Compared to square-law detectors, heterodyne detectors benefit from significantly higher sensitivity and lower conversion loss due to mixing with a strong LO. For broadband heterodyne detection, similar design blocks are used for broadband LO comb generation. Fig. 2.11(c) shows the design of the receiver. This architecture is, in other words, a sub-sampling receiver, such that in each cycle, the incoming THz signal is sampled by the standard SBD device. SBD has been used vastly for THz non-coherent square-law detection; whereas, in this work SBD is used to for coherent mixing of incoming THz waves with the LO comb. A standard SBD device in the 90-nm BiCMOS process is employed, which presents low parasitics and

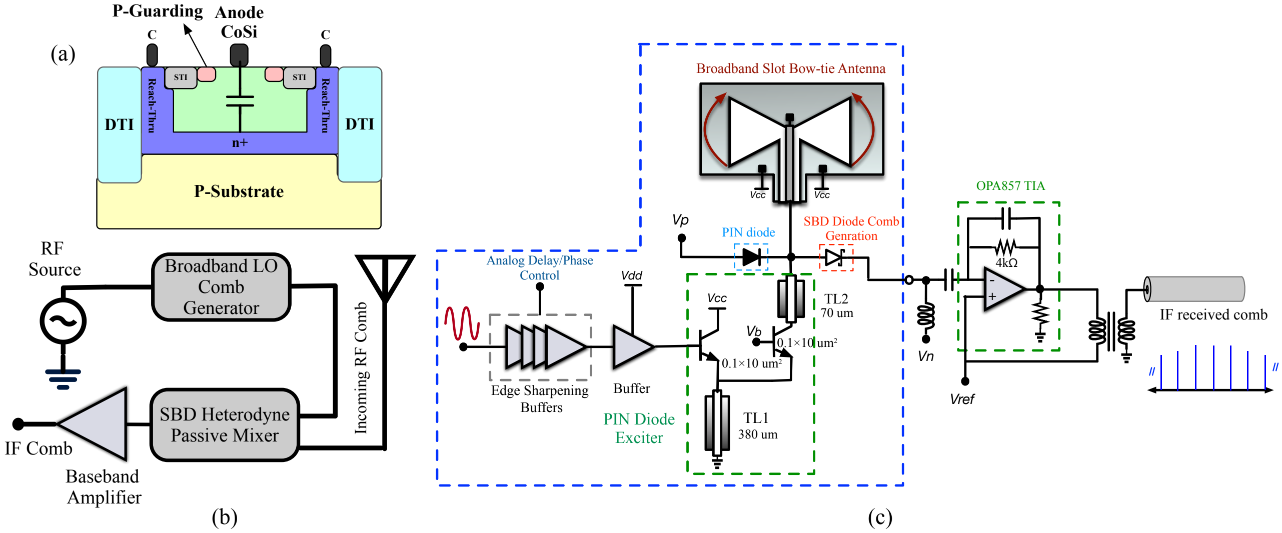

Figure 2.11: (a) Structure of a standard epitaxial SBD device in 90-nm BiCMOS GF process. (b) Block diagram of broadband heterodyne receiver. (c) Full schematic of the receiver.

high responsivity to THz waves. The physical structure of SBD is shown in Fig. 2.11(a). The choice of SBD size is important, as there is a trade-off between the mixer conversion loss and bandwidth. The cut-off frequency of SBD against the anode area is plotted in Fig. 2.12, which shows that, with the increase of the anode area, the cut-off frequency decreases. This is due to the fact that $C_{off} \propto A_{an}$ while $R_{on} \propto A_{an}^{-0.5}$. Although diodes with a smaller area have a higher cut-off frequency, larger diodes, due to the higher effective transconductance, can result in lower conversion loss at the frequency range of interest (below 1 THz). To determine the effect of SBD size on conversion loss, the test bench of Fig. 2.13(a) is used for PSS and PAC analysis, whereby LO is a 50 GHz large signal, and IF is a small signal at harmonics of the fundamental tone. Fig.2.13 shows the change in conversion loss for different sizes of SBD. Note that, the performance of SBD deteriorates significantly for SBDs larger than 3×3 μm^2. In this design, a 2×2 μm^2 SBD with a cut-off frequency of 1 THz is used, as based on simulations, it offers a relatively better conversion loss compared to that of other sizes of SBDs. The trigger signal frequency results in different responses, where higher sensitivity is achieved with a higher frequency trigger signal. This is due to the fact

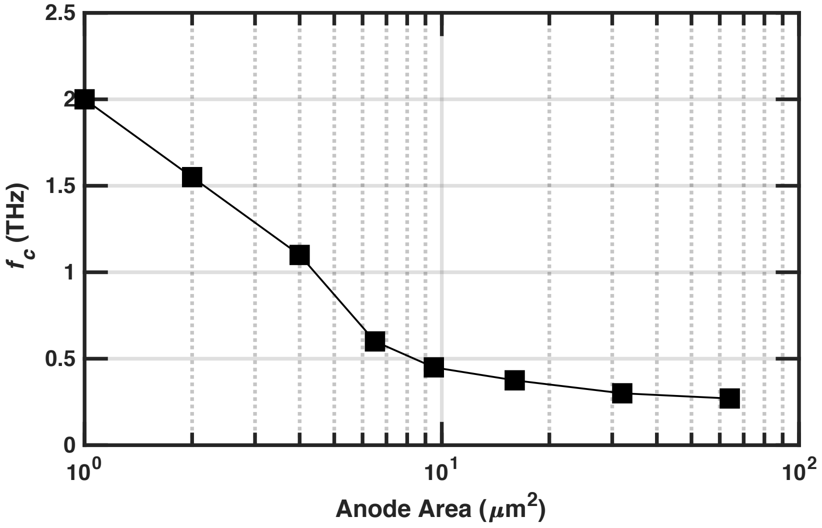

Figure 2.12: Cut-off frequency versus diode anode area based on standard model of SBD in 90-nm SiGe BiCMOS GF process.

that increasing the trigger frequency, results in a stronger LO comb.

2.4 Measurement Results

The pulse radiator and comb receiver are fabricated in the GlobalFoundries 90-nm SiGe BiCMOS process. The DC power consumption of the radiator and receiver are 40 and 38 mW, respectively. The die micrograph of the comb transmitter and receiver are shown in Fig. 2.14. The transmitter and receiver chip are measured and characterized separately on two different PCBs. For both chips, the repetition-rate of the pulses (input trigger frequency) can be tuned to an arbitrary frequency, with highest frequency of 15 GHz, which results in the lowest conversion loss and highest radiated power for the receiver and transmitter, respectively.

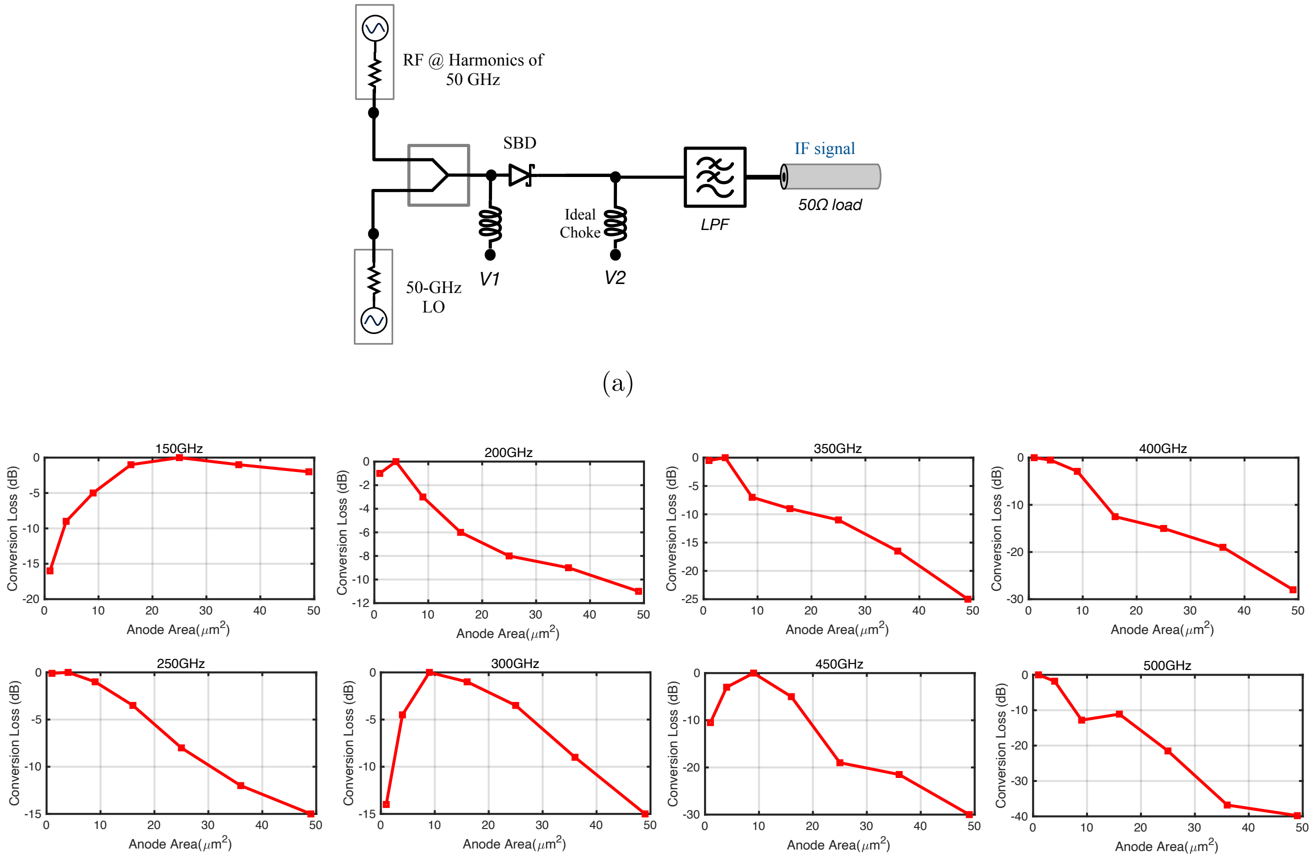

(a)

(b)

Figure 2.13: (a) Schematic used for simulation to determine the proper choice of SBD size. (b) Normalized conversion loss against different sizes of SBD across sub-THz band.

2.4.1 Frequency-Domain Characterization of Pulse Radiator

One of the important characteristics of THz radiators is the effective isotropic radiated power (EIRP). In pulse radiators, the EIRP measurement is challenging compared to CW radiators, as it requires measuring EIRP for each tone separately. This requires adjusting the position of the chip across frequency tones, since the radiation pattern and angle of the main lobe are susceptible to change. Different factors can cause change in the angle of the main lobe. During packaging and assembly, the epoxy below the chip may not be uniform, resulting the chip being uneven. The silicon lens may be misaligned and not positioned exactly at

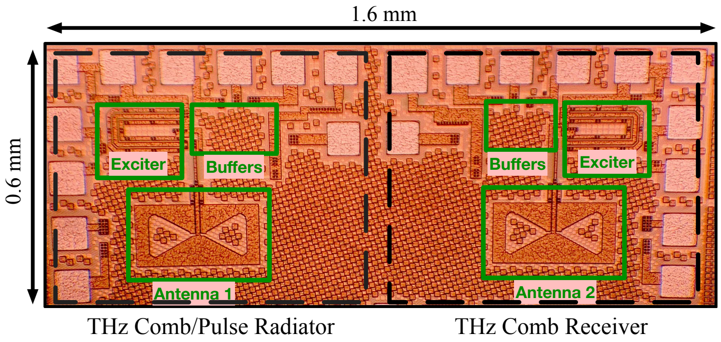

Figure 2.14: Micrograph of the pulse/comb radiator and receiver.

the center. In addition, the on-chip metals, pads and capacitors are not symmetric around the on-chip antenna, which can cause deviation in radiation angle across the THz band. To characterize the radiated tones across the THz band, four different bands of Virginia Diodes, Inc.

(VDI) Spectrum analyzer extender (SAX) THz down converters are employed to cover from 220 GHz up to 1.1 THz. The measurement setup of Fig. 2.15(a) is used for radiator characterization in the frequency domain. EIRP calculation is performed based on the Friis formula in the farfield. To ensure farfield mode of radiation, the receiver antenna and radiator are 10 cm and 35 cm apart for frequencies above and below 330 GHz, respectively. Although the Fraunhofer distance is larger than 10 cm for a lens size with a diameter of 14 mm, the farfield distance is below that which the Fraunhofer distance formula predicts. This is due to the fact that the effective aperture of the radiation is significantly smaller than the size of the lens for the case of a directive on-chip antenna. Fig. 2.15(b) confirms the farfield mode of radiation for the distance of 10 cm at 495 and 750 GHz. For the EIRP calculations, the conversion loss of the mixer at each frequency point is de-embedded from measurements, which ranges from 1 to 25 dB. Conversion loss data is provided by VDI based on calibration using PM5B power meter with a 0.5-dB margin of error. In addition, the spectrum analyzer calibration error and the loss of cable at IF are taken into account to reduce the error in the EIRP measurements. EIRP depends on the repetition-rate of the radiated pulses. Ideally,

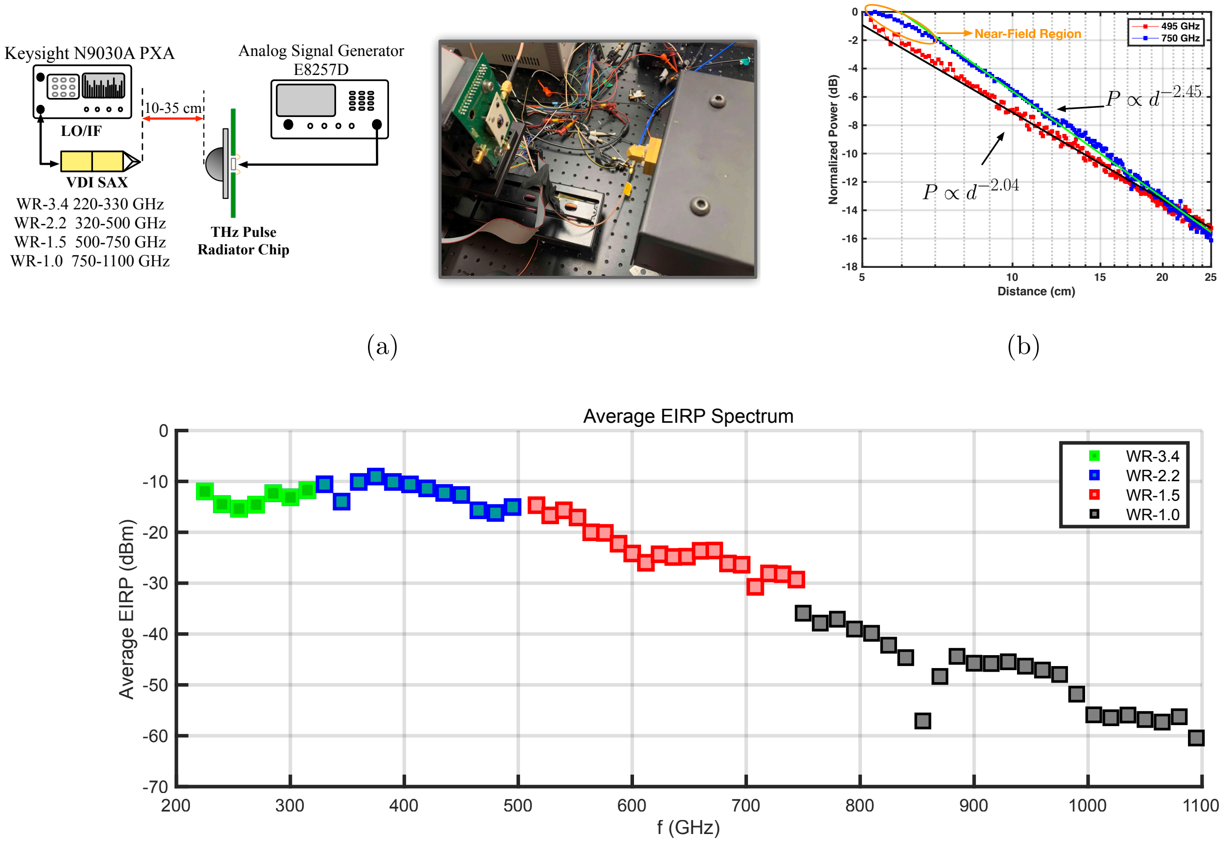

(a) (b)

(c)

Figure 2.15: (a) Frequency-domain characterization measurement setup. (b) Received power versus distance at 495 and 750 GHz. Results are consistent with the Friis transmission equation. (c) Measured EIRP from 220 to 1100 GHz using 4 different SAX modules.

increasing the repetition-rate by N results in a $20log(N)$ increase in each corresponding tone. To cover each point in the spectrum, the repetition rate of pulses need to be swept. For instance, to cover any arbitrary frequency point above 285 GHz, the repetition rate needs to be swept from 15 GHz-750 MHz to 15 GHz. Although the EIRP of tones is directly correlated with the repetition rate, the effect of 100s of MHz change in the repetition rate on the EIRP is negligible. For EIRP measurements, the repetition rate of 15 GHz is chosen, which is the highest operating frequency of input buffers and exciter stage. The EIRP of the radiated

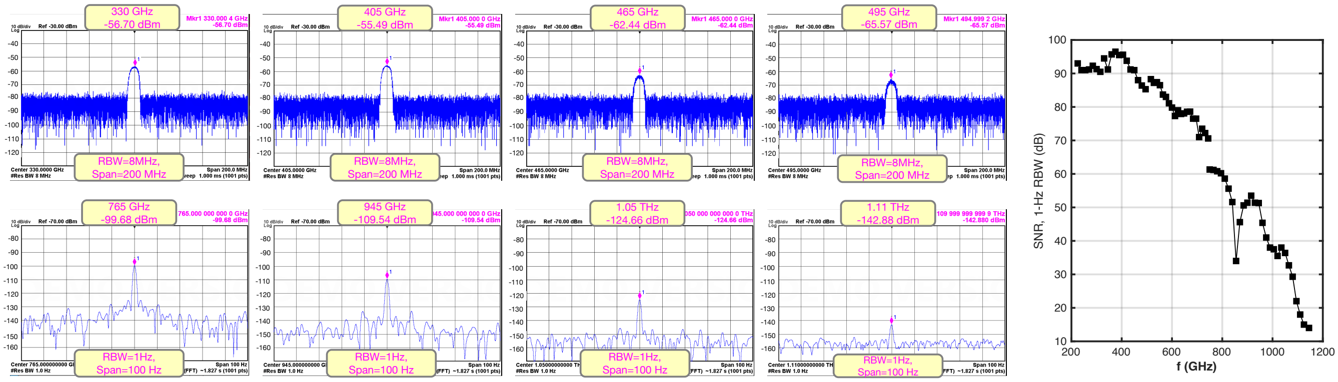

(a) (b)

Figure 2.16: (a) Measured tones of the radiated frequency comb. (b) Corresponding SNR for each received tone by VDI SAX module with 1-Hz RBW.

tones for a 15-GHz input trigger (pulse repetition rate) is shown in Fig. 2.15(c). Fig. 2.15(c) shows a flat response over the WR-3.4 and WR-2.2 bands with 10-dB bandwidth of more than 300 GHz. It is worth mentioning that THz tones up to 1.14 THz are detected with 1-Hz RBW in the measurement setup of Fig. 2.15(a); however, since the calibration data and power meters were not available, they are not reported in Fig. 2.15(c). Strong deviation from simulation results is observed above 750 GHz, which implies poor device modeling of PIN diode in this frequency range. Note that, simulation results are based on foundry PIN diode model, and post layout parasitics are included.

High spectral purity of the radiated tones is critical for many sensing applications [55, 9]. Two main parameters, 10-dB linewidth, and phase noise are a good indication of spectral purity. The spectra of received THz tones and the corresponding SNR (at 10 cm distance) of each one are shown in Fig. 2.16(a). As shown, the radiated tones all show a 10-dB linewidth of less than 2 Hz. This enables tuning the frequency of each tone with a resolution of less than 2 Hz. The SNR of the THz tones are shown in Fig. 2.16(b) for 1-Hz resolution bandwidth (RBW), where the noise floor is determined by the conversion loss of each VDI mixer. It can be observed that the highest SNR is achieved in WR-2.2 band. In the WR-1.0 band,

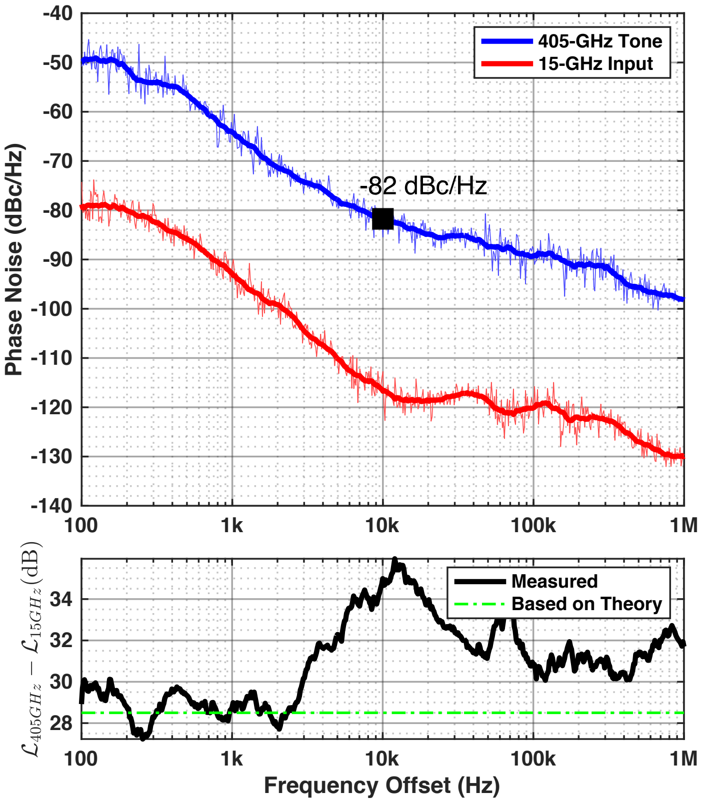

Figure 2.17: Measured phase noise of the tone at 405 GHz and fundamental frequency of 15 GHz.

the SNR decreases, due to high conversion loss of the VDI mixer and lower radiated power of the pulse transmitter. Nonetheless, more than 10 dB SNR is achieved at 1.1 THz with 1-Hz RBW when the distance is 10 cm.

Phase noise is another critical specification in THz radiators. In this pulse-based system, the repetition-rate of the radiated pulses is locked to a stable external source. Neglecting the noise contribution of the circuit components, the phase noise of the generated harmonics can be ideally calculated using the following:

$$\mathcal{L}_{Nf_0} = 20log\ N + \mathcal{L}_{f_0} \tag{2.5}$$

where $\mathcal{L}_{f_0}$ and $\mathcal{L}_{Nf_0}$ are the phase noise at the fundamental frequency (pulse repetition-rate) and Nth harmonic, respectively. For instance, for the repetition-rate of 15 GHz, the phase

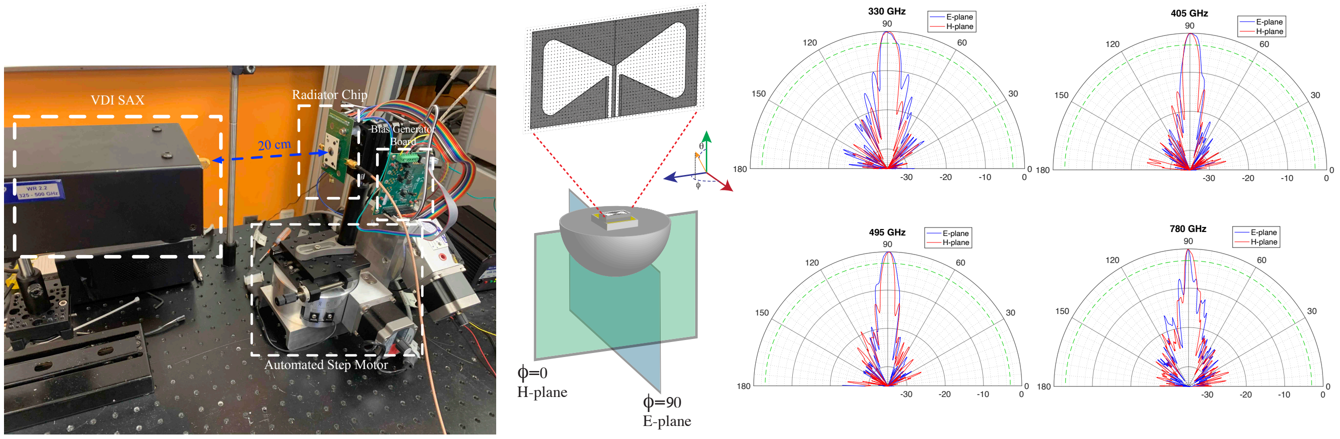

(a)

(b)

Figure 2.18: (a) Setup for radiation pattern measurement of the pulse radiator. (b) Measured radiation pattern at 330, 405, 495, 780 GHz.

noise of the 27th tone at 405 GHz is 28.6 dB above the phase noise of the 15-GHz tone, based on (4.18). Fig. 4.24 shows the measured phase noise at 405 GHz and 15 GHz. For the offset frequencies of less than 1 kHz, the measured phase noise at 405 GHz is 28 dB above the fundamental frequency of 15 GHz, which is close to what (4.18) suggests. However, for higher offset frequencies, the noise contribution of the circuit blocks causes deviation from the ideal case.

Radiation pattern and antenna directivity are important for many applications. Directive beams can be used for sensing, without needing to collimate the beams. Therefore, the measurement setup can be compact, as it does not require additional components for collimation, such as off-axis parabolic (OAP) mirrors and Teflon lenses. The measurement setup of Fig. 2.18(a) is used to measure the radiation pattern. In this automated setup, the radiator is rotated with 0.5° precision using a step motor, and the corresponding power is captured using a Keysight N9030A spectrum analyzer with 100-Hz RBW. The measured radiation pattern is shown in Fig. 2.18(b). The estimated directivity, based on the formula provided in [56], is 24.6, 26.3, 27.5, and 32 dBi at 330. 405, 495, and 780 GHz, respectively.

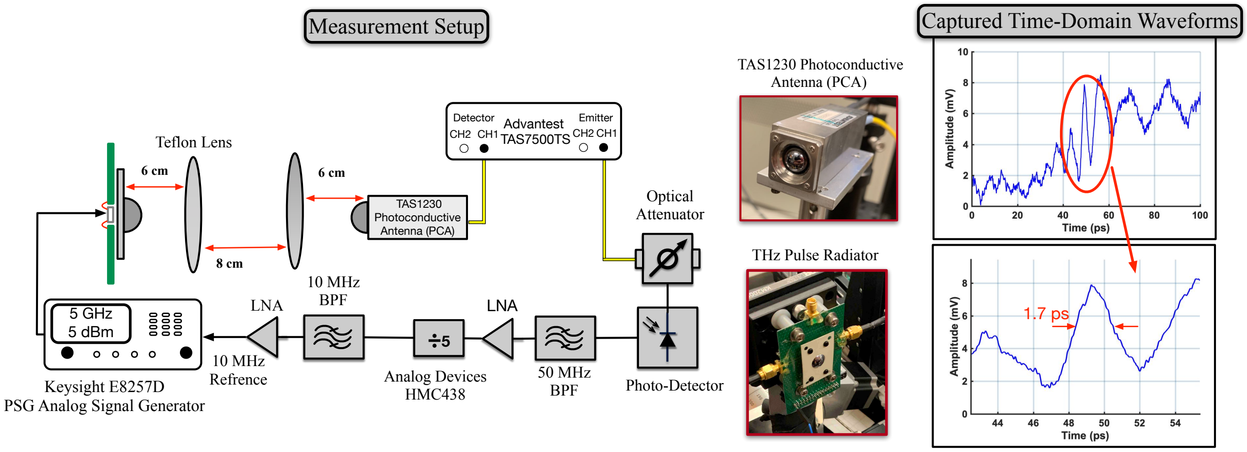

Figure 2.19: Measurement setup for time-domain characterization of the radiated pulses.

2.4.2 Time-domain characterization of Pulse Radiator

Due to wide bandwidth of the radiated pulses, capturing the radiated pulses in the time domain is not feasible using electronic oscilloscopes. Optical sampling systems, on the other hand, can operate over a wide band, and therefore can be employed to record the THz waveforms. To achieve this, the measurement setup of Fig. 2.19 is designed, in which the Advantest TAS7500TS THz optical sampling system is used to receive the pulses. For receiving pulses, synchronization between the signal generator and the optical system is critical; otherwise, due to high jitters and frequency drift of the optical system, the received pulses vanish after averaging. To achieve this, one channel of the optical system is converted into an electronic signal and divide by 5 to provide the reference signal for the signal generator. Although the radiated pulses are synchronized with the optical sampling system, due to jitters of the laser low-pass filtering still occurs after averaging. Captured time-domain waveforms after 256 averagings are shown in Fig. 2.19. The radiated pulses present a FWHM of 1.7 ps. Although the measured FWHM is larger than the real FWHM because of averaging and jitters, it gives a good estimate of the quality of the generated pulses, and overall performance of the radiator.

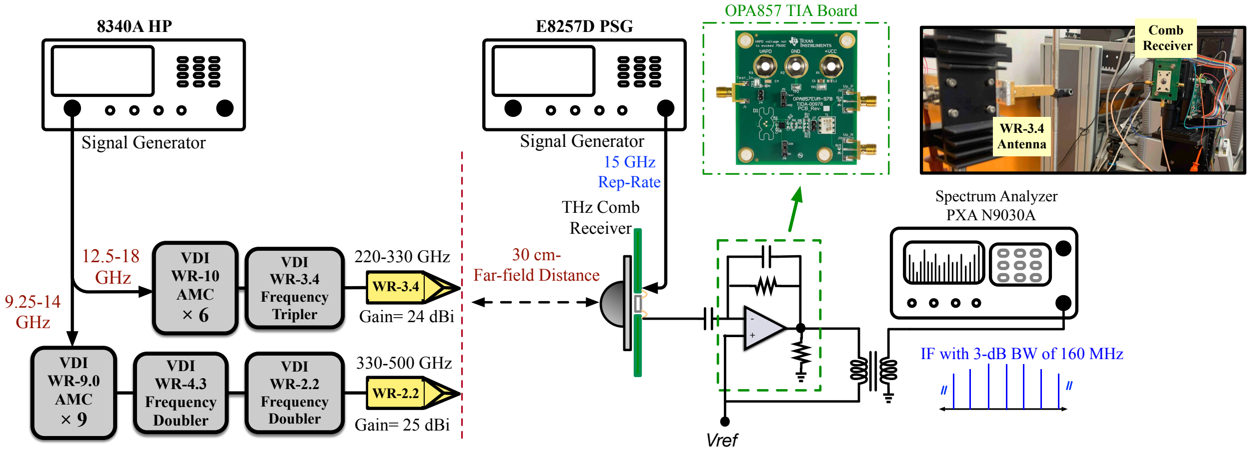

Figure 2.20: Measurement setup for frequency-domain characterization of the broadband comb receiver.

2.4.3 Frequency-Comb Receiver Characterization

The frequency-comb receiver is characterized using sources with calibrated output power for different bands covering 220 to 500 GHz. Since the radiated power from the sources and gain of the antenna are known, the power received by the receiver antenna can be calculated using the Friis transmission formula to derive conversion loss and sensitivity. The setup for frequency characterization is shown in Fig. 2.20. A ×6 WR-10 AMC and a VDI WR-3.4 tripler are cascaded to cover 220 to 330 GHz. In addition, a VDI WR9.0 SGX module is configured with external multipliers to extend the frequency coverage up to 500 GHz. Since in this receiver, the current of the SBD is modulated and contains the mixing product, a transimpedance amplifier (TIA) is used to amplify the current and convert it into voltage. The TIA presents low input impedance at IF frequencies that prevents loading the cathode of SBD. Fig. 2.21(a) shows the measured IF tones for received RF at 270, 315, 360, 405, 450, and 480 GHz with the 1-kHz RBW. In this measurement, the bias of SBD is changed at each frequency point to maximize the received power. Using the Friis formula, the SSB-Conversion Loss (CL), sensitivity and noise figure (for 1-kHz RBW) are measured and shown in Fig. 2.21(b), derived by the following equations:

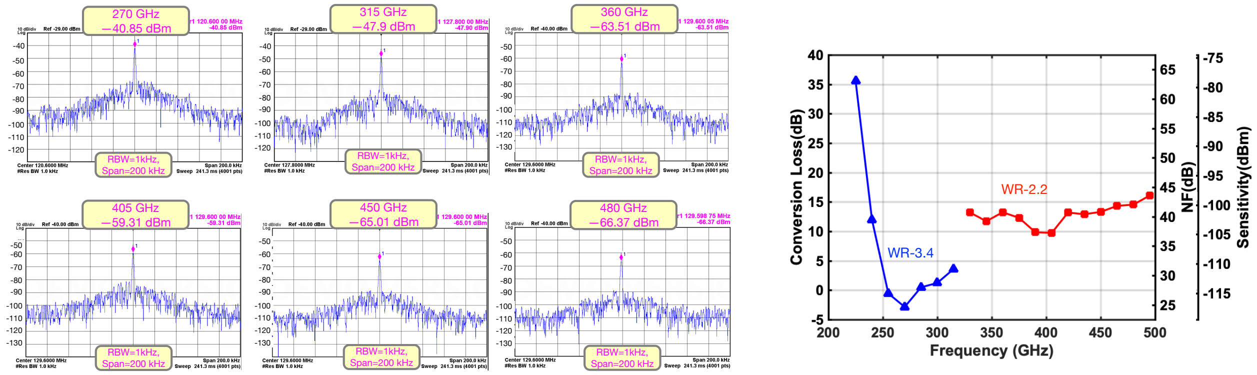

(a)

(b)

Figure 2.21: (a) Spectrum of IF tones in WR-3.4 and WR-2.2 bands, (b) calculated conversion loss, noise figure, and sensitivity.

$$CL_{|dB} = P_{R,ant|dBm} - P_{IF|dBm} \tag{2.6}$$

$$Sensitivity_{|dBm} = 10log(\frac{1\ kHz}{RBW}) + RX_{IF-noisefloor|dBm} + CL \tag{2.7}$$

$$NF = RX_{IF-noisefloor} - SA_{noisefloor} + CL \tag{2.8}$$

where received power of receiver antenna, $P_{R,ant}$ is defined as follows:

$$P_{R,ant|dBm} = P_{t|dBm} + G_{t|dBi} + G_{r|dBi} - L_{path|dB} \tag{2.9}$$

Here P_t is radiated power by the source, and L_{path} is the path loss derived using Friis transmission equation. The amount of the radiated power at each frequency point is known from the device datasheet. G_t is the gain of the source antenna, which is 24 and 25 dBi for the WR-3.4 and WR-2.2 bands, respectively. G_r represents the gain of the receiver antenna, which is obtained from the simulation results. Aforementioned derivation for CL excludes the antenna loss based on the simulation results (Fig. 2.10(c)), and mainly focuses on the performance of the receiver rather than on the antenna. Observed Noise floor on the spectrum analyzer with 1-kHz RBW is -114.5 dBm (with TIA) after 1000 averagings for sensitivity and noise figure measurements. Although the TIA improves the conversion gain, the overall sensitivity drops by 3 to 5 dBs, due to the noise contribution of TIA. The choice

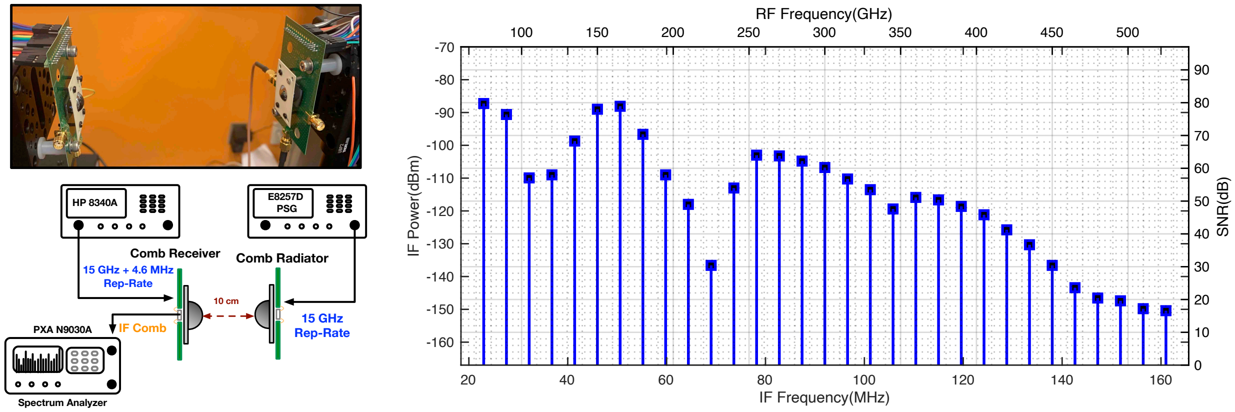

(a) (b)

Figure 2.22: (a) Chip-to-chip dual-comb measurement setup, (b) measured IF-comb power and signal to noise Floor (1-Hz RBW) for chip-to-chip dual-comb measurement.

of IF frequency range is important, as at low IF frequencies flicker noise dominates the noise floor and deteriorates the sensitivity. Therefore, IF frequency is chosen in a range, below the IF 3-dB BW, wherein flicker noise is not a contributing factor. For CW measurements, IF is at 129.6 MHz. IF bandwidth is limited by the external TIA. In these measurements, a 3-dB bandwidth of 160 MHz was observed; however, by lowering the gain of TIA, the 3-dB bandwidth can be increased to as high as 250 MHz.

2.4.4 Dual-Comb Measurement

In this section, the measurement setup of Fig. 2.22(a) is used to perform a dual-comb measurement from 75 to 525 GHz. The repetition-rate of the radiator and receiver are set to 15 GHz and 15 GHz+4.6 MHz. Therefore, an IF frequency comb is received such that the spacing between adjacent tones is 4.6 MHz. For instance, the IF tone at 92 MHz corresponds to the received RF tones of 300 GHz. Fig. 2.22(b) shows the received IF tones and their corresponding RF frequencies. Note that, for each frequency the DC bias of SBD is changed across THz bands to achieve the highest sensitivity.

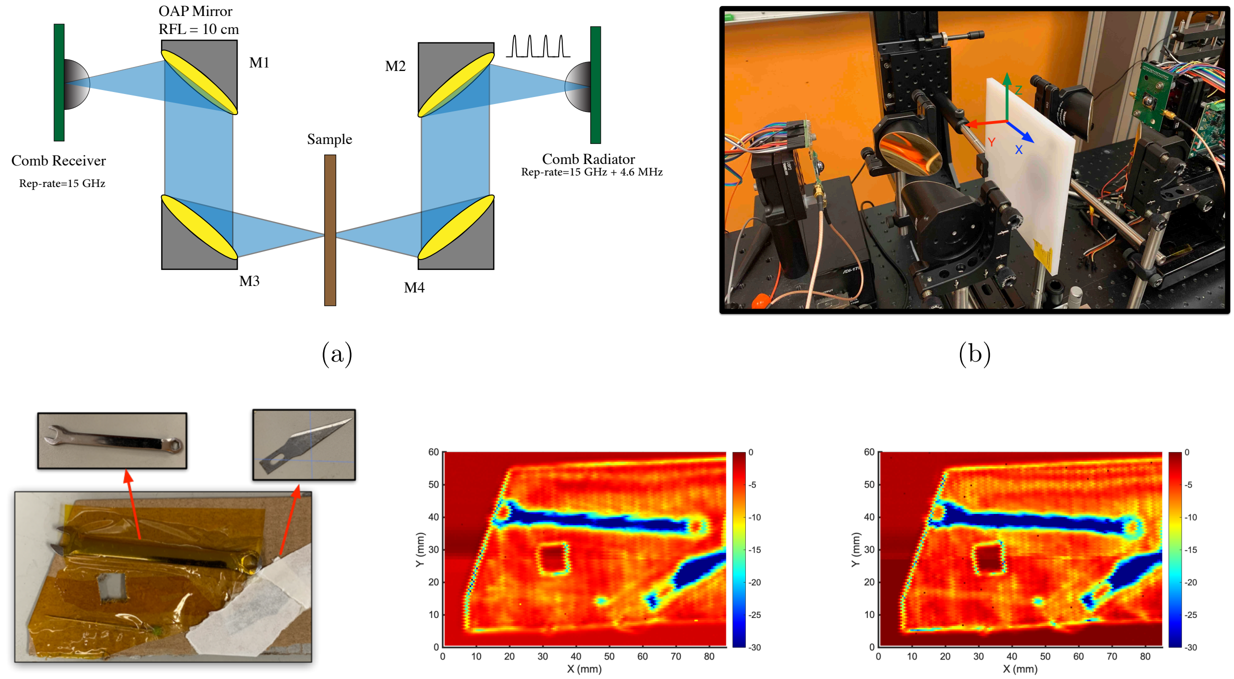

(a)

(b)

(c)

(d)

(e)

Figure 2.23: (a) Imaging setup block diagram, (b) Photo of the measurement setup. (c) Imaging sample, which consists of a blade, a wrench and a needle, which are placed on a hard paper with a square hole in the middle. (d) Captured image at 330 GHz. (e) Captured image at 450 GHz.

Moreover, Fig. 2.23 demonstrates dual-comb hyperspectral imaging as one of the potential applications of this work. In this setup, Off-Axis Parabolic (OAP) mirrors are used to collimate and focus the THz wave on the imaging sample. The position of the sample is controlled via two automatized rails on the XZ plane. The sample is imaged line by line with 500 um steps. Fig. 2.23(d),e shows the images of the sample at 330 and 450 GHz. For each frequency, the biasing of SBD at the receiver side is tuned to achieve the highest SNR. The achieved SNR is above 30 dB for each frequency; however, to better illustrate the contrast, the dynamic range of captured images is set to 30 dB.

Table 2.1: Comparison of THz pulse radiators

Reference	**This work**	**[17]**	**[39]**	**[37]**	**[57]**	**[58]**
Highest Measured Frequency(GHz)	**1140**	1100	1100	N/A	110	216
Pulse Width (FWHM)	**1.7 ps[†]**	1.7 ps	1.9 ps	8.8 ps	26 ps	2.6 [*]
Repetition Rate (GHz)	**15[‡]**	10.5[‡]	6[‡]	8	1.52	108
Highest EIRP above 320 GHz (dBm)	**-10**	-28	-34	N/A	13@110GHz	5@214GHz
Die Area (mm^2)	**0.48**	0.48	0.47	0.63	6.16	8.37
DC power (mW)	**40**	45	105	146	1400(TX+RX)	1100
Generation Technique	**PIN diode**	PIN diode	D2I	Reflection-based	Oscillator-based	Oscillator-based
Technology	**90-nm SiGe BiCMOS**	130-nm SiGe BiCMOS	130-nm SiGe BiCMOS	110-nm CMOS SOI	130-nm SiGe BiCMOS	65-nm-LP CMOS

[†] Optical sampling system jitters broaden the measured pulses.

[‡] Maximum repetition rate the pulse generator can operate.

[*] Based on simulation results.

2.5 Conclusion

This work demonstrates a fully integrated low-power solution for high-resolution spectroscopy and broadband sensing applications. Design of THz comb/pulse radiator and receiver as an integral part of dual-comb technique implementation are elaborated in detail. PIN diode reverse recovery is used to generate and radiate bipolar pulses over a wide band ranging from 10s of GHz up to 1.14 THz. This technique boosts the radiation power and EIRP, which not only surpasses the output power of the state-of-the-art pulse radiators, but also reaches to CW radiators. In addition, extremely narrow spectral line-width and low phase noise make this work an excellent choice for ultra-high-resolution sensing applications. Moreover, the area-efficient and low-power topology allows scaling up the design for large array implementation. Table 2.1 compares the pulse radiator of this work with previous

Table 2.2: Comparison of sub-THz Heterodyne receivers

Reference	**This work**	**[46]**	**[18]**	**[45]**	**[59]**	**[60]**	**[61]**	**[62]**
Frequency(GHz)	**220-500**†	160–1000	50–500	50–280	220–330	115–325	315–328	240
Minimum Sensitivity* **(dBm), 1-kHz RBW**	**-117**‡	-100	-105	-73	-129	-115	-124	-102
Chip Input LO (GHz)	**4-15**	18.3	4-10.5	3-5	45-46.7	28.75-81.25	17.7	0.075
RX Tuning Range (GHz)	**280**	840	450	230	110	210	13	2.4
Die Area (mm^2)	**0.48**	1.32	0.48	0.56	6	0.9	1.3	2.8
DC Power (mW)	**38**	600	52	34	1700 (TX+RX)	36	56	212
Technology	**90-nm SiGe BiCMOS**	250-nm SiGe BiCMOS	130-nm SiGe BiCMOS	65-nm CMOS	45-nm CMOS SOI	65-nm CMOS	65-nm CMOS	65-nm CMOS

*Minimum sensitivity of the mixer only (excluding the loss of antenna)

†Frequency range of chip characterization. Dual-comb measurement is performed from 75 GHz to 525 GHz.

‡Including noise contribution of external TIA, which affects sensitivity by 3–5 dB.

state-of-the-art THz pulse radiators. For THz detection, SBD is utilized in a heterodyne architecture that enables receiving any arbitrary frequency spectrum up to 500 GHz with a sensitivity ranging from -117 to -99 dBm (1-kHz RBW). A comparison between the receiver of this work and previous works is provided in Table 2.2. Broadband receiver in conjunction with pulse/comb radiator provides a compact, low-cost, and high-resolution solution for hyperspectral sensing, imaging, and spectroscopy applications.

CHAPTER 3

Power Efficient PIN Diode-based CW THz Radiator in 90-nm SiGe BiCMOS

3.1 A Highly Power Efficient 2×3 PIN Diode-based Intercoupled THz Radiating Array at 425 GHz with 18.1-dBm EIRP in 90-nm SiGe BiCMOS

3.1.1 Introduction

Efficient THz generation in silicon technologies has been of great interest over the recent years, as it enables an integrated low-cost solution for sensing, radar, communication, and spectroscopy [63, 64, 65]. Due to the limited f_t/f_{max} of transistors, direct THz generation using a fundamental oscillator is not feasible; therefore, various approaches have been developed based on harmonic extraction and the frequency multiplication of a fundamental oscillator [66]. In these techniques, the nonlinearity of transistors is utilized to generate higher harmonics from a fundamental oscillator or frequency-multiplier cells; however, such systems have a poor efficiency and low radiated power due to device limitations. To compensate for the low generated power, a coherent array scheme is preferred to increase EIRP and radiated power. Adjusting the phase and locking the frequency of elements for coherent operation are important factors in array architectures, which can be performed through central LO distribution [67] and mutual coupling [68]. LO distribution can cause phase mismatch between elements and significantly increases the DC power consumption by adding more blocks. Mutual coupling through injection locking can maintain phase alignment. However, this type of coupling has low tuning range, which makes it challenging to synchronize elements over a broad frequency range. In this work [19], a technique for THz CW generation is presented, in which, instead of relying on transistor nonlinearity, a PIN diode is used in the reverse recovery mode for strong harmonic generation. A PIN diode, similar to a step recovery diode (SRD), benefits from a sharp reverse recovery and is highly nonlinear in the recovery mode, which enables efficient THz harmonic generation by upconverting the output of a mm-wave oscillator without requiring additional blocks and multipliers. The PIN-based array consists of 2×3 elements, where differential Colpitts oscillators are used as the core to push the PIN diodes into reverse recovery. Array elements are intercoupled using a collective coupling approach that enables wide tuning range and phase match between elements. The PIN-based array achieves a radiated power of 0.31 mW and 18.1 dBm EIRP at 425 GHz.

3.1.2 Design of the THz Radiator Array

In this design, the core of each radiating element consists of a pair of Colpitts oscillators with differential oscillation at the fundamental frequency of 80 to 92 GHz. The schematic of the oscillator is shown in Fig. 3.1. The biasing current of the oscillator is set by adjusting V_{be}, which determines the oscillation frequency through changing the transistor base-emitter capacitance. At the emitter of the transistor, a resistor in conjunction with a quarter-length T-line is used. Note that utilizing a resistor instead of an active current source at the emitter of the transistor results in a lower phase noise and allows for a higher swing at the emitter of the transistors. The oscillators of each array elements are locked to the adjacent oscillators through a coupling network consisting of T-lines and capacitors. This mutual coupling between oscillators reduces the phase noise. A stable phase match between oscillators is critical to achieve high directivity in an array. In this work, the design targets the differential oscillation between any two adjacent oscillators in a collective fashion. This causes the array elements to radiate tones with the same phase (same V_{be} for all elements).

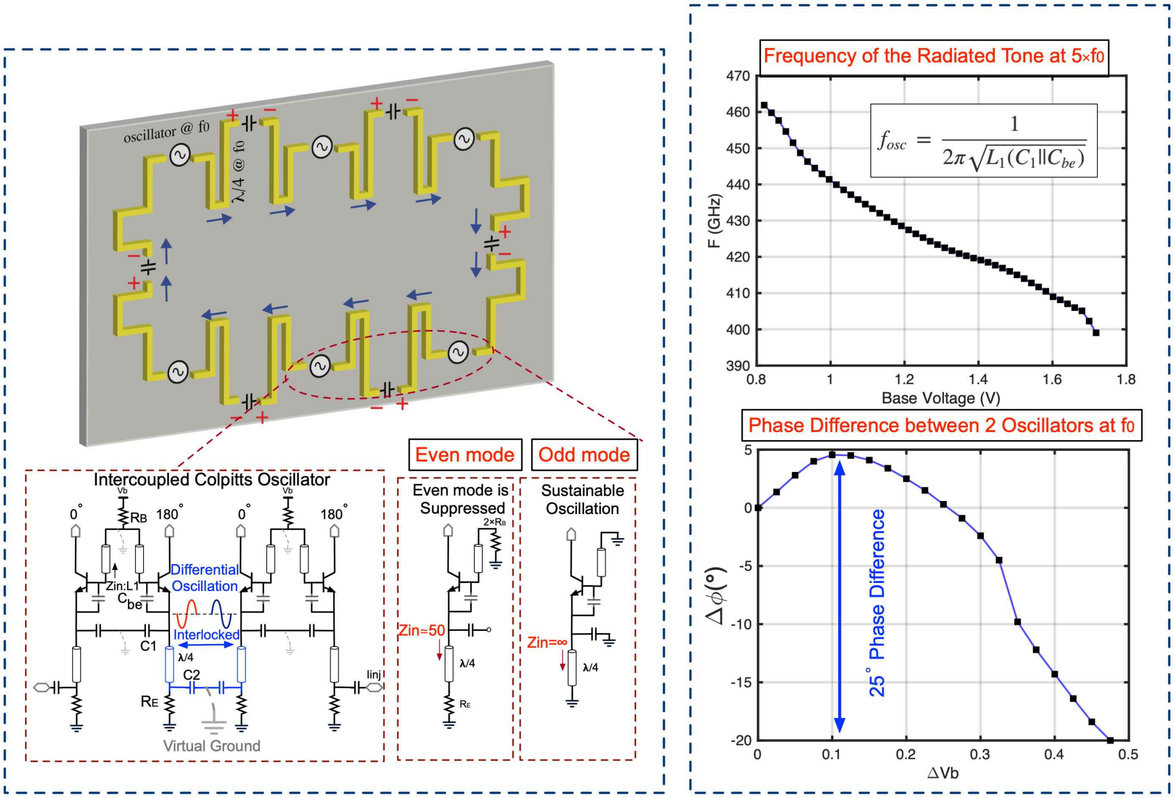

Figure 3.1: Architecture of the intercoupled oscillator array. The oscillators have sustainable oscillations in the odd mode, while any even-mode oscillation is suppressed by the base and emitter resistors. This architecture enables a wide frequency-tuning range and a large phase shift between elements.

As shown in Fig. 3.1, R_B and R_E suppress the oscillation by decreasing the Q-factor of the oscillator in the even mode, while allowing the odd mode of oscillation between two adjacent elements. This technique of coupling allows wide tuning range and stable phase matching between adjacent elements. Figure 3.1 shows the tuning range of 14.6%, where the radiating tone (5th harmonic) can be tuned from 399 to 462 GHz. The oscillators remain locked even when V_{be} of the transistors are different. In this case, as shown in Fig. 3.1, a phase shift occurs between two adjacent oscillator pairs based on ΔV_{be}, which can be used for beam

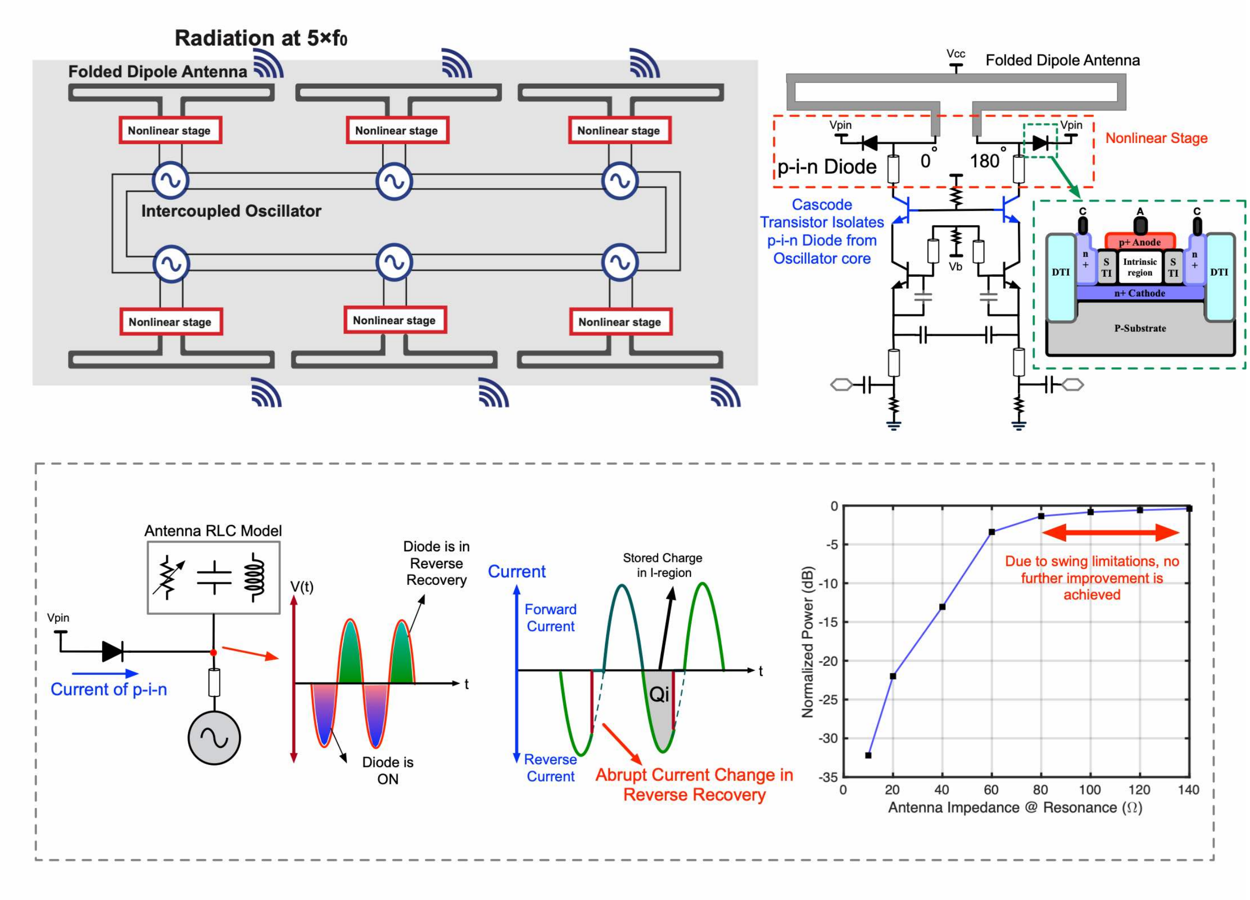

Figure 3.2: Schematic of the radiating cell and the illustration of harmonic generation using the nonlinearity of a PIN diode in reverse recovery in the array scheme. Simulations suggest higher antenna impedance improves the generated THz power.

steering. Furthermore, this architecture can be scaled up to implement a large array.

To generate tones above f_{max} of the transistor, a PIN-diode device is utilized as shown in Fig. 3.2. In this architecture, the PIN diode functions as an ultra-fast current switch in reverse recovery, which abruptly changes the current of the antenna resulting in a high nonlinearity and strong harmonic generation. To drive the PIN diode with the output of the oscillator, a cascode transistor is used to provide some degree of isolation between the PIN diode and the oscillator core. The cascode transistor prevents the disruption of the oscillator core, which can be caused by strong swings at the antenna input. For the efficient

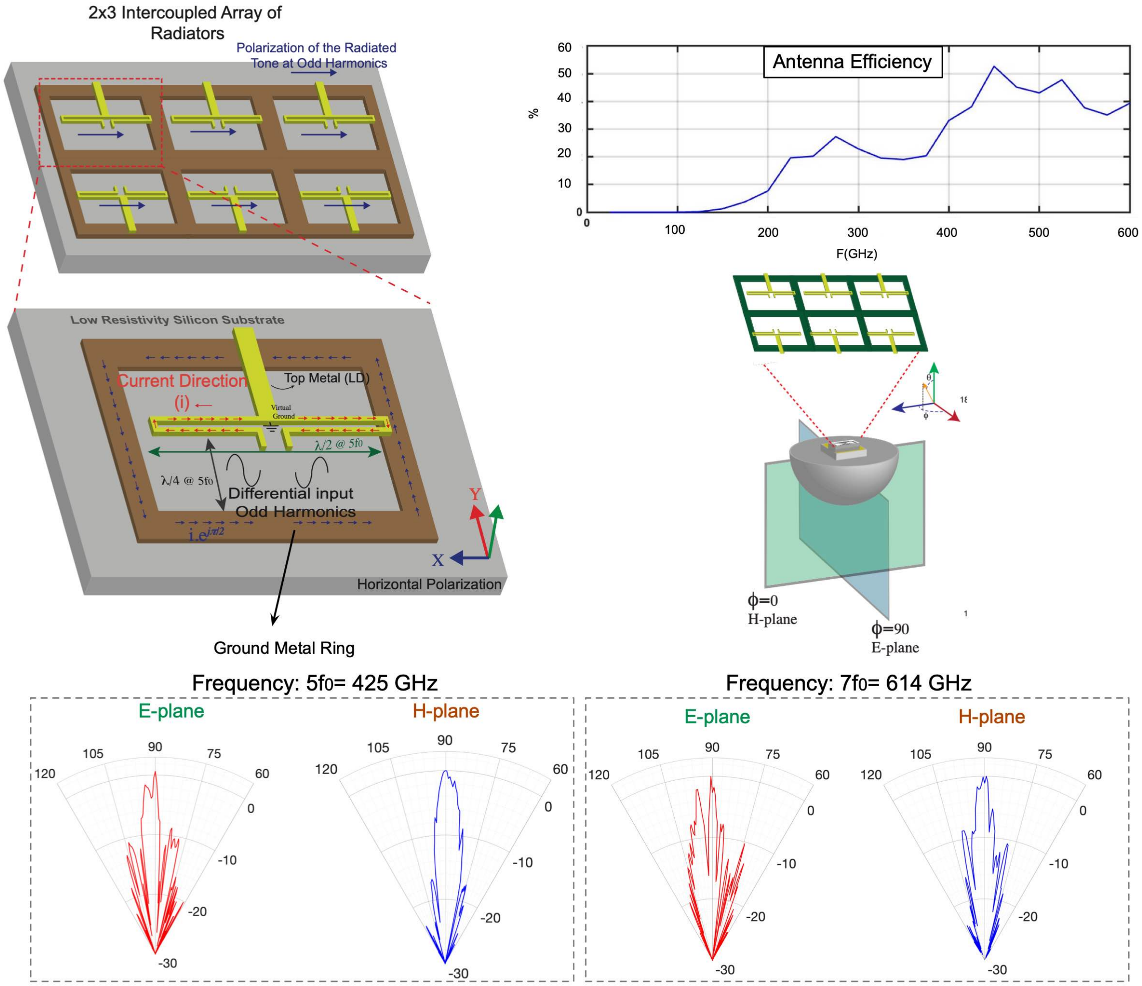

Figure 3.3: Structure of the folded-dipole antenna and measured radiation patterns at the 5th and 7th harmonics.

THz harmonic generation, the antenna impedance should be optimized. To calculate the optimum impedance of the antenna, an RLC model of the antenna at the 5th harmonic (420 GHz) is derived and used. Based on this analysis, the folded dipole antenna of Fig. 3.3 is chosen, which provides a proper impedance matching without requiring an additional matching network. The antenna length is $\lambda/2$ at 425 GHz for optimum radiation at the 5th harmonic. Although the antenna is optimized for the 5th harmonic radiation, significant radiation is observed at higher odd harmonics (Fig. 3.4). To improve the efficiency of the

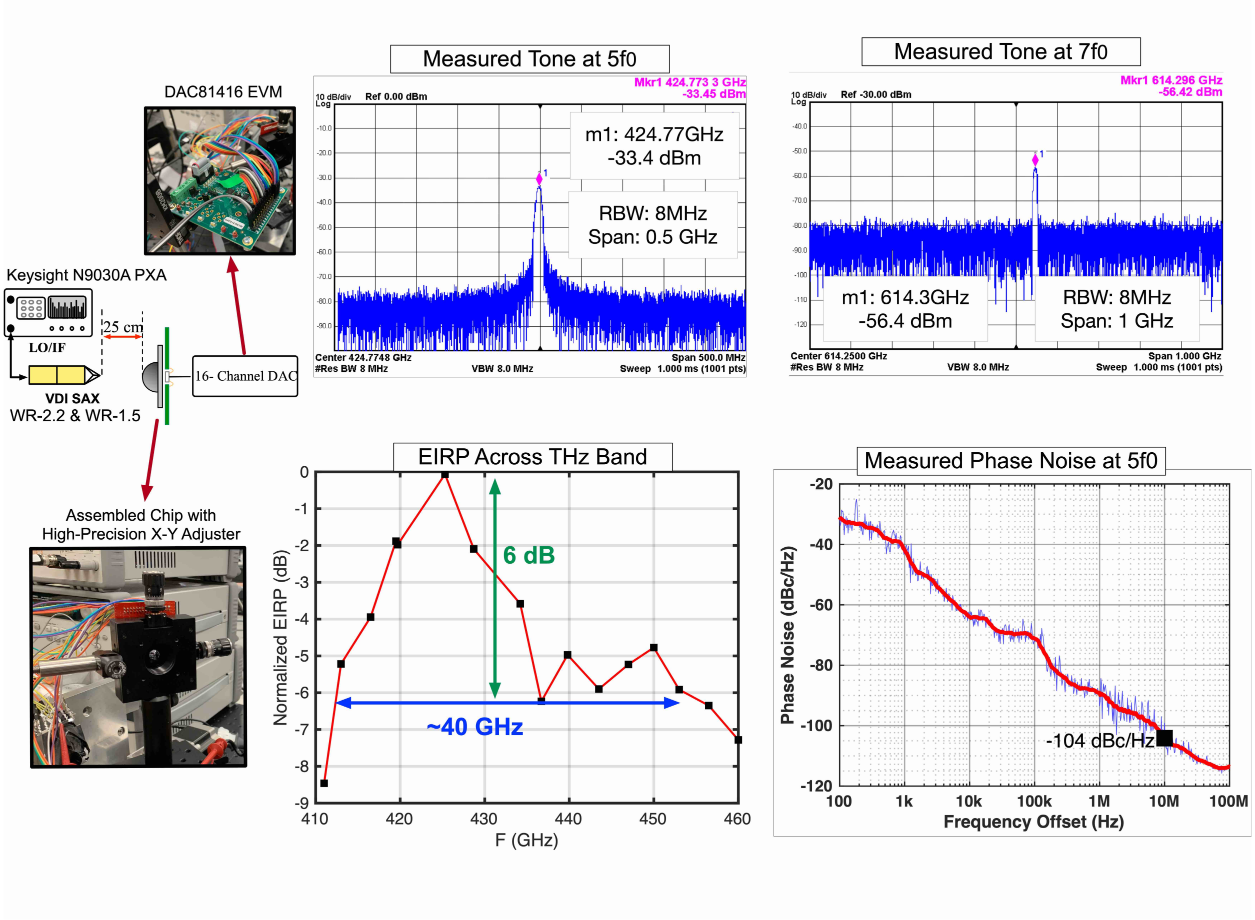

Figure 3.4: Measurement setup for frequency-domain characterization. Measured output tones at the 5th and 7th harmonics. Normalized EIRP vs frequency. Measured phase noise of the intercoupled free-running oscillators.

folded dipole antenna, a proper return path is required. Providing a return path with a 90° phase difference prevents the direct coupling of the antenna return current to the lossy substrate [5]. Therefore, a metal ring with a $\lambda/4$ spacing from the antenna is used as the return path, resulting in an improvement in the radiation efficiency and bandwidth. The radiation efficiency ranges from 30 to 52% in the 400-to-460GHz range using a hemispherical silicon lens. The radiation pattern is measured by using a step motor with half-degree precision, and the results are shown in Fig. 3.3 at 424.77 and 614.3 GHz. The estimated directivity at these frequencies is 23 and 27 dBi, respectively.

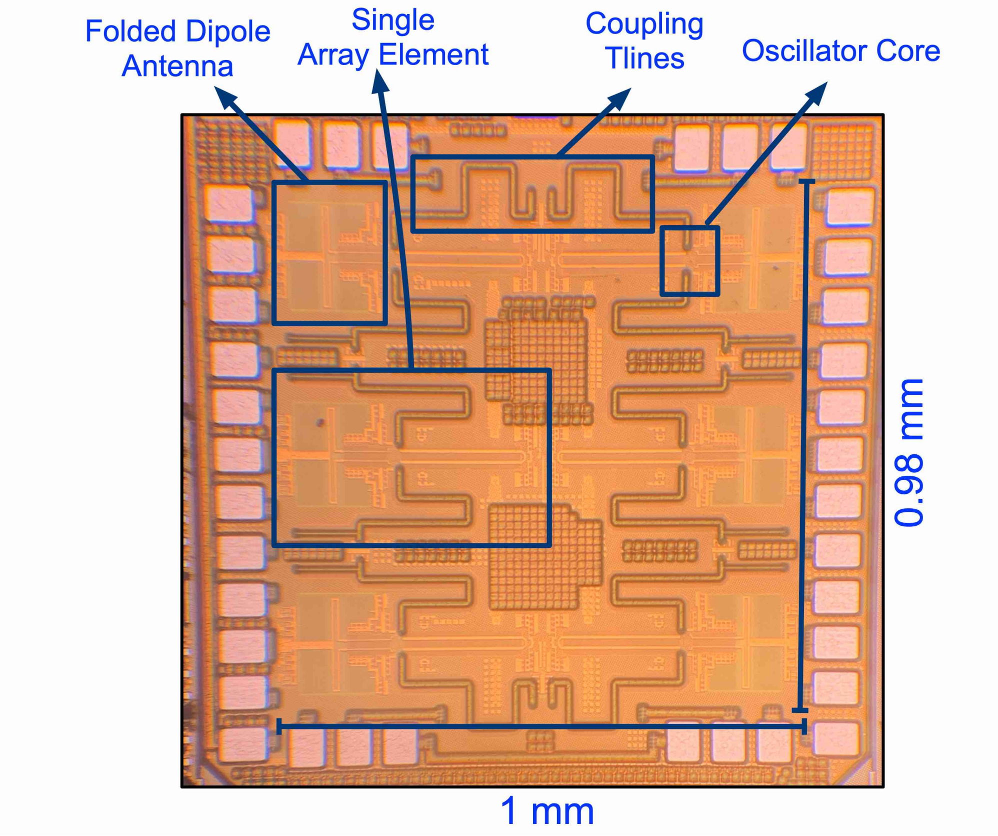

Figure 3.5: Die micrograph.

3.1.3 Measurement Results

The design is fabricated in the GlobalFoundries 90nm SiGe BiCMOS 9HP process with a total area of 0.98 mm2 (excluding pads). The power consumption of the chip is 400 mW. The die micrograph is shown in Fig. 3.5. Figure 3.4 shows the measurement setup for frequency-domain characterization. The received tones at 424.77 and 614.3 GHz are -33.4 and -56.4 dBm, which correspond to the EIRP of 18.1 and 1.4 dBm, respectively, after de-embedding the polarization loss factor, VDI SAX conversion loss, and cable loss. VDI SAX is calibrated using a PM5 power meter and a VDI WR2.2 source. Moreover, EIRP fluctuates less than 6dB over 40 GHz bandwidth. Note that the oscillation is sustained over more than a 60 GHz frequency-tuning range. The measured phase noise of the radiated tone

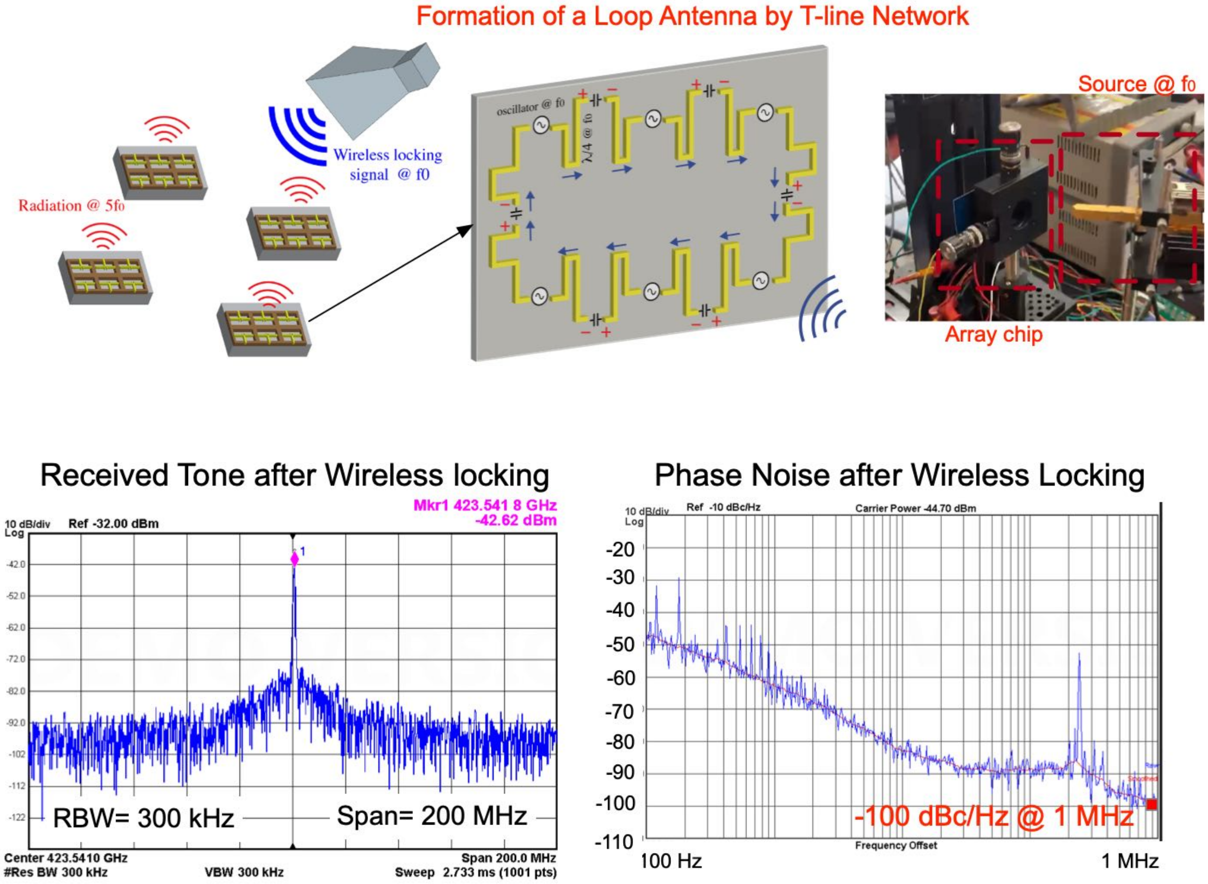

Figure 3.6: Formation of a loop antenna by T-lines and the demonstration of wireless locking using an external source at the fundamental frequency.

at 424.77 GHz is -104 dBc/Hz at a 10 MHz offset frequency in the free-running mode. As shown in Fig. 3.6, the T-line network, which connects the oscillators to each other can form a loop antenna at f_0 enabling synchronization by a wireless external source [69, 70]. This feature allows synchronizing multiple independent chips at f_0 to form a large-scale radiator array at $5 \times f_0$. Figure 3.6 shows the spectrum and phase noise after locking by an external source. In this case, the locking range is 200 MHz using a 10 dBm source with a 25 dBi antenna gain at a 20 cm distance from the top side of the chip.

Table 3.1: Comparison between this work and previously published silicon-based THz sources.

Reference	This Work	[29]	[71]	[54]	[72]	[73]
Frequency(GHz)	**425**	416	668	459	344	338 240
EIRP (dBm)	**18.1‡**	14	7.4	19.3	4.9	17.1
Radiated Power (mW)	**0.31**	0.5	0.025	0.66	0.21	0.79
Tuning Range (%)	**14.6**	1.7	2.3	8.9	15.1	2.1
Source Type	**2×3 PIN PIN Array**	4×4 Array	4×2 Array	25-element Array	2×2 Array	4×4 Array
Phase Noise (dBc/Hz) @ 10 MHz	**-104**	-	-93	-100.6	-93.1	-93@1MHz
Die Area (mm^2)	**0.98**	4.1	0.87	3.94	1.2	7.2
DC-to-THz Efficiency (%)	**0.08**	0.03	0.02	0.04	0.04	0.05
Technology	**90-nm SiGe BiCMOS**	65-nm CMOS	40-nm CMOS	65-nm CMOS	130-nm SiGe BiCMOS	65-nm CMOS
DC Power (mW)	**400**	1450	99.7	1470	450	1540

3.1.4 Conclusion

In Table. 3.1, a comparison between this work and recent silicon-based THz sources is presented. This work achieves the highest DC-to-THz efficiency while producing a high EIRP among other designs in Table 3.1. The array has a small area and low power consumption. In addition, the interlocked oscillators used in this work allow scaling up the design and improve the phase-noise performance. Furthermore, the interlocked oscillator architecture provides more than 14% frequency-tuning range (a 60 GHz tuning range at the 5th harmonic).

3.2 A 0.4 THz Efficient OOK/FSK Wireless Transmitter Enabling 3 Gbps at 20 meters

3.2.1 Introduction

With recent advancements in silicon-based mm-wave/THz systems, THz frequency bands have been of great interest for potential applications in broadband wireless communication. Silicon-based THz systems can potentially exploit unlicensed sub-THz bands and provide a low-cost solution to realize high-speed point-to-point communication links.

Despite recent advances in THz circuit design, wireless THz transmitters suffer from low efficiency due to the limited f_t/f_{max} of transistors, high DC power consumption, and low radiated power limiting the practicality of such systems for multi-Gbps communication. Different techniques have been proposed to compensate for the low generated power and to increase the data rate, including spatial orthogonality [74] and utilizing efficient modulations [75]. Moreover, PIN diode reverse recovery for THz harmonic generation has been proposed in [12] to increase the DC-to-RF efficiency.

In this section, the reverse recovery of PIN diode in conjunction with a mm-wave oscillator at 130 GHz is utilized for efficient THz harmonic generation at 390 GHz as the core of the transmitter. This transmitter supports both FSK and OOK modulations and enables a 3-Gbps point-to-point communication link over 20-meter distance. The power-efficient design of the transmitter enables various important applications including fixed-wireless, backhaul communication, and low-latency distributed computing.

3.2.2 Transmitter Architecture and Measurement Results

Fig. 3.7 shows the schematic of the transmitter block. A differential Colpitts oscillator is designed with a tunable oscillation frequency of 126 to 134 GHz. Instead of relying on varactors for adjusting the frequency, tuning mechanism is based on adjusting the current

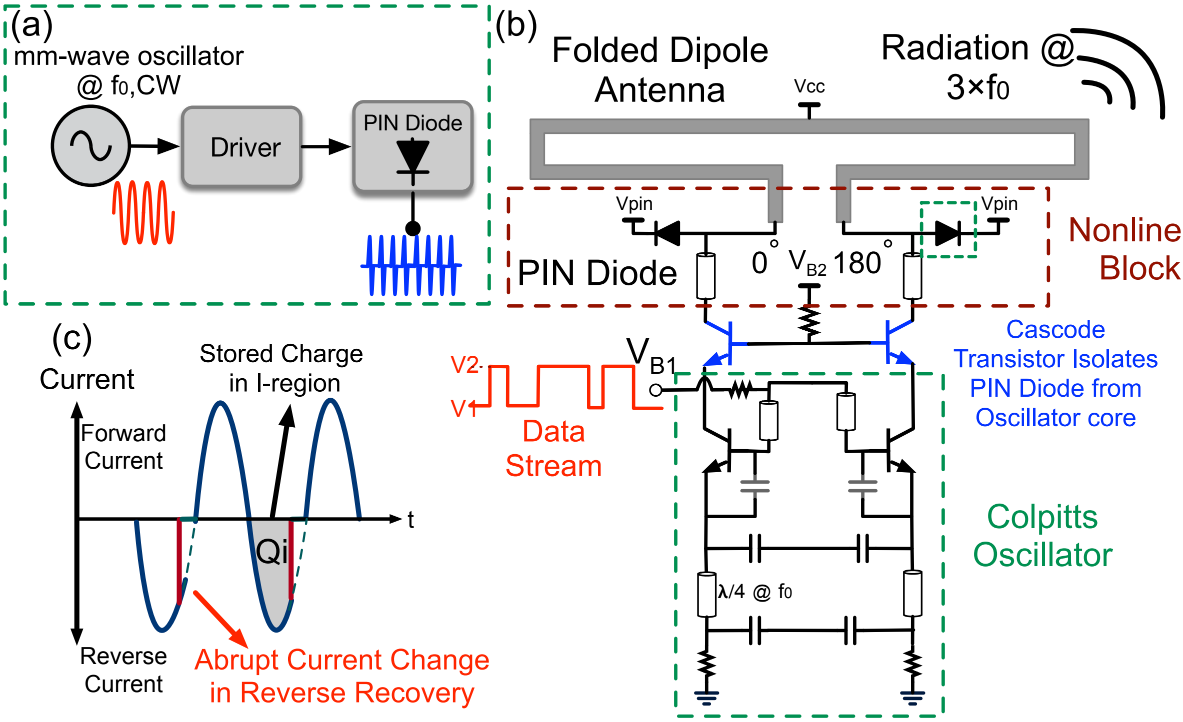

Figure 3.7: (a) Block diagram and (b) schematic of the PIN diode-based THz transmitter with (c) illustration of PIN reverse recovery.

of oscillator by tuning the Base voltage (V$_{B1}$). Due to poor performance of varactors in mm-wave, avoiding varactors enables a higher Q-factor and a larger voltage swing. The measured tuning range is reported in Fig. 3.8(b). The output frequency (at third harmonic) varies from 379 to 403 GHz by changing V$_{B1}$ from 0.9 to 1.65 V. The oscillator is connected to PIN diodes via cascode bipolar transistors. The cascode transistors provide isolation between the oscillator core and output the nodes preventing disruption of oscillation due to the non-linearity of PIN diode. The oscillator drives the PIN diodes into reverse recovery mode for the purpose of harmonic generation. Fig. 3.8(c) illustrates the reverse recovery of PIN diode. A folded dipole antenna with a resonance at the third harmonic of the fundamental frequency is used to radiate THz signals. An EIRP of 13 dBm and a phase noise of -96 dBc/Hz at 10 MHz are measured using the setup shown in Fig. 3.8(a).

To modulate the output tone, a pseudorandom data stream with OOK modulation is

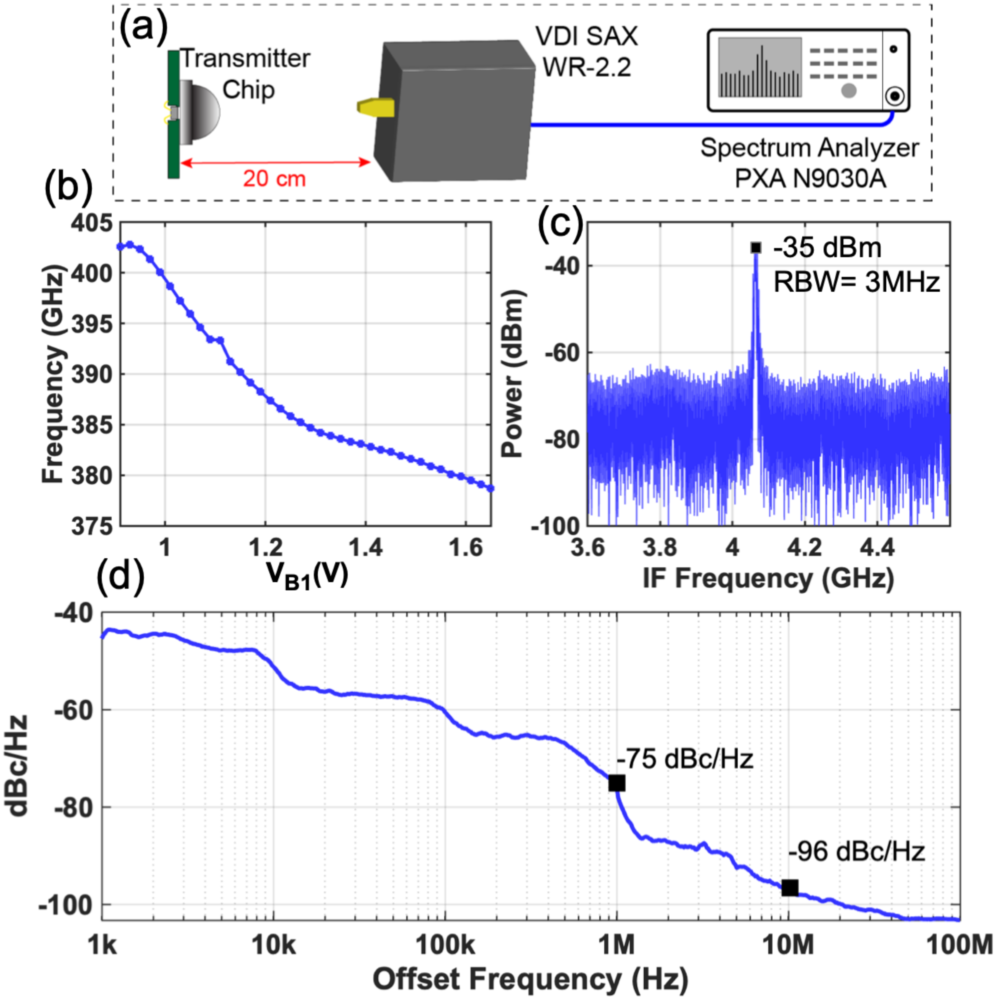

Figure 3.8: (a) Frequency-domain measurement setup. (b) frequency tuning range and (c) downconverted THz tone at 390 GHz. (d) Measured phase noise.

applied at the VB1. The transmitter enables two modulation schemes, OOK and FSK, by adjusting the DC voltage of VB1. To elaborate further, the PIN diode goes into the reverse recovery mode only if the output oscillation amplitude is large that occurs if VB1 is above 1 V. This happens when "1" is transmitted. In transmitting "0", VB1 is kept below 1 V and the transmitter does not radiate significant power. This mode corresponds to OOK modulation. FSK modulation can be applied as well simply by choosing the DC voltage of VB1 above 1 V. In this mode, "1" and "0"s generate different output frequencies determined

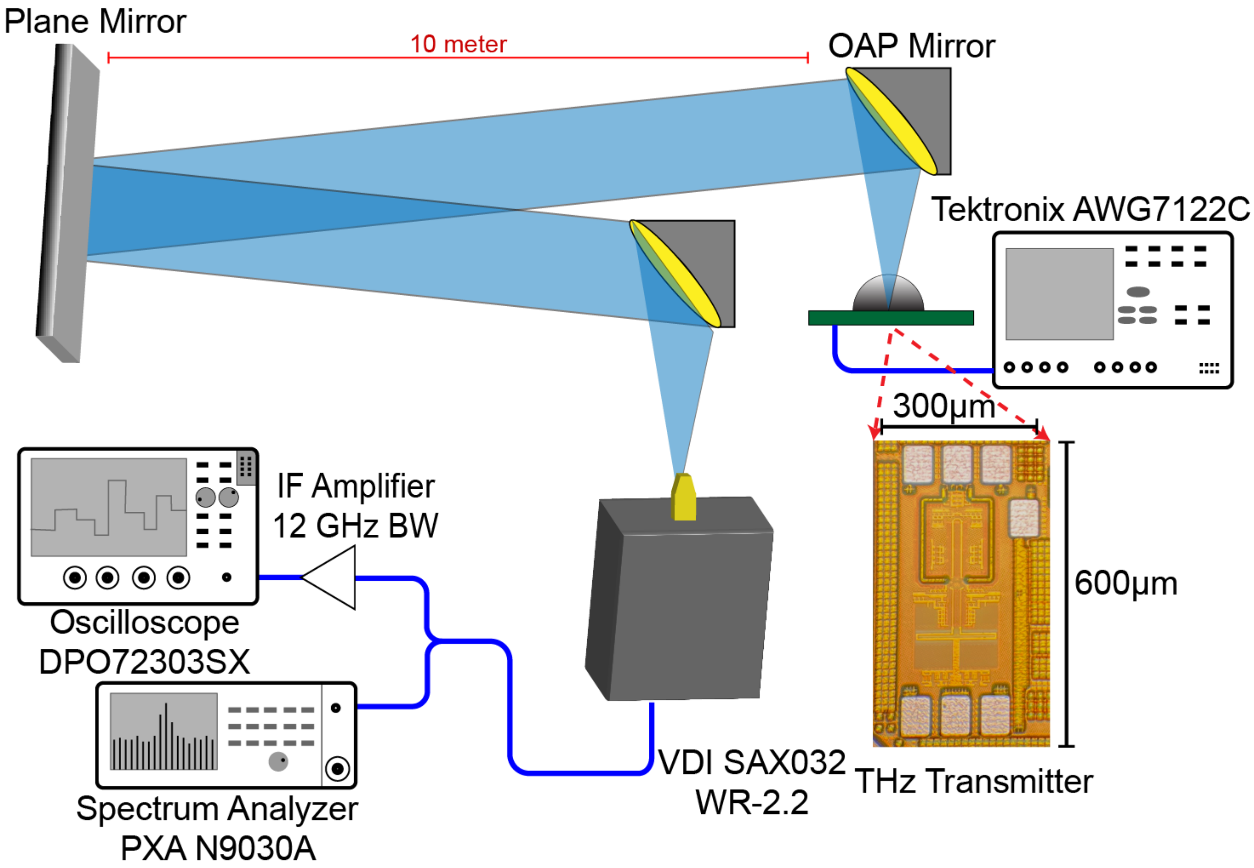

Figure 3.9: Measurement setup for 20-m communication link.

by Fig. 3.8b.

Collimating mirrors are utilized to decrease the path loss and increase the directivity for medium-range communication. Fig. 3.9 shows the measurement setup for a multi-Gbps communication link over 20-m round trip distance. Off-axis parabolic (OAP) mirrors are used to collimate and focus the THz beams at the transmitter and receiver, respectively. A plane mirror is used to reflect the THz signal at 10 m from the transmitter. The THz beams are received using a WR-2.2 VDI SAX module. The IF signal is analyzed using spectrum analyzer and oscilloscope. Fig. 3.10 shows the recorded time-domain results and eye diagrams using the oscilloscope for different data rates and modulation schemes. In addition, the IF signal is post-processed for BER calculations. No bit error was detected in

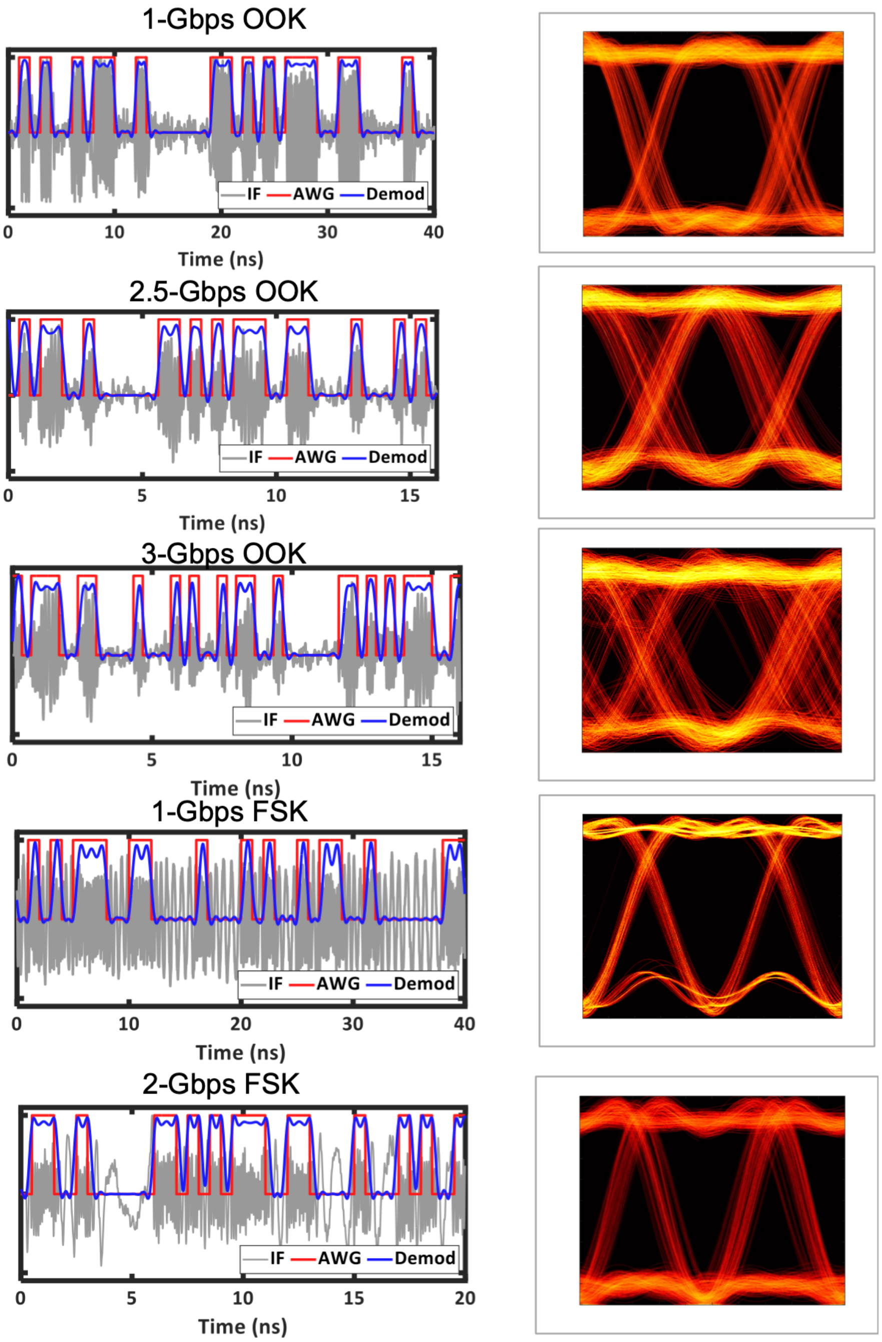

Figure 3.10: Time domain waveforms and eye diagrams for various data rates and modulation schemes over 20-meter distance.

Table 3.2: Comparison with previous THz multi-Gbps transmitters.

Reference	**This work**	**[76]**	**[24]**	**[77]**
Frequency(GHz)	**390**	220	410	196
Distance (meter)	**20**‡	0.28	0.61	0.01
Modulation	**OOK & FSK**	ASK (2-bit array)	OOK	FSK
Data Rate (Gbps)	**3**	20	1 @ 61cm & 5 @ 13cm	10
Pdc(mW)	**70**	165.2	120	231
EIRP(dBm)	**13**	4.2	-3.99	-3
Area (mm^2)	**0.18**	0.89	-	0.68
Technology	**90-nm SiGe BiCMOS**	**55-nm SiGe BiCMOS**	28-nm Bulk CMOS	**55-nm SiGe BiCMOS**

transmitting 2 M bits at a rate of 3 Gbps (BER¡0.5×10^{-6}). Recording more than 2 M bits was not possible due to the limited memory of the test instrument (oscilloscope).

In this section, a 3 Gbps 20 m communication link at 0.4 THz has been demonstrated by using a low-power (70 mW) transmitter. Table 3.2 compares the transmitter of this work with previous state-of-the-art THz transmitters. To the best of my knowledge, this is the longest multi-Gbps THz communication link demonstrated using a low-power fully-electronic silicon-based transmitter.

CHAPTER 4

Demonstration of Novel THz Applications and Measurements

4.1 Plasma Characterization using a Silicon-Based Terahertz Frequency Comb Radiator

4.1.1 Introduction

Due to myriad applications, the Terahertz (THz) band has been of great interest to researchers over recent years. Electronic silicon-based technologies enable the integration of THz radiators and detectors at the system level providing an efficient low-cost solution for high-resolution radars, imaging, remote sensing, and high-speed communication. THz Continuous wave (CW) [29] and pulse based approaches have been improving constantly for different types of applications. In particular, for broadband remote sensing applications and spectroscopy, pulse-based radiators and detectors have been demonstrated to be a more viable solution compared to CW systems due to broadband spectral information, and ultra-low-phase-noise THz tones. In [9, 10], a THz pulse radiator is used to recover and reconstruct the sound from vibrations on the surface of a scattering radar target using micro-Doppler effect. THz waves can also be used to characterize the propagation medium based on its complex permittivity [78]. As a result, THz waves have been considered for plasma characterization. For instance, a THz-TDS system is utilized in [79, 80] to probe and characterize the plasma across a wide band.

Amongst conventional approaches for plasma characterization, interferometry is a well-established non-intrusive method to measure the line integrated density of a plasma [81]. The general concept is to measure the phase shift of an electromagnetic wave in the plasma relative to that in vacuum. For high density plasmas, optical instruments utilizing lasers are used for interferometry [82, 83, 84]; however, this is challenging at low densities where the characteristic plasma frequency is orders of magnitude smaller than the frequency of the laser and capturing the phase shift due to plasma is not feasible. For low density plasmas, microwave radiation is widely used for interferometry[85, 86, 87, 88]. In order to measure a broad range of plasma density ($10^9 - 10^{13} cm^{-3}$) for devices such as the Large Plasma Device[89], the microwave frequency must be sufficiently higher than the plasma frequency so that the beam stays coherent after traveling through a non-uniform plasma volume, but also low enough such that a phase difference is measurable at low density.

THz pulses/frequency comb can be used to probe and characterize plasma physics. Utilizing a broadband frequency comb increases the dynamic range of the measurements and is more suitable for the measurement of different plasma densities. Additionally, by investigating the measurement data in different frequencies, ambiguity in the measurements can be minimized. Moreover, THz frequency comb can be used to detect the rotational states of molecules and identify the gas species present in the chamber. Considering that broadband THz radiators and receivers [12, 18, 90, 91, 92] can be implemented in silicon, they are superior to other types of sources in terms of the cost and integration.

In this work, an experimental setup using a single custom-designed silicon-based THz frequency-comb radiator [17] is presented to probe a pulsed Inductively Coupled Plasma (ICP) at different frequencies in the low-THz band. I/Q analysis have been used to calculate the phase and amplitude change of THz tones. Measurements have been performed under various plasma pulse repetition rates, pressures, and RF excitation powers. Based on the results, plasma characteristics including the electron density and plasma frequency are calculated. The remainder of this section is as follows: section 4.1.2 elaborates on theories of plasma physics and illustrates how a broadband THz frequency-comb radiator can benefit the measurements. In section 4.1.3, the operation of the chip and the main specifications are presented. Section 4.1.4 describes the details on the experimental setup and section 4.1.5 reports on the measurement results. Finally, section 4.1.6 concludes this work.

4.1.2 Theory; Plasma Physics

The main parameter of the relevant unmagnetized plasma physics is the plasma frequency (ω_p). The plasma behaves as an opaque medium below the plasma frequency and a transparent medium above it. Plasma frequency can be calculated as

$$\omega_p = \sqrt{\frac{n_e e^2}{m_e \epsilon_0}} \tag{4.1}$$

where n_e is the electron density, e is the electron charge, and m_e is the electron mass. (4.1) shows that the plasma frequency increases for higher densities, thus necessitating a probing source with higher frequency of radiation. Normally, a microwave source with an order of magnitude higher frequency than the plasma frequency is used. This is done to prevent beam refractions. Therefore for each density, the microwave source frequency range is limited for correct measurements. THz frequency-comb sources have tones over a wide bandwidth (e.g. 50-500GHz), which can be utilized to improve the dynamic range of measurements.

The complex index of refraction $n = \sqrt{\epsilon/\epsilon_0}$ in plasma is frequency dependant and in the absence of magnetic field is given by the equation

$$\frac{\epsilon}{\epsilon_0} = (1 - \frac{\omega_p^2}{\omega^2 + \nu^2}) - i(\frac{\omega_p^2}{\omega^2 + \nu^2}\frac{\nu}{\omega}) \tag{4.2}$$

where ω is the radiation frequency and ν is the average momentum collision rate. Note that the collision frequency in this experiment is more than five orders of magnitude smaller than the microwave frequency, so the imaginary part is negligible.

The amount of the phase shift is

$$\Delta\phi \approx \frac{\omega}{c}\int[(1 - \frac{\omega_p^2}{\omega^2 + \nu^2})^{\frac{1}{2}} - 1]dx \tag{4.3}$$

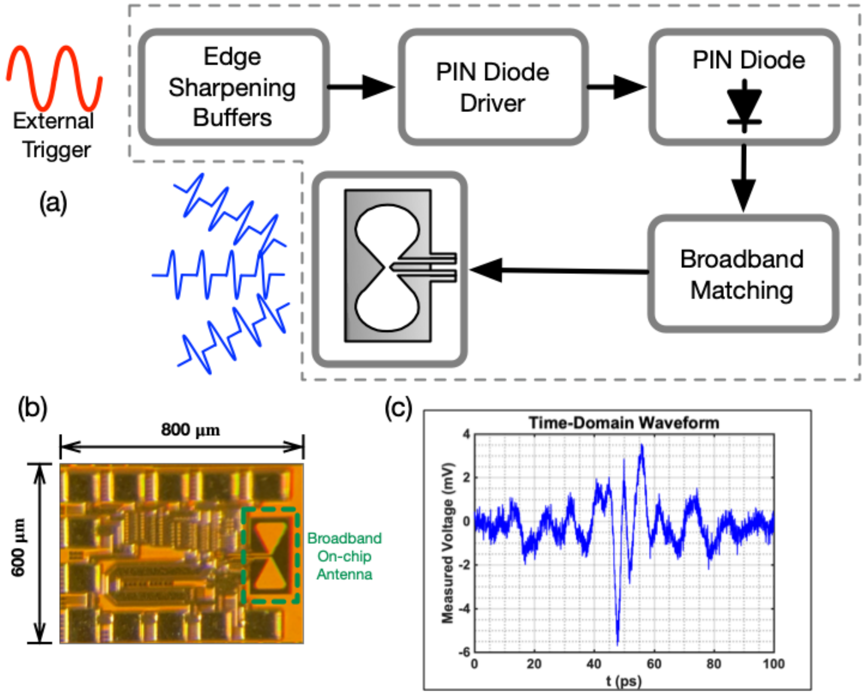

Figure 4.1: (a) Block diagram of the chip operation, (b) Micro-graph of the THz radiator chip. (c) Time-domain waveform of the radiated pulses.

With $\nu << \omega$, the plasma density can be calculated by

$$\Delta\phi \approx \frac{e^2}{2c\omega m\epsilon_0} \int n_e dx \tag{4.4}$$

4.1.3 THz Radiator Chip

A custom designed frequency-comb/pulse radiator in 130-nm SiGe BiCMOS is used as the source [17]. The chip radiates frequency comb from 10s of GHz up to 1.1 THz using a broadband on-chip slot bow-tie antenna. A high-resistivity silicon lens is employed to increase the efficiency and gain of the antenna. The lens prevents the THz power from being trapped in the substrate in the form of substrate wave-guide modes. The spacing between the radiated tones is determined by the pulse repetition rate, which is tunable up to 10.5 GHz. The pulse generation mechanism of this chip is based on the non-linearity of

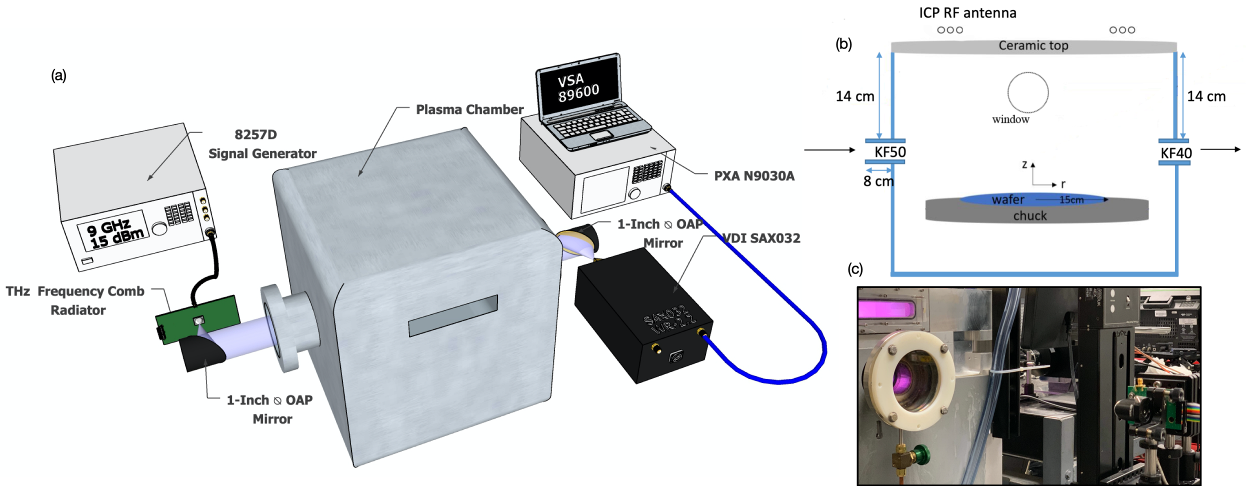

Figure 4.2: (a) A 3D view of the experimental setup used for plasma physics characterization, (b) schematic of the experimental plasma chamber, (c) a picture of the experimental setup.

a PIN diode device in reverse recovery. A block diagram of the chip operation is illustrated in Fig. 4.1(a). The driver stage, which is fed by an external trigger, pushes the PIN diode into reverse recovery mode. Due to the high non-linearity in reverse recovery of a PIN device, ultra-short pulses with picosecond duration can be generated and radiated using an appropriate matching circuit. Note that the generated pulses are locked to a low-phase-noise external trigger signal rather than an on-chip oscillator. Thus, the radiated tones have a low phase noise, which is critical for high-resolution remote-sensing and spectroscopic applications where the modulated THz tones contain the phase information. Fig. 4.3 shows a micro-graph of the chip, and a time-domain waveform of the radiated signal measured by an optical THz-TDS setup. The total power consumption of the chip is 45 mW, and the repetition rate of the pulses is set to 9 GHz in the experimental plasma setup.

4.1.4 Experimental Setup

Fig. 4.2 shows the experimental setup designed for probing an ICP [93]. The plasmas are excited using an RF coil on a ceramic window located on the top of the chamber. In this setup, the plasma is investigated with different pulse repetition rates[94]. To probe

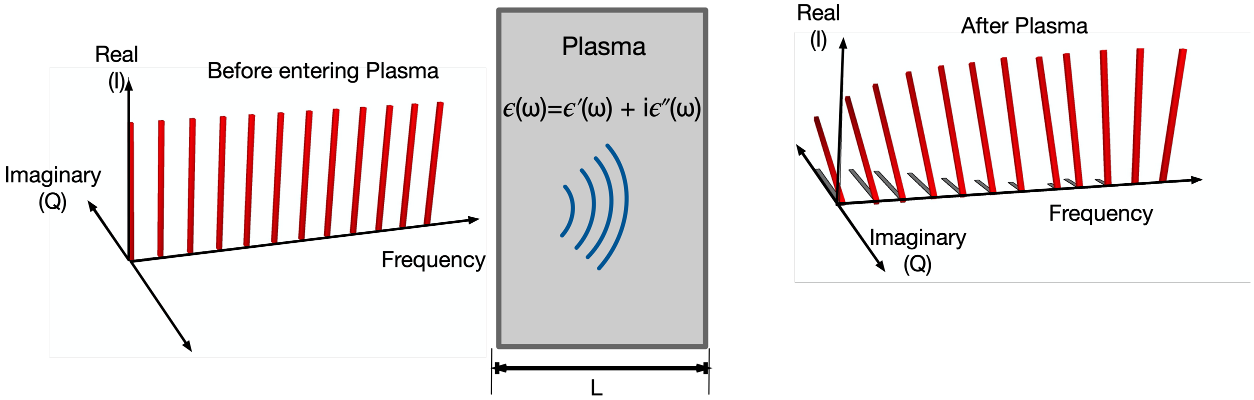

Figure 4.3: Illustration of plasma interaction with the THz frequency comb.

the plasma properties, the custom-designed frequency-comb radiator of section III is used, which is fed with by a 9-GHz signal generated from a Keysight E8257D signal generator. The radiation of THz chip is first collimated using a 1-inch-diameter Off-Axis Parabolic (OAP) mirror at the opening of the chamber. The collimated beams are then focused on the receiver's antenna using another OAP mirror at the other side of the chamber. To minimize the error in the measurement, precise collimation is critical; therefore, collimation is first performed using visible a light laser, and the laser is later replaced with with the chip at the exact same location. THz tones are down-converted into IF frequency using a VDI spectrum analyzer extender (SAX032), which covers 320–500-GHz band. The IF signal is then measured using a PXA N9030A Keysight spectrum analyzer.

In pulse-based ICP, the plasma appears and disappears with the frequency of the pulses. In other words, when the RF generator is energized, the antenna excites the gas in the chamber, thereby generating the plasma. As explained in section II, the plasma causes a phase shift in the probing THz beam (Fig. 4.3). When the RF pulse goes low, the plasma disappears from the chamber. As a result, the THz waves reach the receiver at a phase proportional to their vacuum path length. This means that the phase and amplitude of each THz tone in the frequency comb is being modulated by pulsed plasma. To capture

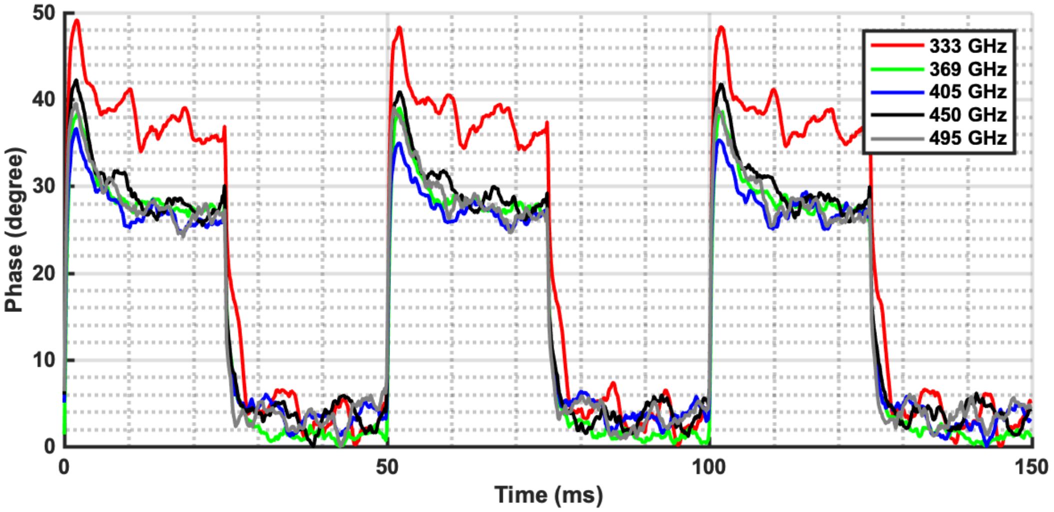

Figure 4.4: Time-domain wave-forms of THz tones' phase.

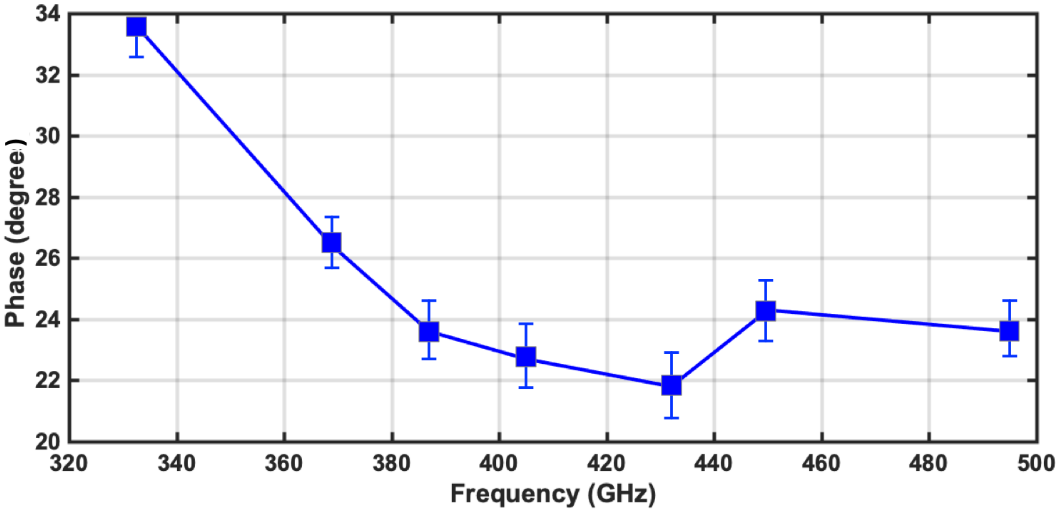

Figure 4.5: Phase shift of THz frequency comb through an Ar ICP.

the IF I/Q data, Keysight Vector Signal Analysis (VSA) 89600 is utilized. Using VSA, quadrature demodulation is performed allowing to calculate the amplitude and phase of the tones separately over time. The precision of I/Q measurement is limited by the power and phase noise of the THz tones.

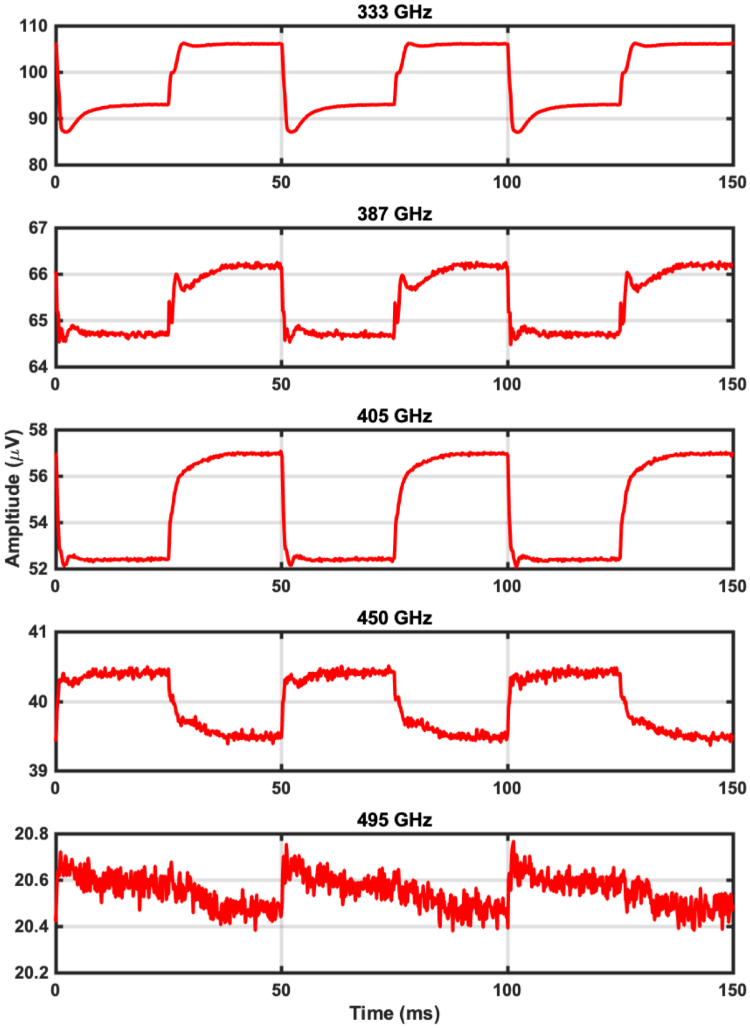

Figure 4.6: Amplitude of the THz tones versus time.

4.1.5 Measurement Results

The results are investigated under different plasma excitation power, pulse rates, and pressures. Fig. 4.4 illustrates the time-domain phase averaged over 100 pulses across the THz band where the plasma is pulsed at 20 Hz with 700 W excitation power. Fig. 4.5 plots the phase change for each frequency point, which is in agreement with (4.4) predicting smaller phase changes at higher frequencies, Fig. 4.6 shows the time-domain amplitude of the THz

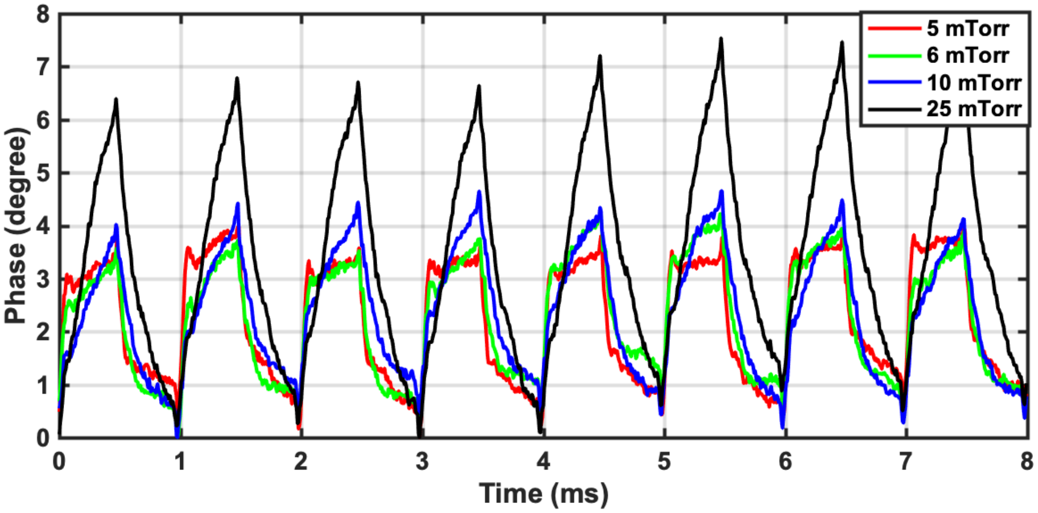

Figure 4.7: Phase change for different gas pressures.

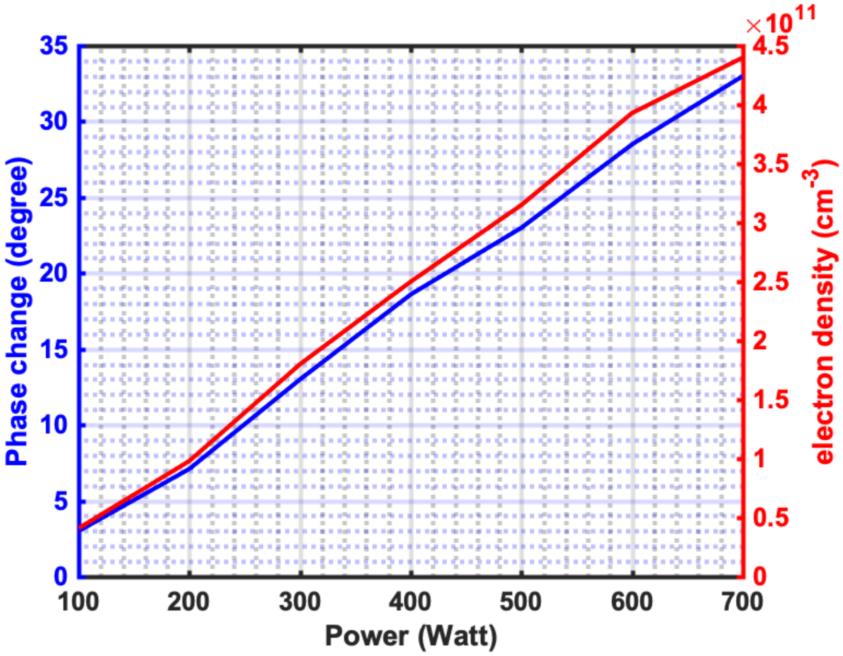

Figure 4.8: Measured Phase shift and calculated electron density versus various excitation power.

tones. Amplitude fluctuations are caused by refraction and absorption in the spatially non-uniform plasma. At higher frequencies (495 GHz) the change in the amplitude is negligible, which is expected according to (4.2). Based on (4.4), ω_p is approximately 6.05 GHz, which corresponds to an electron density of $4.5 \times 10^{11} cm^{-3}$. This measurement was verified with a different 60 GHz homodine interferometer[95] and hairpin probe.

The gas pressure in the chamber affects the plasma density, and consequently the phase shift of the microwaves. In general, plasma in an ICP is generated by electron neutral collisions, so increasing the pressure results in denser plasmas, therefore higher phase shift is expected. Fig. 4.7 shows the measured results for gas pressures of 5, 6, 10, and 25 mTorr at the plasma pulse rate of 1 kHz. At higher pressure, the plasma on-time is not long enough for the density to reach steady state. This is consistent with previous observations [94].

Plasma frequency and the phase change depend on the plasma excitation power. With the increase in the excitation power, the plasma becomes more dense, which results in higher plasma frequency. Thus, for the same probing frequency (333 GHz), higher phase shift is observed at higher power. Fig. 4.8 shows the amount of the phase shift and corresponding electron density when the excitation power is swept.

4.1.6 Conclusion

In this work, a new technique for pulsed plasma characterization using a low-power silicon-based THz frequency-comb radiator is introduced. Using the THz frequency comb, the spectral information of plasma is captured over a wide band. The plasma frequency and electron density are calculated by measuring the phase shift across THz band using a vector signal analysis tool. Since the frequency comb extends from 10 GHz to 500 GHz, the system is capable of measuring a broad range of densities. Low power consumption, high spectral resolution, high integration capability, and broadband radiation makes this silicon-based THz radiator a low-cost solution for plasma sensing applications.

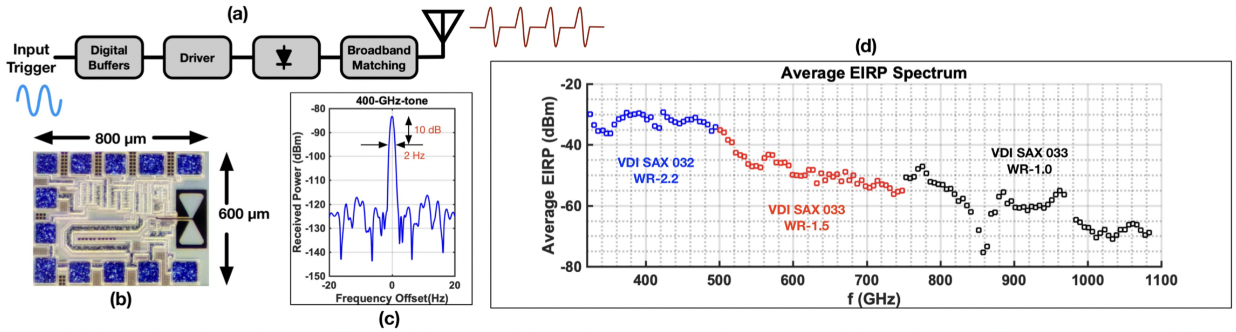

Figure 4.9: (a) Architecture (b) Chip Micrograph (c) Measured THz Linewidth (d) Measured EIRP.

4.2 Terahertz Gas-Phase Spectroscopy of CO using a Silicon-Based Picosecond Impulse Radiator

4.2.1 Introduction

Owing to the unique spectral fingerprints inherent in the terahertz (THz) regime, THz spectroscopy is considered a vital tool for sensing and material characterization. Remarkable improvements in THz integrated circuits in the previous decade have sparked an increasing interest in the development of chip-scale THz spectrometers. A broadband, tunable source having a narrow linewidth is desired for high-resolution spectroscopy. In this work, I have demonstrated THz spectroscopy of CO using a fully-electronic frequency comb radiator designed in a commercial BiCMOS process. CO detection has been crucial for air-pollutant monitoring and fire sensing. Lately, it has also been used to predict aerodynamic heating in hypersonic environments for Mars entry capsules. The quantized rotational transitions exhibit periodicity with absorption lines repeating at an interval of 115 GHz for CO. The custom-designed chip demonstrated in previous chapters was used to perform broadband spectroscopy and measure CO absorption lines at 461, 576, and 691 GHz across different pressures and mixing ratios. A silicon integrated source promises a compact, cost-effective, and energy-efficient solution compared to its counterpart laser-based source.

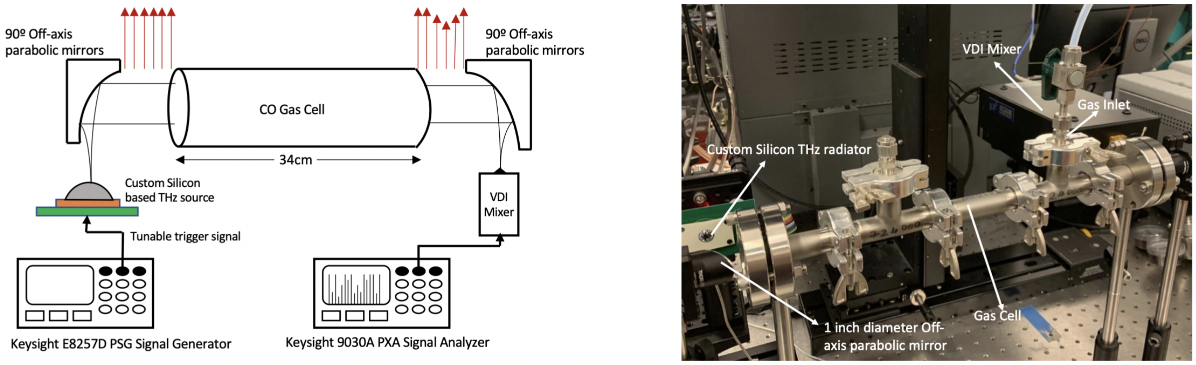

Figure 4.10: CO gas spectroscopy measurement setup.

4.2.2 Custom Impulse Radiating THz Source

A custom silicon chip [17] with an on-chip antenna is used to perform gas spectroscopy. Using direct Digital- to-Impulse(D2I) technique [39], the chip generates and radiates pulses with a FWHM of 1.7 ps, resulting in a broadband 0.3–1.1 THz frequency comb. The spacing between the tones is programmable, set by the frequency of the input trigger. The radiated THz tones exhibit a narrow 10-dB linewidth of less than 2 Hz. This is at least three orders of magnitude lower than the laser sources and enables high-resolution spectroscopy. A hemispherical silicon lens is attached at the backside of the chip to eliminate the substrate modes caused by its rectangular geometry. The architecture of the chip, the measured linewidth of the frequency comb, and the average measured EIRP spectrum is shown in Fig. 4.9.

4.2.3 Experimental Setup

Fig. 4.9 illustrates the measurement setup. The gas cell consists of a 340-mm long aluminum tube with 25-mm inlet windows. The gas cell is sealed using sapphire windows and has a provision of precisely monitoring the pressure and the volume mixing ratio (VMR) of the gas inside the cell. The chip is fed by a digital trigger generated from a Keysight E8257D PSG signal generator. The radiated THz signal passes through a 90° off-axis parabolic mirror

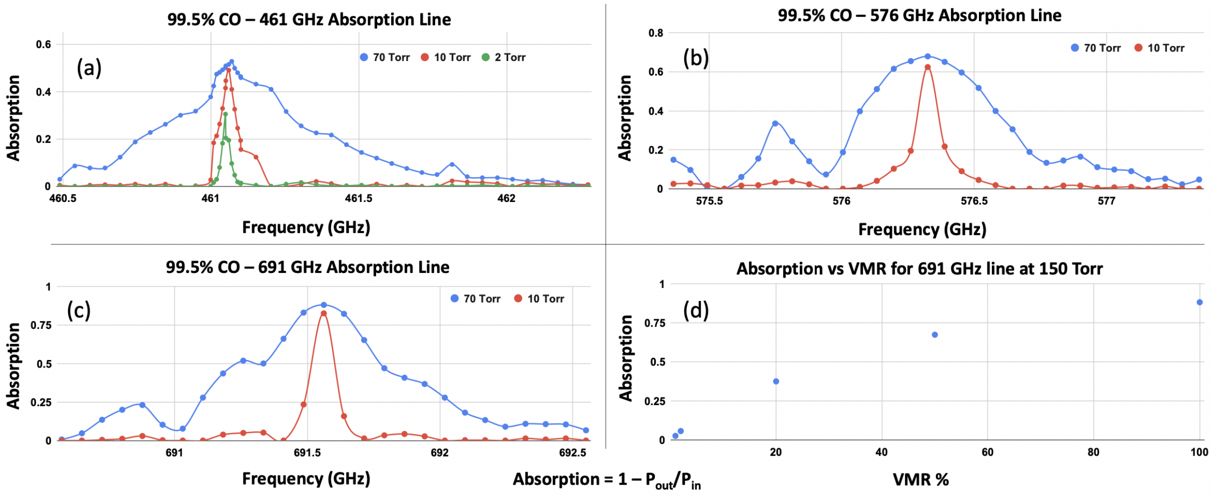

Figure 4.11: (a) 461 GHz Absorption Line (b) 576 GHz Absorption Line (c) 691 GHz Absorption Line (d) Absorption vs VMR at 691 GHz.

of 1 inch diameter having a protected aluminum coating. It collimates the beam to the size of the gas cell window and ensures low-loss transmission. A similar mirror placed at the outlet of the gas-cell focuses the THz pulses to the horn antenna of a Virginia Diodes Inc. (VDI SAX WR-2.2/1.5) harmonic mixer. The power of each tone in the downconverted signal is measured by a Keysight N9030A PXA Signal Analyzer. The digital trigger input frequency is set to 9 GHz and changed in steps of 1 MHz to sweep the frequency around the absorption peaks.

4.2.4 Measurement Results and Discussion

Initially the cell is filled with vacuum and the received power is measured around the three absorption peak frequencies. The cell is then filled with 99.5% CO and the received power is recorded. The absorption values are computed from the difference between the received powers and are plotted in Fig. 4.11. Measurements are performed at 70 Torr and 10 Torr to demonstrate the pressure-broadening effects. In addition, to illustrate the advantage of using a source with a narrow linewidth, absorption is recorded at a low-pressure of 2 Torr at 461 GHz. The VMR of the gas was also varied and the absorption was recorded for mixing ratios as low as 1%. The measured results are in accordance with the HITRAN simulations.

The presented broadband source allows sensing of multiple lines, which helps to reduce the probability of false alarm for gas detection. Its excellent frequency stability enables precise detection in mixtures containing multiple gases that absorb at almost the same frequencies and allows sensing at extremely low pressures. To the best of the my knowledge, this is the first time a silicon-based chip-scale THz spectrometer was used for CO sensing.

4.3 Terahertz Channel Characterization Using a Broadband Frequency Comb Radiator in 130-nm SiGe BiCMOS

4.3.1 Introduction

Most studies in the THz domain have been limited to short-distance setups in a lab environment. Studies of long-distance THz propagation have mostly utilized laser-based THz sources. However, laser-based THz systems suffer from high power consumption, high cost, and bulky measurement setups. Therefore, although such studies have offered valuable analyses of the THz band, they do not promise a practical solution for the long-distance THz propagation problem.

A variety of challenges need to be addressed for long-distance THz propagation. The Friis formula illustrates major constraints in high-frequency wave propagation:

$$P_{r|dB} = P_{t|dB} + G_{t|dB} + G_{r|dB} + 20\log(\frac{\lambda}{4\pi d}) - 4.34\alpha_f d, \tag{4.5}$$

where P_r is the received power and P_t is the transmitted power. G_r and G_t are the antenna gain for the receiver (RX) and transmitter (TX), respectively; α_f is the frequency-dependent atmospheric attenuation factor; λ is the signal wavelength; and d is the distance between the receiver and the transmitter. As is evident, the amount of path loss is directly proportional to the frequency of the propagating wave. As a result, at the THz band, the amount of path loss is significantly larger compared to lower frequency bands, thereby limiting the propagation distance. The other challenge arises from atmospheric absorption lines. A precise knowledge of the locations and widths of these absorption lines is essential for long-distance applications. Spectral shaping techniques can be employed to effectively use the windows in between the absorption peaks to mitigate this problem. These challenges become even more critical in the case of silicon-based THz radiators, in which the radiated power is significantly lower than optical THz generators.

Prior studies of THz wireless channel characterization have been attempted with varying temperatures, humidities, and elevations to refine the existing theoretical models and predict atmospheric propagation in this regime. These studies have used predominantly optical setups implementing Fourier transform spectroscopy (FTS) [96, 97, 98, 99] or THz time domain spectroscopy (THz-TDS). For instance, in [96], multipass FTS was used to propagate THz radiation between 0.15 and 1.1 THz over distances up to 469 m. In [99], a THz-TDS system with optoelectronic antennas was used to characterize water-vapor absorption from 0.2 to 2 THz over a distance of 6.2 m. All these techniques suffer from the aforementioned limitations imposed by the use of an optical-laser-based setup.

Due to the limited bandwidth and radiated power of conventional electronic THz sources, and due to high absorption in the THz band, low-cost electronic sources were not considered as a viable option for relatively large distances. However, it was shown in [100] that transmitting and receiving broadband THz pulses over 100s of meter is feasible. This section is based on [101, 100]. This work describes an all-electronic method that uses a low-power silicon integrated radiator based on PIN diode reverse recovery [17] to examine the channel response in the 0.32–1.1 THz frequency range for distances between 10 and 110 m. Note that the THz radiator chip used in this work is the same as the radiator chip used in sections 4.1, 4.2. Compared to [100], a more efficient THz pulse radiator is utilized which results in higher received power, and more details of the measurement approach and theoretical analysis are presented. The goals of this are are (1) to demonstrate wireless transmission and reception in THz frequencies over long distances using a low-power custom silicon-based radiator, (2) to identify the frequency windows suitable for THz propagation, and (3) to demonstrate channel characteristics (e.g., atmospheric absorption coefficient) over a broad range of frequencies using a compact, all-electronic, tunable silicon source. The experimental setup of this work can also be used to investigate long-distance high-speed wireless communication, remote sensing, and radar applications.

In section 4.3.2, the long-path experimental setup, which is used for channel characterization, is elaborated. Section 4.3.3 presents the measurement results. Section 4.3.4 offers insights into the measurement results and proposes a method of extracting the absorption coefficient from the measured data, and section 4.3.5 concludes this work.

4.3.2 Long-Distance Experimental Setup

It is well-known that THz atmospheric transmission is a function of relative humidity [102]. The channel characterization measurements were performed indoors with an average humidity of 55%. The schematic of the measurement setup for distances between 10 and 110 m is shown in Fig. 4.12, in which the chip is fed by an 8-GHz trigger signal from a Keysight E8257D PSG Signal Generator. Two off-axis parabolic (OAP) mirrors were utilized to increase the directivity of TX and RX antennas for long-distance propagation. The parabolic mirrors are utilized as directive reflector antennas for THz waves enabling long-distance propagation. The directivity of the OAP mirror is determined by the size of the mirror, Therefore, 4-inch OAP mirrors with aluminium coating were used to collimate the beams. Furthermore, the metal thickness of the mirror coating was larger than the skin depth at THz frequencies, promising low-loss reflection.

Following M1, the collimated THz electromagnetic waves pass through various distances between 5 and 55 m to reach a plane mirror (M2). The reflected waves from M2 pass through the return path to reach another 4-inch OAP reflector (M3). A Keysight N9030A

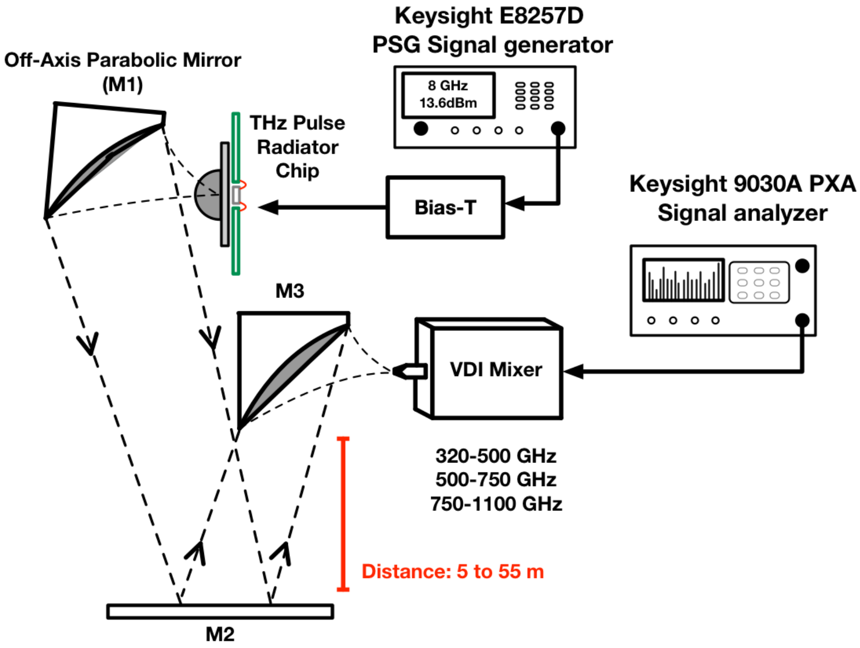

Figure 4.12: A block diagram of the long-distance THz pulse measurement setup.

PXA Signal Analyzer and VDI SAX mixers are used in conjunction with WR2.2, WR1.5, and WR1.0 horn antennas to cover the 320–500, 500–750, and 750–1100-GHz frequency bands, respectively. Moreover, by using a broadband pulse radiator and by changing the position of M2, the channel characteristics were evaluated for different frequencies as well as different distances. Fig. 4.13 illustrates the measurement setup used in this study.

One of the main challenges is the precise collimation of the invisible THz waves. For this purpose, the THz pulse radiator chip is replaced with a lens that transforms the red laser beam (located at back of the printed circuit board) into a point source. After collimating the visible light by adjusting the mirrors, the quality of collimation is checked at a distance of 55 m from the setup. To facilitate the measurements at different distances without needing to adjust the mirrors, another visible light laser (the green-light laser shown in Fig. 4.13) is used to track the propagation path of the collimated THz waves.

Collimation, although performed in visible light region, can fail in the THz band due to nonideal effects of the antennas at the receiver and transmitter sides. One of the main

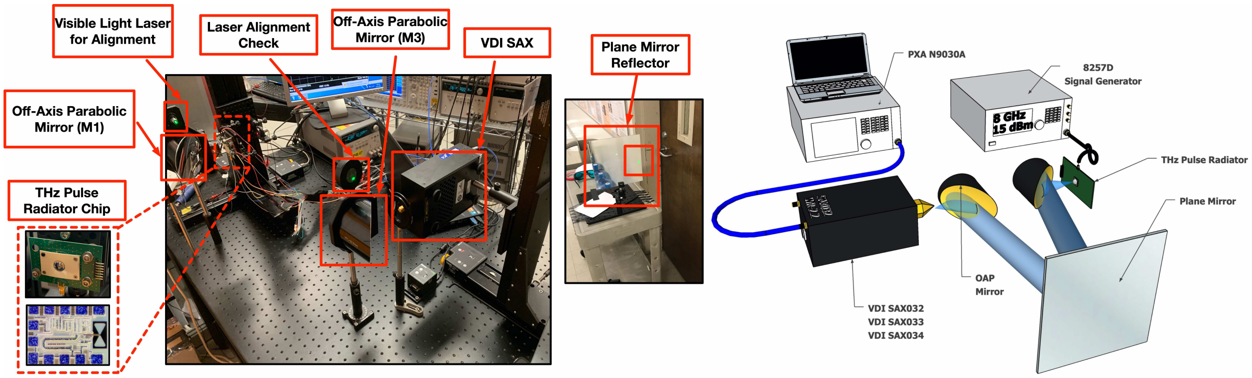

Figure 4.13: A picture of the long-distance THz pulse measurement setup with details of the components and equipment used.

challenges over the band of radiation is the varying phase center of the antennas. Therefore, it is critical to take such an effect into account during the measurement. In order to have a realistic expectation of the phase center deviation, electromagnetic simulation is performed in CST Studio Suite that illustrates the change in the phase center. Fig. 4.14 (a) shows the fluctuations of the phase center for the radiator's antenna. As observed, the phase center changes abruptly across the band, which is due the complex structure of the the transmitter's antenna, which consists of a high resistivity silicon lens, doped silicon layer, silicon oxide, and a slot bow-tie (Fig. 4.14(c)). In order to compensate the phase center fluctuations and maintain collimation, for each frequency point, the position of the chip is adjusted to find the position with the highest received power. The same method is applied at the receiver side. Phase center variations of diagonal horn antennas at the receiver side are calculated based on [103, 104] for each THz frequency band, which is shown in Fig. 4.14 (b).

4.3.3 Measurement Results

Fig. 4.15 shows the power of the received signal over the frequency range of 0.32–1.05 THz and the channel length of 10 to 110 m. The frequency step of the measurement is 8 GHz, which equals the repetition rate of the external trigger applied to the THz radiator. Note

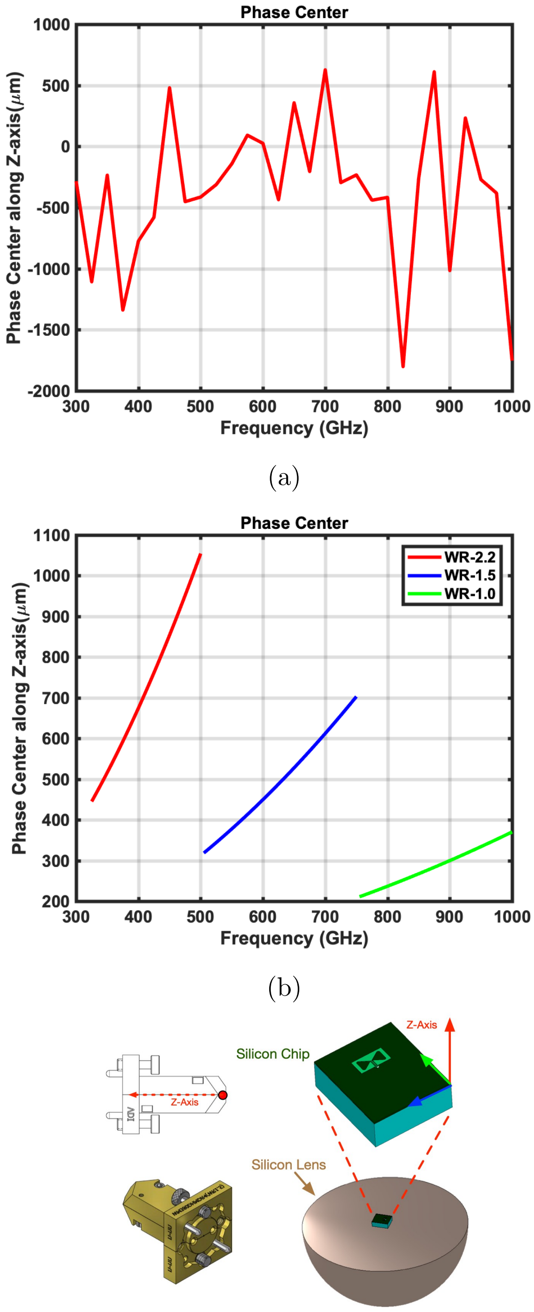

(a)

(b)

(c)

Figure 4.14: Variation of antennas' phase center across THz band for (a) THz transmitter and (b) VDI receiver. (c) Structure of the transmitter and receiver antennas.

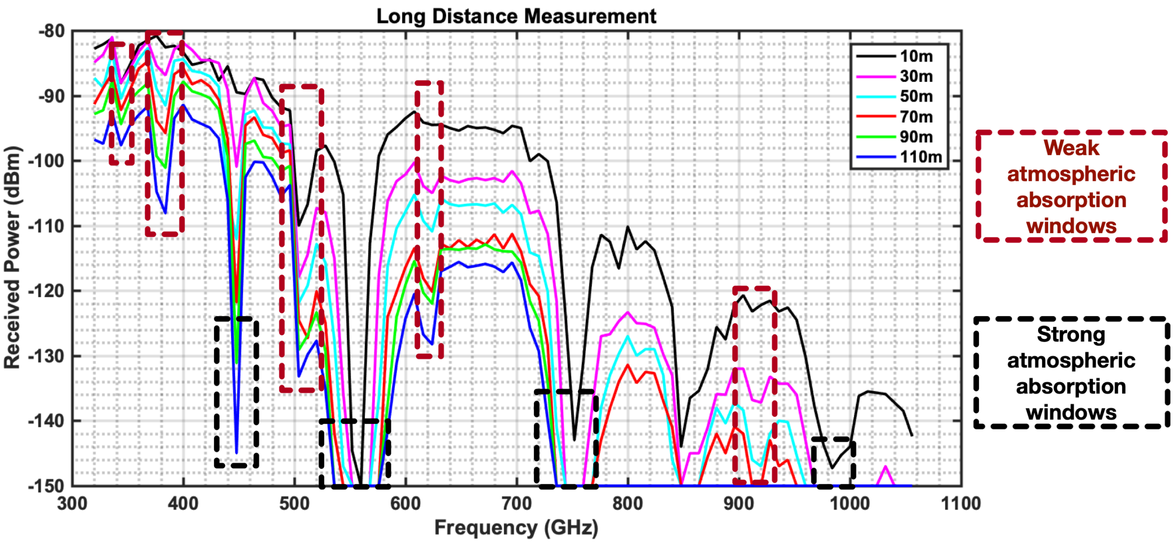

Figure 4.15: Measured received power across the THz band for different propagation distances.

that by varying the repetition rate, the frequency steps can be changed to any arbitrary number, thus enabling us to cover the desired frequency band with a resolution determined by the linewidth of THz tones. The 10-dB linewidth of the THz tones is less than 2 Hz, which is achieved by locking the repetition rate of the pulses to a low-phase-noise external source. The measured noise floor of the setup is -150 dBm for 1-Hz resolution bandwidth (RBW), which imposes the upper limit on the wireless link range.

As known from equation (4.5), the attenuation of the THz waves can be attributed to two main factors: path loss and absorption. The former directly depends on the propagation distance and the frequency of the propagating wave, which is verified by the results presented in Fig. 4.15. The frequency-dependant absorption stems from the quantized molecular rotational transitions of molecules occurring in the THz regime. Fig. 4.15 illustrates the weak and strong absorption windows due to the presence of water molecules in the atmosphere. These windows are divided into weak and strong windows based on the absorption coefficient. For windows with attenuation above 0.5 dB/m, it is referred to as strong absorption window,

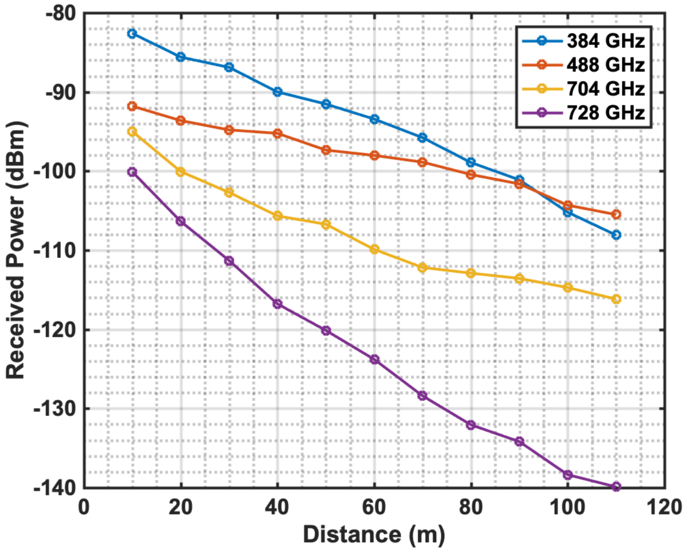

Figure 4.16: Measured received power versus propagation distance.

whereas attenuation of 0.1–0.5 dB/m is labeled as weak absorption window. The locations of the absorption windows have a strong resemblance with those of the HITRAN database [105]. The results of Fig. 4.15 can be used to determine the low-loss frequency windows for long-distance broadband communication, remote sensing, and radar applications.

Fig. 4.16 plots the received power in logarithmic scale versus distance for various frequencies. This figure illustrates the effect of atmospheric absorption on the received power at different frequencies. When fitted to a straight line, different tones have different slopes because of frequency-dependent atmospheric attenuation coefficients. The rate at which the received power declines with distance depends on the absorption as well as path loss caused by imperfect collimation. For instance, at 488-GHz, the slope at which the power drops is less compared to 728-GHz tone, due to different amounts of atmospheric absorption.

The measured weak and strong absorption windows are summarized in Table 4.1. The results are consistent with the HITRAN simulations.

Table 4.1: Absorption windows

Weak Absorption Windows	**Strong Absorption Windows**
0.33–0.34 THz	0.44–0.46 THz
0.375–0.39 THz	0.53–0.58 THz
0.48–0.49 THz	0.74–0.77 THz
0.615–0.63 THz	0.96–1 THz
0.91–0.925 THz	–

4.3.4 Estimation of Absorption Coefficient

In this section, the absorption coefficient is estimated from the received power at a particular frequency. By measuring the received power across different channel lengths, the frequency-dependent atmospheric absorption coefficient α_f is calculated. The received power over different distances can be compared to obtain an estimate of the absorption coefficient at a particular frequency. From equation (1), over two distances d_1 and d_2, the ratio of the received power can be expressed as

$$\alpha_f = 0.2303 \frac{P(d_1)_{r|dB} - P(d_2)_{r|dB} - 20\log(\frac{d_2}{d_1})}{d_2 - d_1}. \tag{4.6}$$

By using (4.6), the atmospheric absorption coefficient can be calculated for a particular frequency in far-field mode. The upper bound of the extracted absorption coefficient is limited by the noise floor of the setup.

The above analysis is valid only in the far-field region, where the THz beams diverge based on Friis theory. In this setup, OAP mirrors are used to collimate the radiated THz beam from the chip. In the case of perfect collimation, the waves are nondivergent; therefore, the attenuation is due simply to absorption rather than path loss factor. However, due to self-diffraction effects, the collimation is never perfect, and the transmitted THz waves acquire a curvature as they propagate along the channel. This effect of divergence is quantified in terms of the Rayleigh range, which is defined as the distance at which the beam width increases by a factor of $\sqrt{2}$. In other words, the effective spot size of the collimated THz beam doubles at this distance. In this study, a 4-inch OAP mirror has been used to collimate the THz waves. The Rayleigh range can be calculated as

$$Z_r = \frac{\pi W_c^2}{\lambda}, \tag{4.7}$$

where W_c is the radius of the OAP reflector antenna, which is 2 inches in the measurement setup (half of the OAP mirror's diameter), and λ is the wavelength. The Rayleigh range for a 4-inch mirror is 8.1 and 27 m at 300 GHz and 1 THz respectively, where the far-field distance is 20.6 and 68.8 m at 300 GHz and 1 THz, respectively. In order to calculate the absorption coefficient at each distance, it is critical to identify the region in which the THz waves are propagating. The on-chip antenna is shown in Fig. 4.17(a), and the EM simulation is performed using CST Microwave Studio. The far-field pattern is illustrated in Fig. 4.17(a) at 300, 500, 700, and 1000 GHz. Fig. 4.17(b) is a symbolic representation of different THz propagation regions. To verify and demonstrate these regions, we use the far-field data of the chip at 300 GHz and the model of a 2-inch OAP mirror for EM simulations. Note that the diameter of the OAP in this simulation is half of the one we used in our measurement to increase the simulation speed. As a result, the Rayleigh range in this simulation is one-quarter of the Rayleigh range in our measurement setup. As shown in Fig. 4.17(c), results of EM simulation clearly illustrates the divergence of THz waves in 2-m length, which is close to the Rayleigh range of the OAP mirror with 2-inch diameter at 300 GHz.

In the receiving side, by using an OAP with the same dimensions placed at Z_r, half of the transmitted power is lost due to diffraction. Equation (5) also shows that with an increase in the frequency of the radiated signal, the Rayleigh range increases. Therefore, the waves can remain collimated for longer distances at higher frequencies. Depending on the frequency of the radiated signal, the resulting beam width can be expressed in terms of distance from the source as

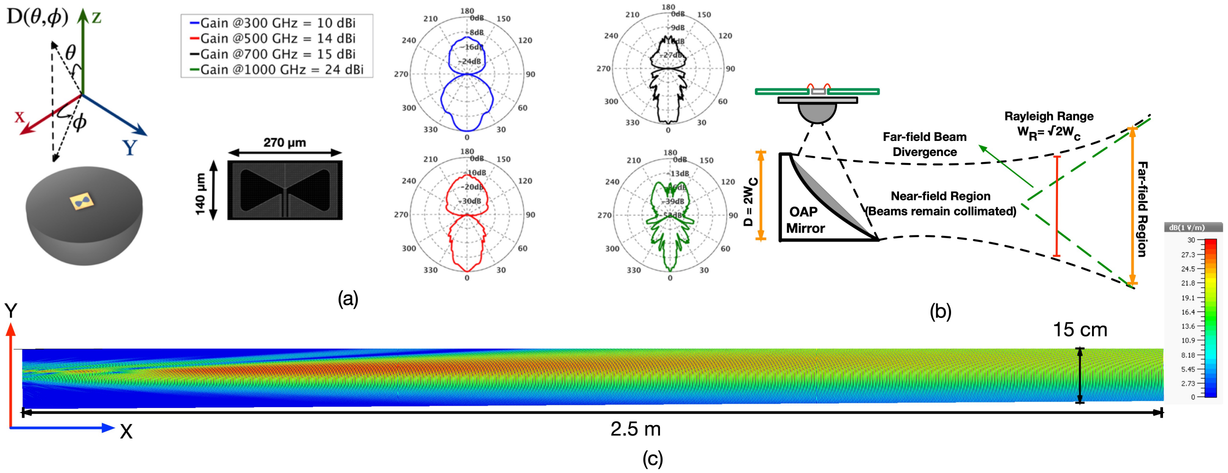

Figure 4.17: (a) Broadband slot bow-tie antenna and its radiation pattern across THz band. (b) Illustration of different propagation regions when an OAP mirror is used. (c) Simulated E-field in Y direction that shows the different propagation regions.

$$W(d) = W_c \sqrt{1 + (\frac{d}{Z_r})^2}, \tag{4.8}$$

where W is the effective beam radius after propagating a distance d from the source. As a result, the ratio of the received power at two distances d_1 and d_2 can be represented as

$$\frac{P_r(d_1)}{P_r(d_2)} = K e^{\alpha_f (d_2 - d_1)}, \tag{4.9}$$

where K is a factor that estimates for the power loss due to divergence of THz beams (or spot size change) and can be expressed as

$$K = \frac{1 + (\frac{d_2}{Z_r})^2}{1 + (\frac{d_1}{Z_r})^2}. \tag{4.10}$$

K is a function of the frequency of the radiated signal and the distances taken into consideration. In the near-filed region, the absorption coefficient can be approximated as

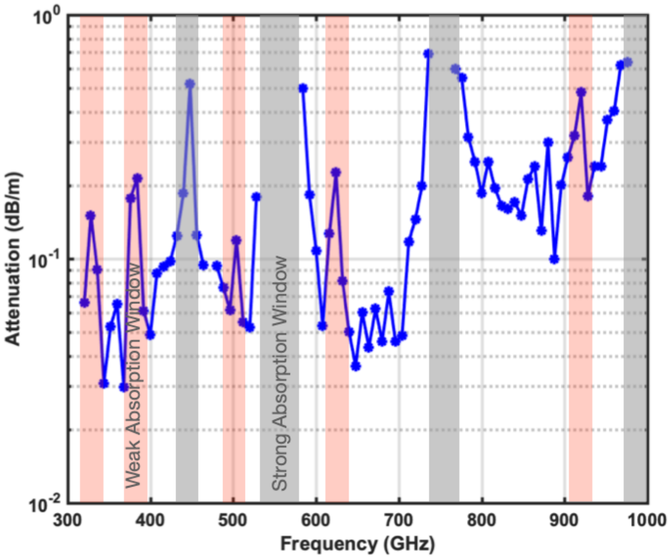

Figure 4.18: Calculated attenuation based on measurement results.

$$\alpha_f = 0.2303 \frac{P(d1)_{r|dB} - P(d2)_{r|dB} - 10\log(K)}{d_2 - d_1}. \tag{4.11}$$

Fig. 4.18 plots the atmospheric absorption coefficient for frequencies in the range of 0.3–0.9 THz using (4.10) and (4.11). Note that to calculate the absorption coefficient, the points below the Rayleigh range for each frequency was used. Therefore, equation (4.11), was used for calculations in near filed region; however, there are still minor errors in calculation of K since the radiated THz waves are not ideal Gaussian beams.

The lower limit of the atmospheric absorption coefficient is set by the amplitude stability of the source, and the upper limit is set by the noise floor of the setup. The relative strengths and the positions of the absorption coefficient peaks are consistent with the HITRAN simulations [105].

Table 4.2: Comparison with previous studies

	This work [101]	[106]	[107]	[108]	[109]
Maximum distance (m)	**110**	167	910	100	0.67
Frequency range (THz)	**0.32–1.1**	0.1–1	0.1–1	0.1–0.4	0.1–2
Frequency steps (GHz)	**8**†	0.0898	0.0084	100	2–3
Source output power (dBm)	**19.2 (EIRP)**	-45.3	-45.3	10*	-
THz source	**Custom-designed 130-nm SiGe BiCMOS chip**	Femtosecond laser (THz-TDS)	Femtosecond laser (THz-TDS)	Virginia Diodes Multiplier	Picometrix T-Ray 4000 (THz-TDS)

*10 dBm @ 400 GHz, 8.5 dBm @ 300 GHz, 20 dBm at 200 GHz, and 24 dBm @ 100 GHz.

†Tunable from 10s of MHz up to 8 GHz with the resolution of 2 Hz, which is limited by the phase noise.

4.3.5 Conclusion

In this study, the results of indoor THz wireless channel characterization are presented using a low-power, custom-designed impulse radiator chip. A broadband radiator eliminates the need for multiple radiating sources to cover a broad range of frequencies. A THz non-line-of-sight link is designed that can be used for communication and broadband sensing applications. In addition, the use of a silicon process to design the radiator enables integration an array of radiators on a single die, which is a practical solution for increasing the propagation range.

Using a custom measurement setup, channel characterization is performed for frequencies in the range of 0.3–1 THz for a distance of 10–to–110 m in steps of 10 m. A comparison of this study with other atmospheric channel characterization attempts is presented in Table 4.2. Due to the utilization of a custom silicon-based broadband THz pulse radiator, this study benefits from low cost and high integration compared to previous ones. Frequency windows with strong water-vapor absorption as well as those with low-loss suitable for wireless propagation in a low-THz regime were identified from the measurement results. Moreover, the results demonstrate the feasibility of using low-power THz silicon radiators for applications such as high-speed communications, high-resolution remote sensing, and radars. To the best of the authors' knowledge, this is the first time THz propagation up to a distance of 110 m using a low-power silicon-based radiator has been demonstrated that has covered the 320–1000-GHz frequency range.

4.4 Micro-Doppler Detection and Sound Sensing using Silicon-based THz Radiators

4.4.1 Introduction

Doppler effect has been broadly utilized to identify, classify, and characterize moving targets such as cars, vessels, and aircraft in radar applications. Similarly, subtle surface vibrations can cause Doppler effect on microscale and generate unique Doppler signatures, which is commonly referred to as micro-Doppler signatures. In vibration sensing applications, by analyzing these signatures, detailed information of the object features, including material properties, texture, surface displacement and vibration frequencies are obtained. Vibration sensing has been used for various industrial applications for quality control and to investigate and characterize the properties of parts under different operating conditions. Vibration sensing has been an integral part of production control in different sectors of industry, including aerospace, automotive, semiconductor, material research, and testing. In [110], micro-Doppler signature of the blades of a wind turbine is used to characterize its performance. In addition, recently, micro-Doppler effect has been found useful in biomedical applications. In [111, 112], micro-Doppler signature of the heart beat is investigated using an Ultra-Wide band (UWB) Doppler radar. In [113], using Laser Doppler vibration sensing (LDV) new biomedical imaging applications are proposed by measuring the surface vibrations of tissues and organs.

Vibration sensing is performed in two forms: contact and non-contact based. Although contact-based vibration sensors such as piezoelectric sensors [114] enable high resolution measurements, it may affect the vibrations by loading the surface, thereby changing the micro-Doppler signature. This is especially the case for weak vibrations of thin surfaces, where the surface displacement can be as low as a few μm. The non-contact based approach, on the other hand, enables capturing the vibration data while preserving the original signature. Moreover, non-contact vibration sensing allows recording the vibration signatures of distant targets, and does not require a short distance between the vibration sensor and the target of interest. Laser based interferometry in visible light and infrared bands has been used for non-contact based vibration sensing to detect displacements in sub-nm range [115, 116]. Laser-based interferometry for vibration sensing allows high precision measurements and eliminates the effect of laser phase noise as long as the phase noise of the beams in two different paths remains correlated. Apart from high cost of such systems, their high sensitivity limits their practicality for some applications, as they are prone to the error caused by environmental factors [117].

Similarly, mm-wave and THz bands can be used to capture a micro-Doppler signature. Although THz/mm-wave vibration sensing offers less resolution compared to optical-based techniques, it is superior in terms of implementation cost and electronic integration. In addition, THz/mm-wave waves can penetrate through a wide range of materials such as cloth, wood, and plastic, thus allowing to capture the vibration signature of the objects behind an optically opaque barrier. [118] shows THz vibration sensing using a phase-noise-compensated laser-based heterodyne system. Although, [118] shows the potential of THz band for vibration sensing applications, is not a practical solution as optical THz systems are bulky and expensive. On the other hand, electronic silicon-based systems benefit from the high level of integration and low-cost implementation [54]. In particular, recent advances in electronic THz transmitter and receiver open a new frontier for myriad applications including vibration sensing. For instance, a 160-GHz radar is used in [119] to recover speech by capturing the signature of the throat's vibrations. Since the Doppler effect intensifies with the increase in the frequency of carrier tone, sub-THz band has been of interest for high-resolution vibration sensing and micro-Doppler recording [9, 10]. FMCW radars have been utilized for vibration sensing as well. However, the main challenge in such systems is phase ambiguity, which results in large measurement errors. Yet, this problem can be mitigated by employing new processing techniques as suggested in [120] for the case of a 77 GHz FMCW radar. It is worth mentioning that the implementation of FMCW radars in THz frequency range is very challenging, due to the high conversion loss of the THz receiver and low efficiency of THz transmitters. In [121], an FMCW radar is demonstrated that covers from 220 up to 330 GHz. Still, such systems have limited resolution and cannot be used for sub-μm vibration sensing. Besides, due to the high propagation loss of THz waves, THz FMCW radars suffer from low SNR limiting their practicality for high-resolution sensing. CW and interferometry radars have been a viable choice for vibration sensing applications [122]. In these systems, the received signal is mixed with the transmitter signal resulting in a zero or low IF baseband signal. There are different drawbacks to CW radars. CW radars, unlike FMCW radars, cannot detect vibrations of multiple targets. Moreover, zero/low-IF receivers of CW radars suffer from high flicker noise, limiting the sensitivity of the receiver. Although the large gain of an LNA can mitigate the limitation of baseband noise at the receiver, it is not a practical approach for THz radars, as THz receivers utilize mixer-first architectures.

In this work, first, a custom-designed THz pulse radiator [12] locked to an off-chip low-phase noise source is used to radiate a frequency comb to record the micro-Doppler signature of a vibrating rigid plane mirror by performing I/Q analysis. In this approach, similar to Doppler and motion sensor radars, the phase of the reflected signal is extracted by quadrature down-conversion. The resolution of the phase is limited by the phase noise of both transmitter and receiver. Locking the receiver and transmitter to the same reference can alleviate this problem, which is addressed in section 4.4.5. Second, a free-running CW THz radiator chip is used to perform THz interferometry to detect subtle sound vibrations. Interferometry offers higher resolution compared to the former technique; however, it requires a high power THz radiator and the measurement setup is more complex. One of the main benefits of interferometry is that it does not require coherence or locking between the receiver and transmitter. This is vital in THz regime, as the implementation of Phase Locked Loops (PLL) can be challenging. Note that the employed approaches of this work are not limited to vibration sensing applications and they can also be utilized for different applications, including high-resolution imaging, spectroscopy, and dielectric properties measurements [11, 88, 123, 124, 125]. This work, which expands on [9, 10], demonstrates multiple low-cost high-resolution approaches for vibration sensing using custom design THz radiator chips, including THz interferometry using a custom designed integrated CW THz radiator. The remainder of this paper is as follows: section 4.4.2 gives a theoretical analysis on the micro-Doppler effect, vibration sensing, and interferometry. Section 4.4.3 elaborates on the operation of THz radiator chips used in this work. The experimental setup and the measurement results based on I/Q analysis are discussed in Section 4.4.4. A phase noise cancellation technique is proposed in section 4.4.5. Interferometry measurement setup using a free-running CW THz radiator chip and corresponding results are provided in 4.4.6. Ultimately, a conclusion on this work is given in 4.4.7.

4.4.2 Theoretical Analysis

4.4.2.1 Micro-Doppler Effect and Vibration Sensing

Doppler phenomenon is the frequency shift caused by relative movement of the target to the receiver. A higher frequency shift is expected as the frequency of the source (incident beam) increases. Fig. 4.19 illustrates the Doppler effect for the case of a vibrating target which is known as micro-Doppler. The reflected beams experience a periodic phase change,

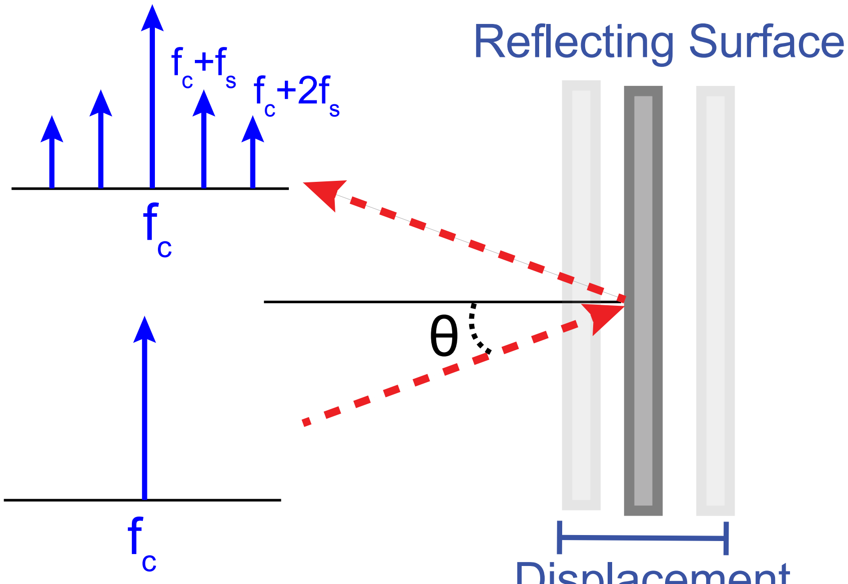

Figure 4.19: Modulation of a carrier tone after reflection from a vibrating surface.

which can be expressed as:

$$R(t) = A\cos\left(2\pi f_c t + 2\pi \int f_d(t)dt\right) \tag{4.12}$$

and

$$f_d(t) = \frac{2v(t)\cos(\theta)}{c} f_c \tag{4.13}$$

$$v(t) = D\omega_s \cos(\omega_s t) \tag{4.14}$$

where D is the amplitude of the vibration (displacement), and θ is the angle between the vibration direction and the incident wave. The signature of vibration manifests itself in the form of phase variation. Therefore, phase demodulation can be used to extract the information of vibrations. Note that D needs to be comparable to the wavelength of carrier for proper phase detection.

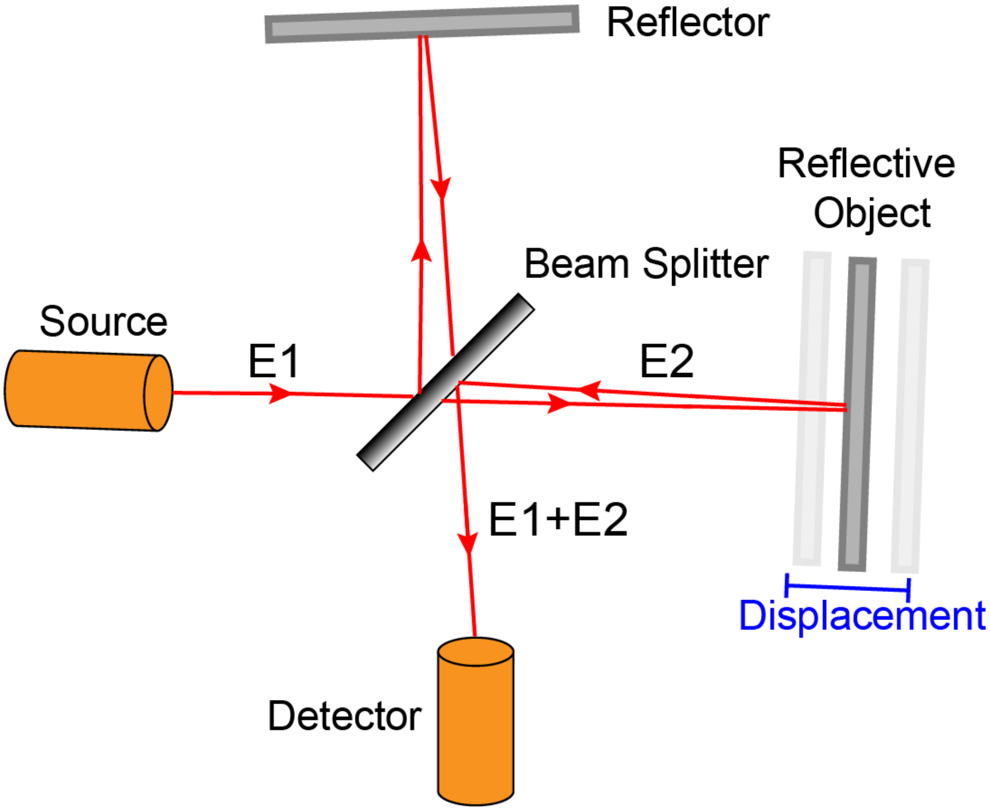

Figure 4.20: Illustration of interferometry method.

4.4.2.2 Interferometry for Vibration Sensing

As shown in Fig. 4.20, in the interferometry technique, a beam is split and travels through two different paths, where the beam in one path experience modulation by the target of interest, and in the other path, the traveling beam remains intact. These two beams are combined at the detector. For the case of vibration sensing, the beam, in one path, experiences phase modulation due to target displacement. After combining the beams, the phase information is transformed into amplitude modulation, thereby enabling a detector to capture this information by measuring the wave intensity. To elaborate on how this transformation occurs, two coherent beams are considered:

$$E_1(t) = A_1 \cos\left(2\pi f_c t + \phi_d(t) + \phi_n\right) \tag{4.15}$$

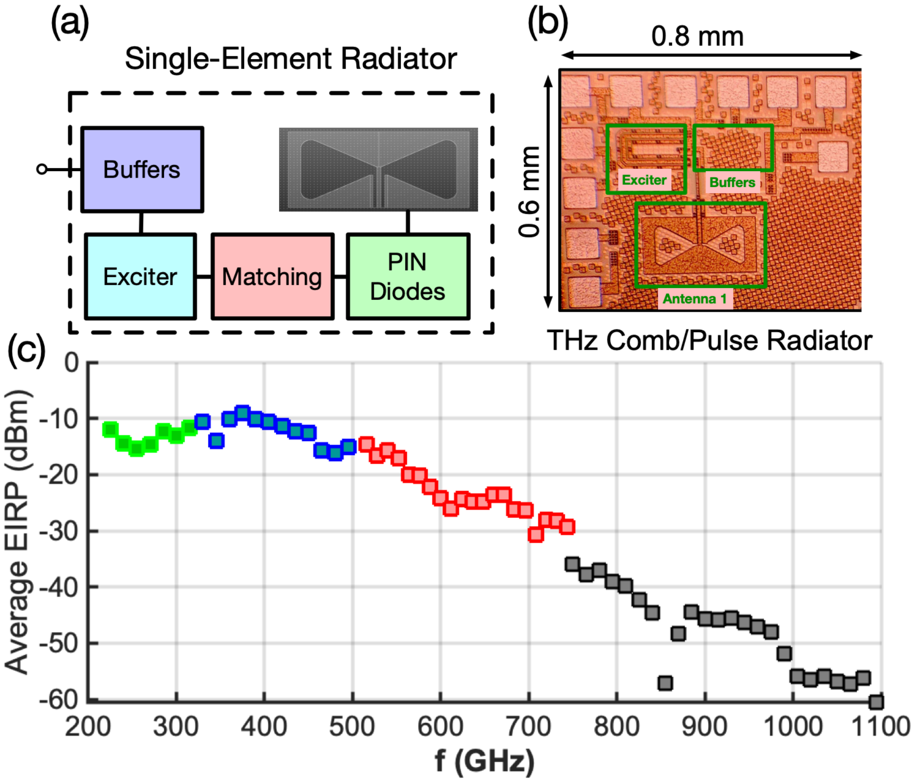

Figure 4.21: (a) Block diagram of the chip operation. (b) A micrograph of the pulse radiator chip. (c) EIRP of the radiator across THz band.

$$E_2(t) = A_2 \cos\left(2\pi f_c t + \phi_n\right) \tag{4.16}$$

Where ϕ_n is phase noise, and ϕ_d is phase change caused by target displacement. The intensity of the combined beams can be calculated:

$$P_{E_1+E_2} \propto \frac{A_1^2}{2} + \frac{A_2^2}{2} + A_1 A_2 cos(\phi_d(t)) \tag{4.17}$$

where the first two terms are constant and the third term contains the phase information of the vibrating sample. Note that the factor of phase noise is eliminated in the aforementioned calculated power. Therefore, the precision achieved in interferometry generally is not limited by the phase noise. This is only true if the phase noise of E_1 and E_2 remain

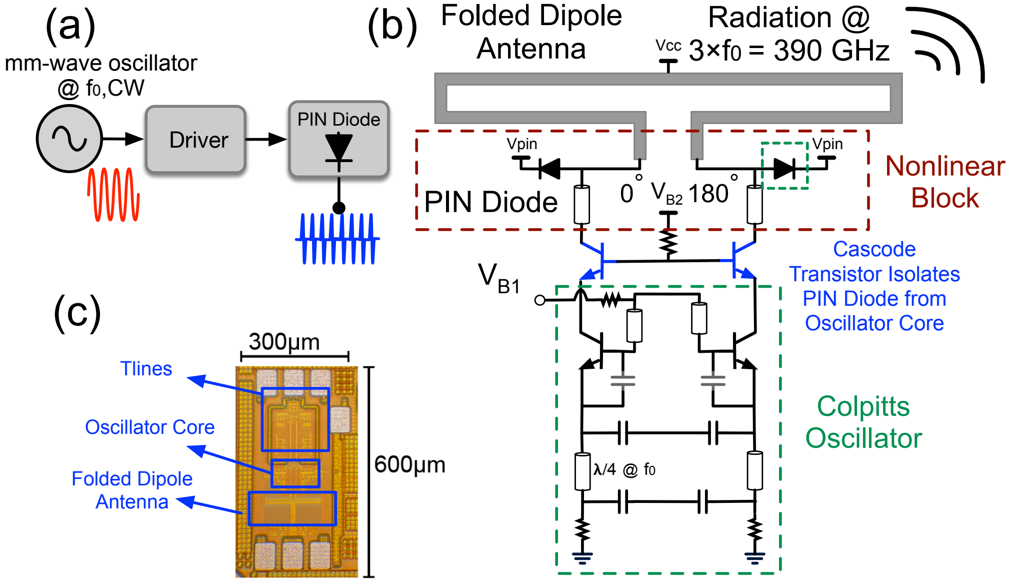

Figure 4.22: (a) Operation of the CW THz radiator chip. (b) Schematic of the CW THz radiator chip. (c) Micrograph of the chip.

correlated, which occurs when the path difference for these two beams is small.

4.4.3 THz Radiator Chips for Vibration Sensing

4.4.3.1 THz pulse radiator

For remote sensing applications, having a stable broadband THz source is critical. With the recent advances in THz sources and detectors both in CW [29], and pulse domain [13, 37], utilizing such sources has gained the interest of researcher for remote sensing applications in low-THz band. Pulse-based sources, despite having less radiated power, benefit from a broad bandwidth, high frequency stability, and low power consumption. Therefore, a custom-designed broadband THz pulse radiator is employed, which radiates a frequency comb with frequency tones ranging from 10s of GHz up to 1.1 THz [12]. The THz generation mechanism is based on the reverse recovery of a standard PIN diode device [51]. Similar to Step Recovery Diodes (SRD), PIN diodes also benefit from a sharp reverse recovery which can potentially

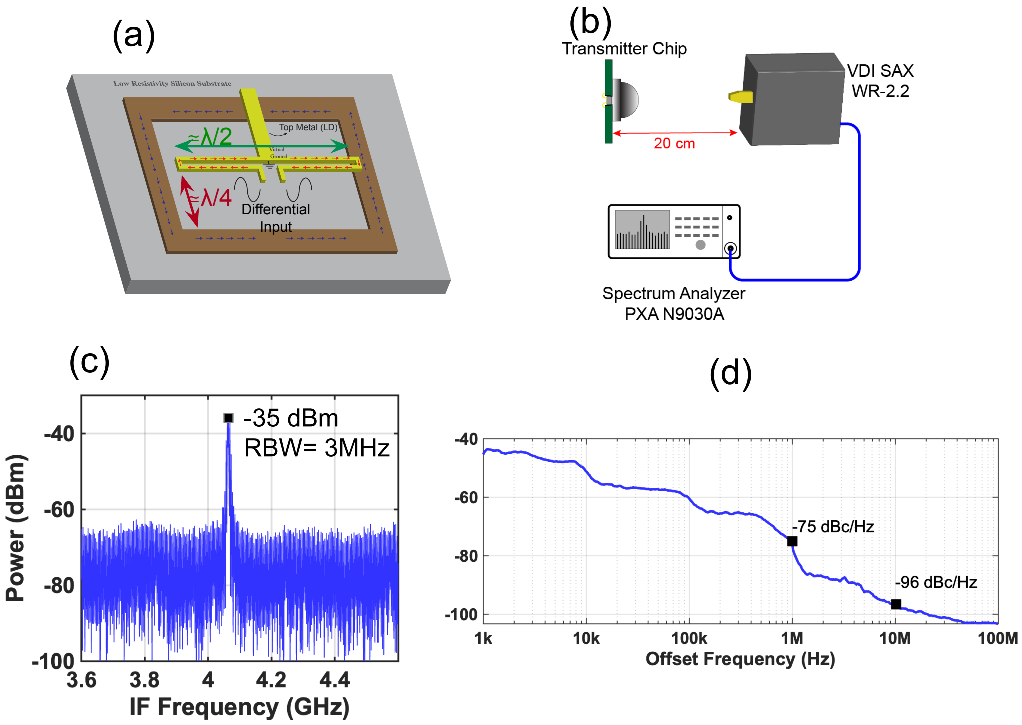

Figure 4.23: (a) Folded dipole antenna in differential mode. (b) EIRP measurement setup. (c) Received tone at 390 GHz, and (d) phase noise of the radiated tone.

be used to generate harmonics in THz band [19]. Fig. 4.21 depicts a block diagram of chip operation, and a micrograph of the chip.

At THz frequencies, off-chip antennas are not an option due to the high inductance of wirebonds and on-chip interconnects. In addition, radiating broadband pulses require a broadband antenna. Thus, a broadband CPW slot bow-tie in conjunction with high resistivity silicon lens is used. THz lens eliminates the substrate waveguide modes by extending the substrate silicon, resulting in higher efficiency and directivity.

As mentioned earlier, to detect sound vibrations, having a low-phase noise source is critical. Otherwise, in a case of a multi-tone vibration, the tones are mixed and cannot be distinguished. The repetition rate of pulses is locked to a low-phase noise source. Therefore, it benefits from high frequency stability and low phase noise. However, phase noise

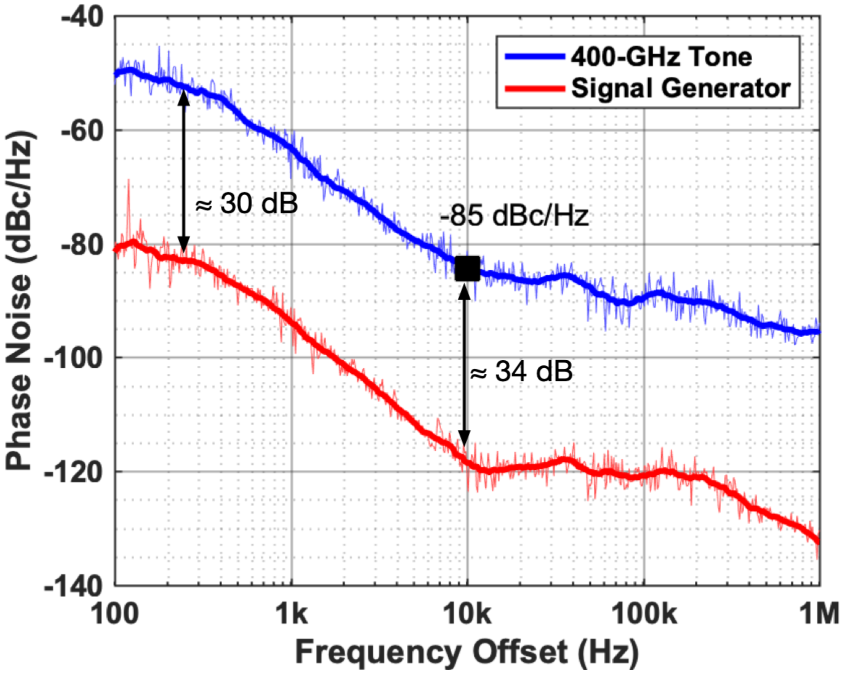

Figure 4.24: Comparison between the Phase noise of the tone at 400 GHz and input trigger generated by the signal generator.

deterioration due to frequency multiplication is inevitable, which is given by the following

$$\mathcal{L}_{Nf_0} = 20log(N) + \mathcal{L}_{f_0} \tag{4.18}$$

where N is the harmonic number and f_0 is the fundamental frequency. The phase noise of the chip at 400 GHz (32nd harmonic) when driven with a 12.5-GHz trigger is measured and shown in Fig. 4.24. The phase noise of the 400-GHz tone is roughly 30 dB above the input trigger (pulse repetition rate) generated by the signal generator. This is consistent with (4.18) and shows the minimal contribution of the circuit blocks noise sources on the phase noise of the radiated tones.

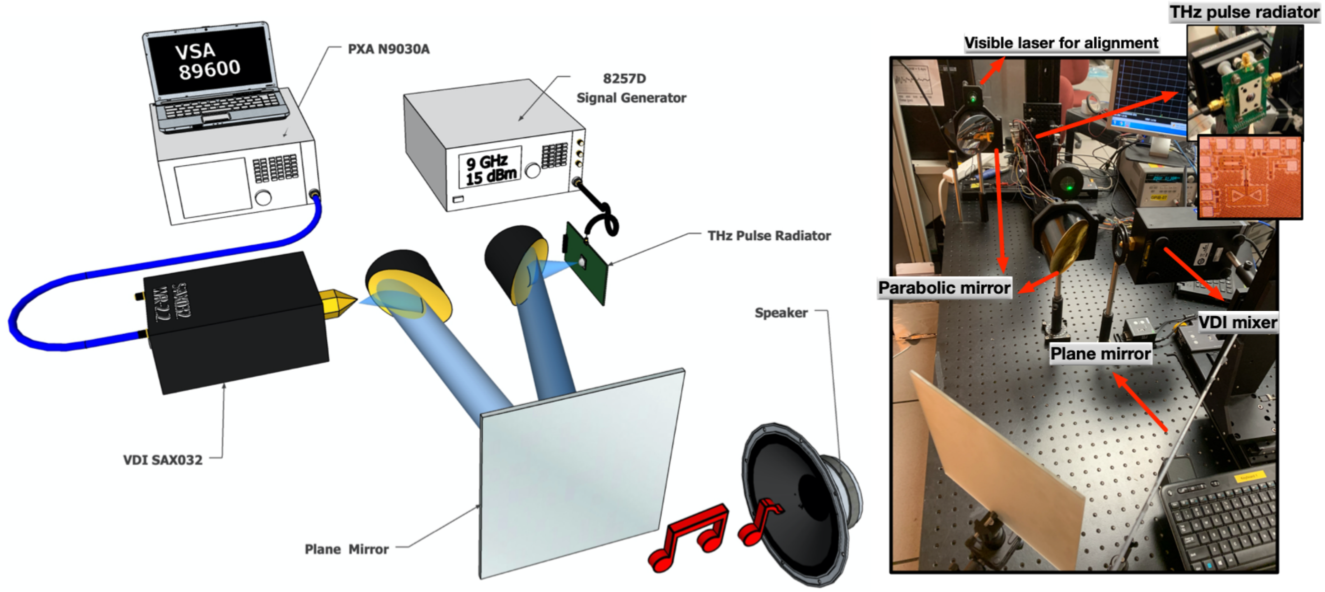

Figure 4.25: (a) A 3D view of the experimental setup used for micro-Doppler characterization and THz vibration sensing, (b) picture of the setup

4.4.3.2 THz CW Radiator

THz CW radiators benefit from higher radiated power. However, such radiators have low frequency stability and high phase noise in free running mode of operation. In this work, a THz CW radiator based on PIN diode reverse recovery [19] is used for interferometry measurements. Nonlinearity of the PIN diode in reverse recovery can ben exploited for strong harmonic generation in THz band. To push the PIN diode into reverse recovery mode, a mm-wave colpitts oscillator is utilized. Fig. 4.22 shows schematic of the THz radiator and the chip micrograph. A differential folded dipole antenna with a silicon lens is used for backside radiation at 390 GHz. Fig. 4.23 measurement setup and important specifications of the THz CW radiator. As shown, the phase noise of the radiated tone is -44 dBc/Hz at 1 kHz offset frequency in free running mode, which makes phase detection by I/Q analysis challenging. The Effective Isotropic Radiated Power (EIRP) of this chip is 13 dBm at 390 GHz.

4.4.4 Experimental setup and the Measurement results using a THz Pulse Radiator

The experimental setup is illustrated in Fig. 4.25. To direct the beams toward the target of interest, the radiated beams are collimated using an Off-Axis Parabolic (OAP) mirror. As demonstrated in [126, 101], precise collimation enables the propagation of THz waves over relatively long distances, which can go as high as 110 m. Using a similar setup in this work, the micro-Doppler signature of distant targets can be detected and recorded. Collimation is first performed with aid of two visible light lasers. After performing collimation using visible light, the laser is replaced with the source chip. The collimated THz beams then hit the surface of a plane mirror, which is vibrating by the mechanical sound waves generated using a commercial speaker. The reflected beams, which contain the information of sound waves, are focused on the receiver's antenna using another OAP mirror. The repetition rate of the THz pulse radiator is set to 5.5 GHz using a Keysight E8257D signal generator. Therefore a frequency comb with the spacing of 5.5 GHz is radiated. VDI SAX032 is used to downconvert the radiated tones in the WR-2.2 band (320 to 500 GHz). The IF signal is analyzed using Keysight PXA N9030A in conjunction with 89600 Vector Signal Analysis tool to capture the I/Q information of the IF. I/Q analysis allows us to observe the exact amount of time-domain phase change and to calculate the displacement due to vibrations. Note that in this measurement, the LO of the receiver and input trigger of the chip are not correlated. Therefore, the phase noise of the signal generator and LO negatively impacts the sensitivity and resolution. Micro-Doppler signatures of sound waves are investigated for different cases: mono-tone, multi-tone, chirp, and music. Each case will be analyzed in the subsequent sections.

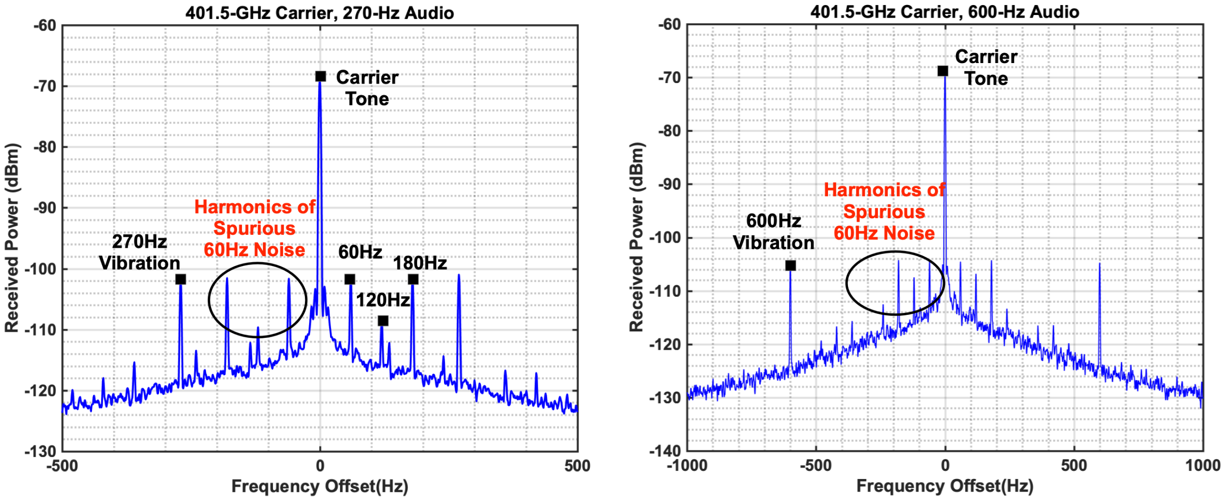

Figure 4.26: Spectrum of the received THz tone for various sound vibration frequencies.

4.4.4.1 Mono-tone Excitation

To show the carrier frequency modulation, audio tones of 270 and 600 Hz are produced separately using the speaker. Fig. 4.26 shows the spectrum for different vibration frequencies in mono-tone excitation for a carrier frequency of 401.5 GHz. Note that, the intensity of vibration at different frequencies depends on the texture and flexibility of the target (plane mirror). Since a rigid plane mirror is used as the reflector, the displacement caused by vibrations is small and inversely proportional to the vibration frequency.

The time-domain waveform of the phase is captured by performing I/Q analysis using VSA 89600. The amount of phase change is directly proportional to the vibration displacement. I/Q analysis provides a practical solution for characterizing vibrating targets in time domain. Using time-domain waveform, the exact amount of displacement can be calculated based on:

$$D = \frac{\lambda \phi}{4\pi} \tag{4.19}$$

Where ϕ is the instantaneous phase of the THz tone. Fig. 4.27 shows the change of phase

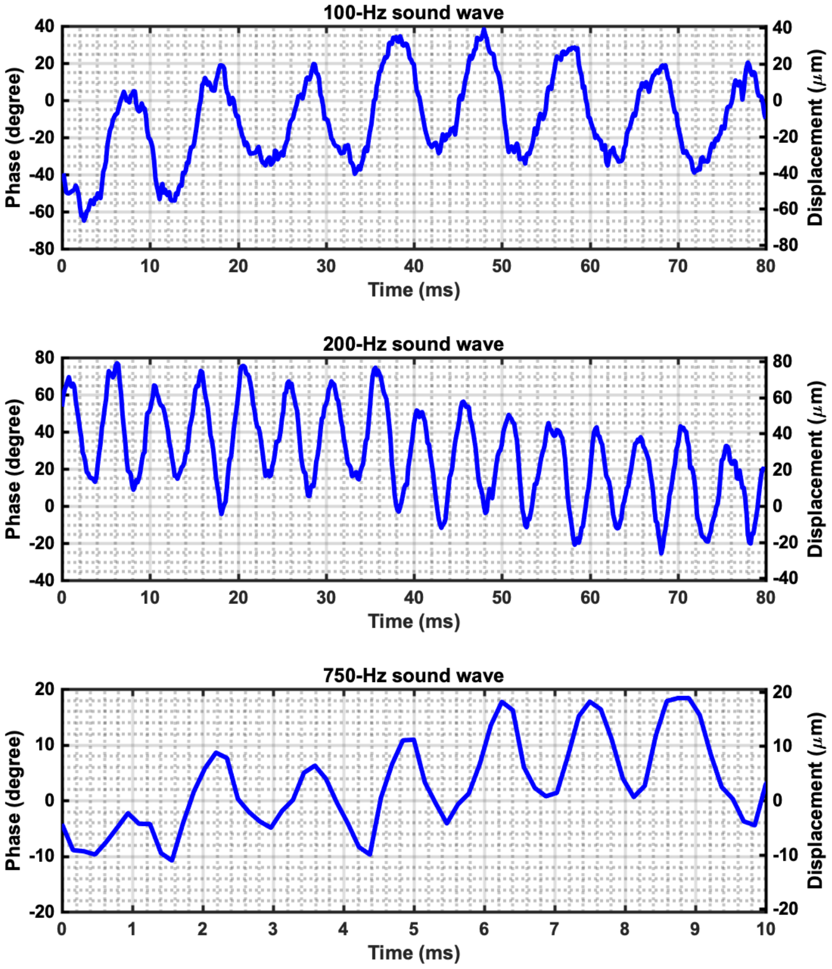

Figure 4.27: Time-domain phase waveform captured by performing I/Q analysis on down-converted THz carrier.

and corresponding displacement versus time for different excitation audio tones.

4.4.4.2 Chirp Audio

In order to analyze the behavior of the scattering surface, a chirp vibration can be used since it characterizes the surface across a frequency range rather than a single frequency point. The micro-Doppler signature is shown in Fig. 4.28 when the surface of the mirror is excited via chirp audio.

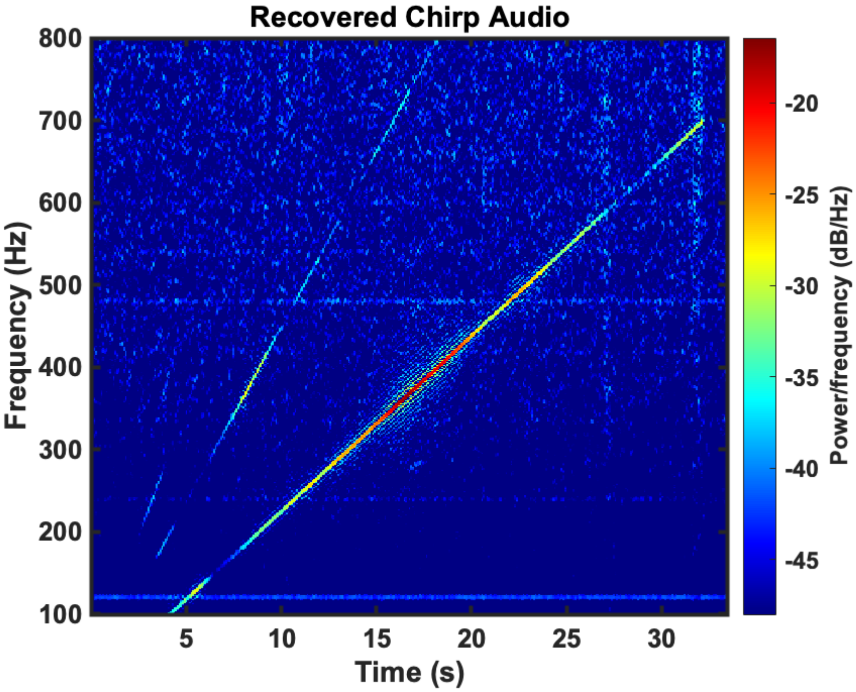

Figure 4.28: Spectrogram of the recovered audio chip.

4.4.4.3 Arbitrary Audio

Fig. 4.29 shows the spectrogram when a piece of music is played. This music track has various frequency components. As shown, using this measurement setup, most frequency components are recovered and this setup can be used to measure and characterize complex vibrations.

4.4.5 Phase Noise Cancellation

The micro-Doppler detection quality is limited by the power of the radiated tones and SNR. However, when the power of tones is well above the noise level, the phase noise of the radiated tones becomes the limiting factor instead. As explained in section III, due to frequency multiplication, phase noise deteriorates at high frequencies. In the setup of Fig. 4.25, the noise sources of the THz pulse radiator and VDI SAX032 are not correlated.

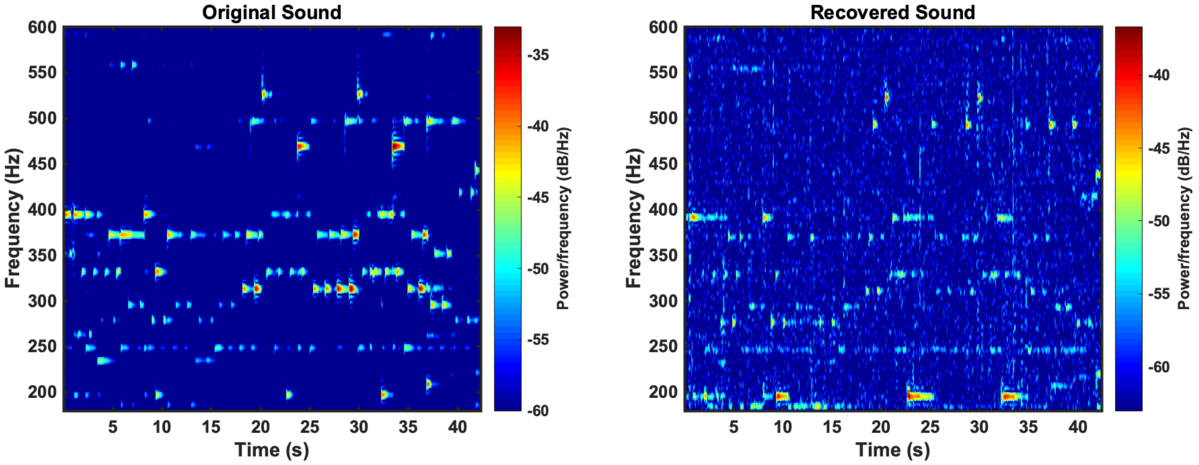

Figure 4.29: Comparison between (a) the original sound and b) the recovered sound track.

In addition, frequency multiplication is occurring at both transmitter and receiver sides. Therefore the phase noise of the IF tone is significantly impacted limiting the sensitivity for the frequency tones that fall below the noise skirt. In CW radars, the effect of phase noise is canceled by feeding correlated LOs to both transmitter and receivers increasing the spectral resolution and sensitivity. In this section, a similar technique is employed. Note that zero-IF commercial receivers are not available in THz. Considering that phase noise of THz tones is mostly due to frequency multiplication rather than the noise contribution of the radiator circuit, using correlated sources to drive THz pulse radiator and receiver can decrease the phase noise caused by frequency multiplication. To elaborate, consider the THz chip input trigger as:

$$X(t) = cos(\omega_0 t + \phi_n) \tag{4.20}$$

where ϕ_n is the phase noise and ω_0 is the frequency of the input trigger to the chip. The Nth harmonic of THz tone after reflection from the vibrating target can be written as:

$$R(t) = cos(N\omega_0 t + N\phi_n + \phi_s(t)) \tag{4.21}$$

where $\phi_s(t)$ is the phase change due to vibrations. $X(t)$ is also fed to the harmonic mixer at the receiver side. Consider the case that the harmonic mixer downconverts the THz tone

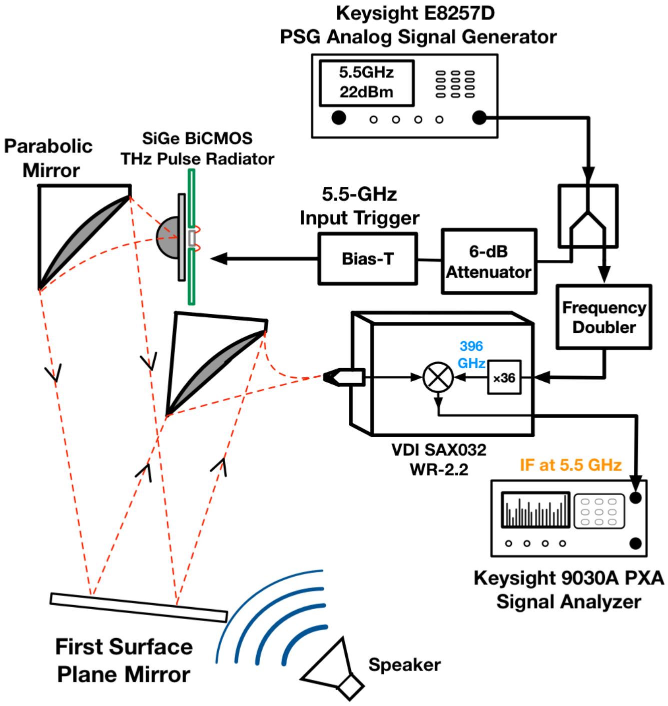

Figure 4.30: Modified experimental setup for phase noise suppression.

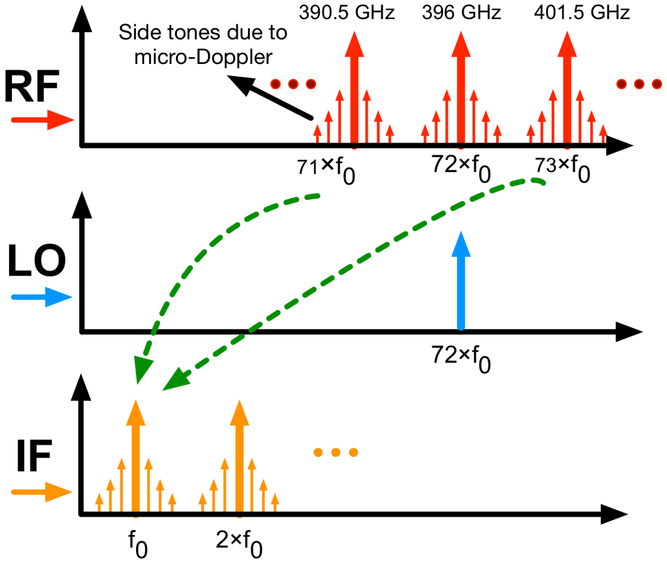

Figure 4.31: Down conversion of adjacent tones in phase noise suppression setup.

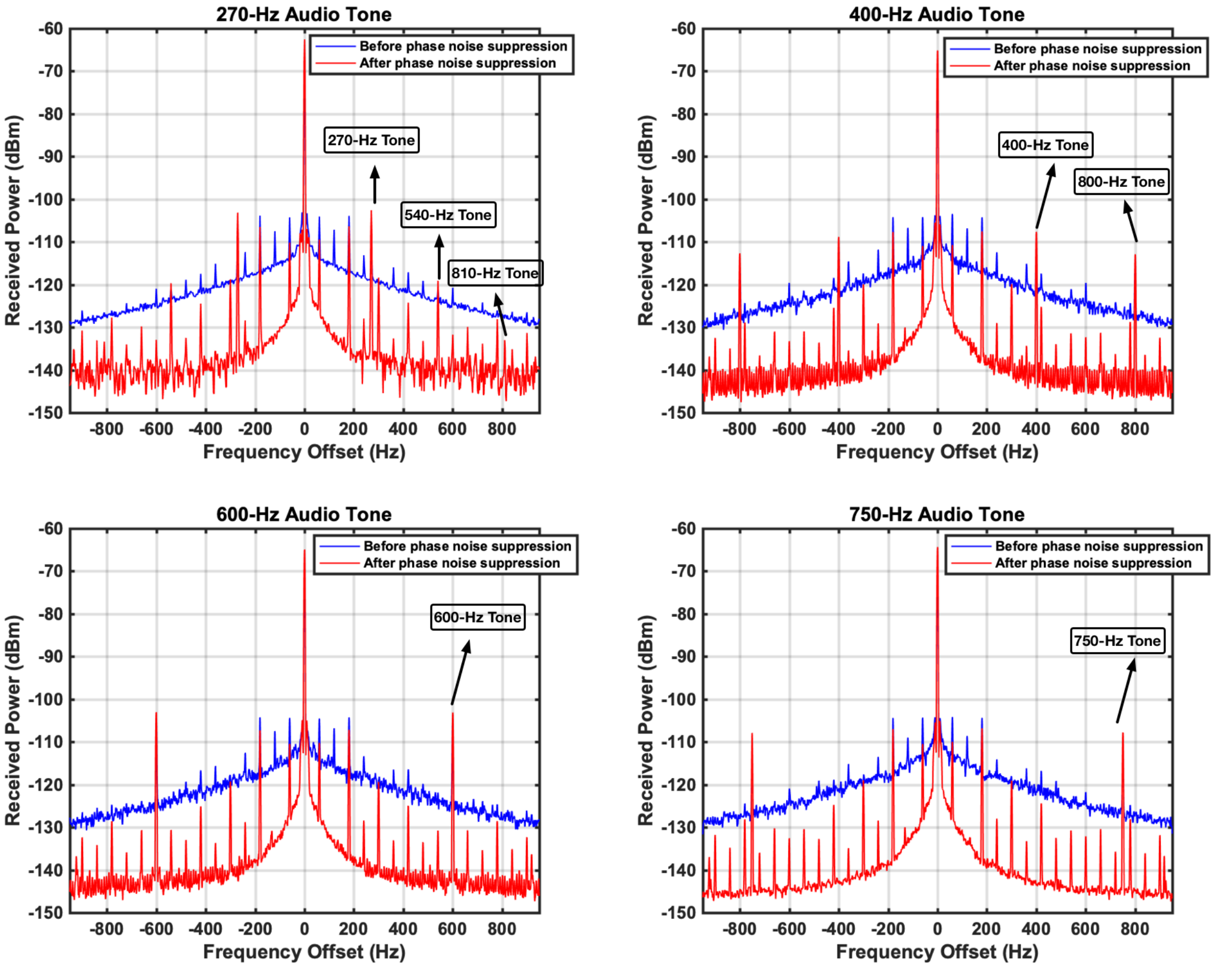

Figure 4.32: Spectrum of the received THz tone using phase noise suppression technique.

by $N-1$ factor. The resultant IF signal can be expressed as:

$$Y(t) = cos(N\omega_0 t + N\phi_n + \phi_s(t)) \times cos((N-1)\omega_0 t + (N-1)\phi_n) \quad (4.22)$$

$$Y(t)_{IF} = cos(\omega_0 t + \phi_n + \phi_s(t)) \quad (4.23)$$

As seen, after downconversion with a correlated signal the phase noise goes back to the initial value if the noise contribution of the mixer is neglected. Therefore, the measurement setup of Fig. 4.30 is employed. The signal from the source is divided between the pulse radiator and VDI SAX032 using a power splitter. In this setup, the chip is driven with a 5.5-GHz trigger

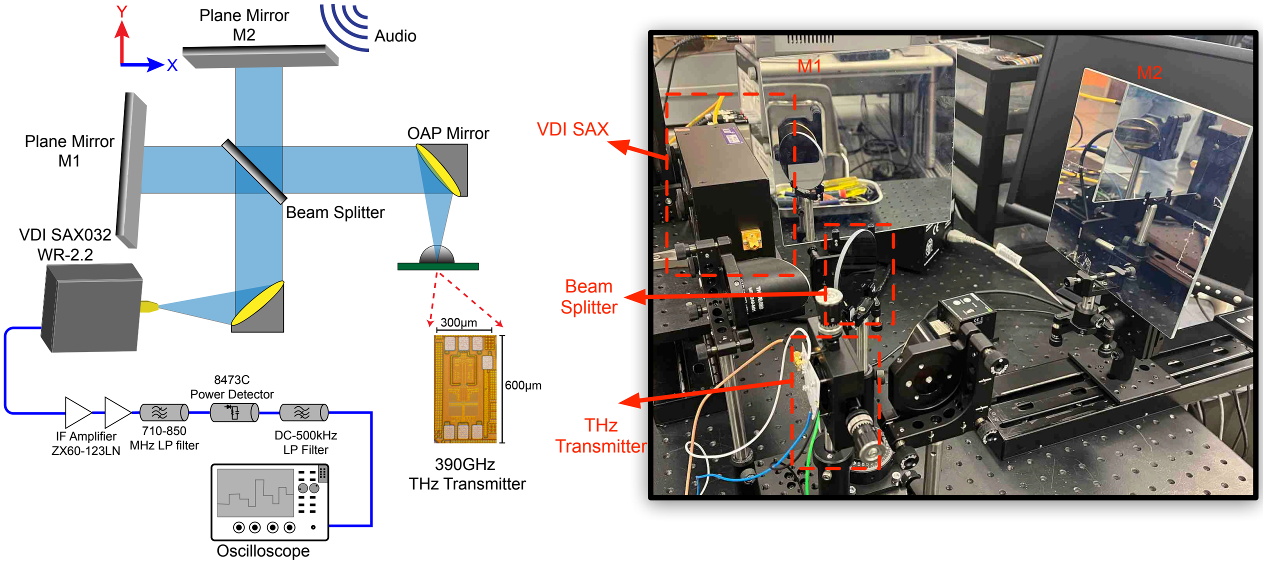

Figure 4.33: Measurement setup for interferometry-based vibration sensing.

signal resulting in a frequency comb with 5.5-GHz spacing. The VDI SAX032 consists of a series of internal frequency multipliers with an overall multiplication factor 36. Additionally, an external frequency doubler is employed so that LO falls in 320–500 GHz band. As illustrated in Fig. 4.31, the tones at 401.5 and 390.5 GHz are downconverted to 5.5-GHz IF. Fig. 4.32 shows and compares the received tones using the measurement setup of Fig. 4.25 and Fig. 4.30 for 270, 400, 600, and 750 Hz audio vibrations. The amount of phase noise has improved 10 (for high-frequency vibrations) to 22 dB (for low-frequency vibrations), thereby improving the overall sensitivity of the setup and enabling the detection of vibration displacements as low as 10 um. However, spurious 60 Hz tones and their harmonics, as observed in Fig. 4.32, caused by coupling of power line noise pose a limit for the detection of vibrations in these frequencies. Using 60-Hz hum eliminators for instruments can remove the spurs and improve the sensitivity in these frequencies.

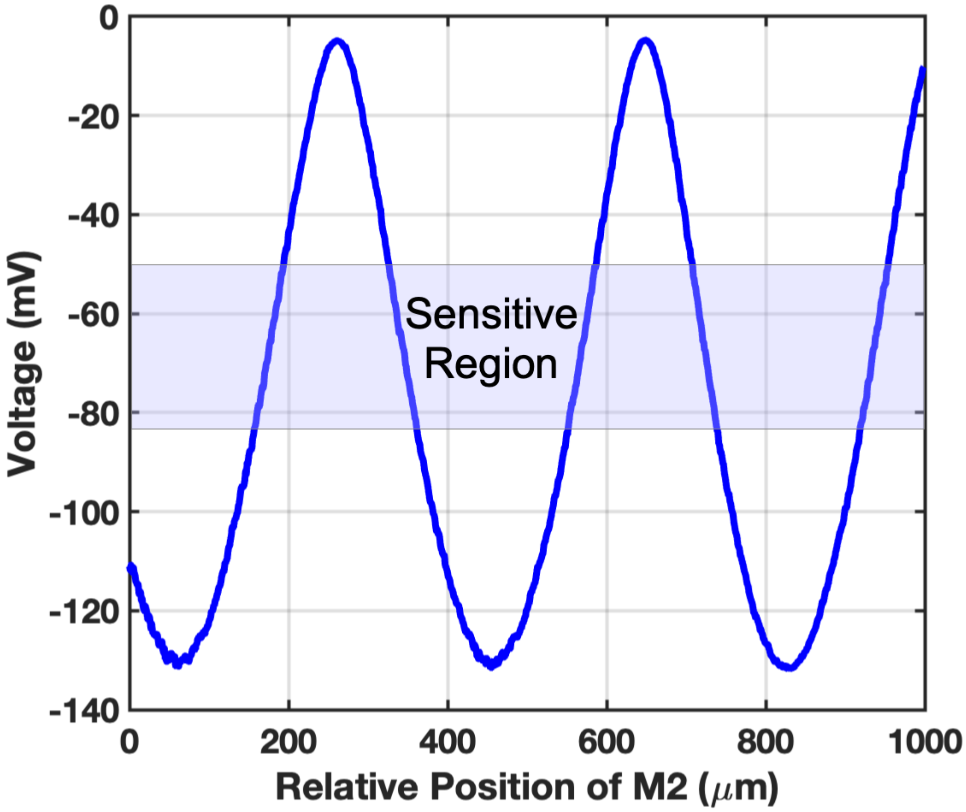

Figure 4.34: Recorded DC voltage when sweeping the position of the mirror.

4.4.6 Interferometry Experimental Setup and Measurement Results

In this section, a THz CW radiator is used to capture the vibrations. Due to the high phase noise of this radiator, I/Q analysis for phase detection, similar to the previous section, is not feasible. Therefore, the interferometry technique is used to reconstruct the original audio from the surface vibrations. Unlike section IV, the limiting factor is not the phase noise, but rather the signal to noise ratio. Fig 4.33 demonstrates the interferometry measurement using the CW THz radiator chip. Similar to previous sections, OAP mirrors are used to collimate and focus THz beams. The THz waves from the chip are first collimated and then divided using a beam splitter. The THz waves travel in two different directions and they are reflected by two plane mirrors, where one of the mirrors is vibrating by sound waves. The reflected beams are recombined at the receiver (VDI SAX module). At the receiver side,

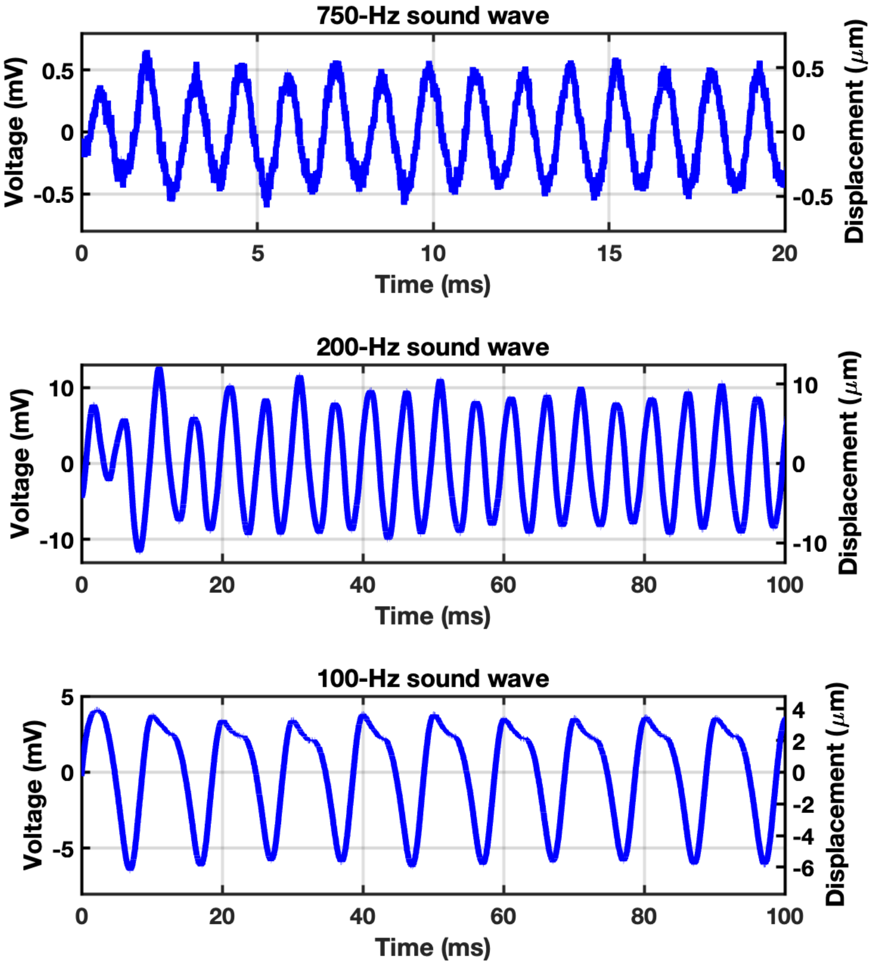

Figure 4.35: Time-domain voltage waveform captured by power detector and corresponding displacement for different sound waves.

the IF signal is amplified by low-noise baseband amplifiers to generate the desired signal for the power detector block. The power detector directly captures the phase information by measuring the signal intensity, which is the third term in (4.17). The output of the power detector is recorded using an oscilloscope.

In the first measurement, to characterize the setup, by moving M2 mirror along Y axis, the intensity of the received beam, (4.17), is measured. Fig. 4.34 shows the DC voltage on the oscilloscope versus the position of the mirror. The period of the curve in Fig. 4.34 is equal to half of the wavelength. As specified in Fig. 4.34, to achieve the highest sensitivity,

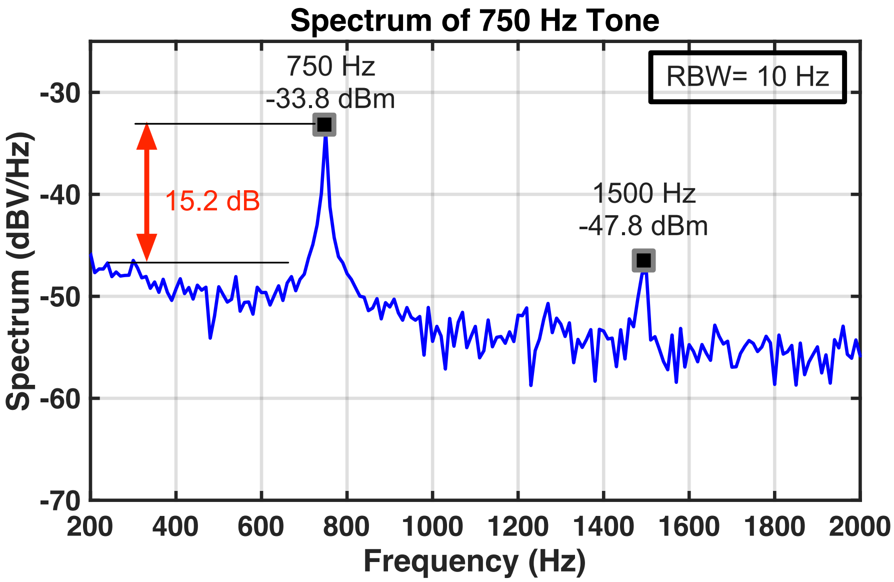

Figure 4.36: Spectrum of the 750-Hz sinusoidal vibration with 10-Hz RBW. Sensitivity of 30 nm is predicted based on 15.2-dB SNR for 0.5-μm vibration.

M2 mirror is positioned in the sensitive region where the highest slope is observed. Fig. 4.34 can also be used to calculate the displacement of the mirror with high precision.

Moreover, the M2 mirror is vibrated by sound waves with different frequencies in this setup. Fig. 4.35 shows the raw time-domain waveforms, which are recorded by the oscilloscope. As observed, the displacement is different for different frequencies, which is attributed to the property of the vibrating mirror. Note that displacement is calculated based on the data from Fig. 4.34. Note that compared to results of monotone excitation of section IV, higher resolution is observed enabling the detection of more subtle vibrations. Fig. 4.36 shows the spectrum for the case of 750-Hz vibration, which can be used to estimate the sensitivity of Fig. 4.33. The SNR is 15.2 dB for the case of 0.5 μm for vibration frequencies above 200 Hz, which corresponds to a sensitivity of $\approx$ 30 nm for 10 Hz RBW (min SNR of 3 dB is considered). Note that by recording the signal over a longer time or lowering the RBW, the resolution can be improved. This work shows significantly higher sensitivity compared to CW radars, which stems from different factors. Part of the error in CW radars

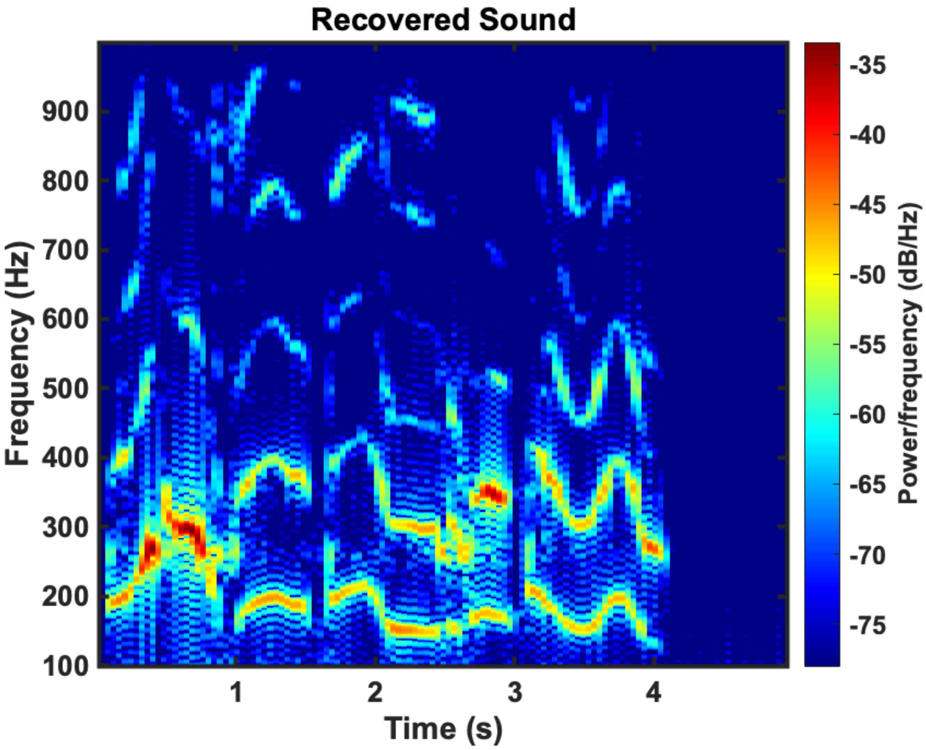

Figure 4.37: Spectrogram of the recovered sentence: "Welcome to ISL Lab at UCLA", which is generated by a speaker.

is due to phase/amplitude imbalance between I and Q, which is not case in Fig. 4.33. Moreover, carrier frequency of 390 GHz enables higher resolution compared to CW radars with lower carrier frequency [127, 128]. Table 4.3 gives a comparison between the interferometry setup of this work with previously reported interferometry radars.

To demonstrate the precision of interferometry measurements (setup of Fig. 4.33), the case of recorded speech audio is considered. The recovered spectrogram is shown in Fig. 4.37. As observed, the speech patterns are preserved in raw recovered data. Because of the high sensitivity of THz interferometry, the recovered speech is recognizable without any further processing.

Table 4.3: Comparison with CW and FMCW radars

Reference	**This work**	**[127]**	**[128]**	**[129]**	**[130]**	**[131]**	**[132]**
Frequency(GHz)	**390**	125	100	122–170	121–127	60	94
Technique	**Interferometry**[†]	CW Radar	FMCW Radar	FMCW Radar	FMCW Radar	CW Radar	FMCW Radar
Sensitivity(μm)	**0.03**[‡]	0.1	0.3[*]	1	6	20	3

[†] This is not a radar but rather an interferometry setup using a silicon THz source.

[‡] Predicted sensitivity with 3-dB SNR and 10-Hz RBW.

[*] Predicted sensitivity with 10-dB SNR and 0.1-Hz RBW.

4.4.7 Conclusion

In this work, various approaches for non-contact vibration sensing using a low-power silicon-based THz pulse radiator and a THz CW radiator are proposed. By picking up the sound vibrations using THz carrier tones, the original sound waves were reconstructed. The measurements were performed for mono-tone, chirp sound, and a music track. Complex vector analysis was performed to capture the time-domain phase change of the THz carrier tones. In addition, a new approach for phase noise reduction was proposed resulting in the improvement of the sensitivity and quality of vibration sensing. A THz interferometry setup is demonstrated that allows using a high-phase noise CW radiator chip to detect vibrations with a sensitivity of 30 nm. This work does not demonstrate an interferometry radar chip but rather an interferometry setup that enables using a free running THz source to perform different sensing measurements including vibration sensing.

4.5 Closing Remarks

In this dissertation, I elaborated on potential applications of THz band and how it can be used as an alternative for expensive bulky optical systems. Moreover, I have addressed the challenges of THz generation in silicon-based technologies and how these pose a limit on implementation of THz systems. Different techniques have been suggested to tackle the challenges of THz generation using low-cost silicon technologies; however, field of THz circuit design is still in early stages and requires further research. The recently proposed silicon THz transmitters and receivers still suffer from low radiation power and high conversion loss, respectively. Therefore, they are not yet a reliable solution for the aforementioned potential applications. In chapter 2, I introduced a novel technique based on PIN diode for THz pulse generation resulting in significant improvement in radiation power across the sub-THz band. I utilized a PIN diode device in reverse recovery mode to generate THz pulses for the first time. Considering that this device had not been used for THz pulse generation before, further research is needed to fully appreciate its potential in the THz band. In chapter 3, I extended the idea of PIN diode reverse recovery to the CW domain and demonstrated a CW 2×3 THz radiator array. Utilizing PIN diode in the CW domain resulted in significant boost in radiation power and efficiency. This paves the way for the implementation of high-power large-scale THz radiator array in future. In chapter 4, I showed utilized my custom-designed chip for different types of applications. This shows the practicality of these chips and how can they can be used to solve real world problems. I employed Pulse/comb radiator chips to perform gas spectroscopy and characterize atmospheric absorption. Moreover, I utilized a low-cost broadband THz radiator chip to characterize plasma physics, which is conventionally done by expensive microwave interferometers. Moreover, I used THz chips to record audio vibrations on a reflective surface and reconstructed the original audio using these recordings. Low cost THz systems for vibration sensing can be a potential replacement for currently bulky expensive laser-based vibration sensors.

With improvement in silicon fabrication technologies and a further increase in the speed of transistors, performance of silicon-based THz systems is expected to improve in near future. Moreover, due to the emergence of new VR and IOT applications, demand for higher communication speed is inevitable. This requires wide available bandwidth, which is only available in the THz band. Therefore, although the THz domain is barely explored, in near future I expect that the focus of the industry shifts toward system design in higher frequency bands including sub-THz band. Therefore, Researchers in this field should put in effort and develop new techniques in integrated THz circuit design to facilitate the availability of THz-based systems for daily applications in near future.

REFERENCES

[1] H. Rahmani, Y. Sun, M. Kherwa, S. Pal, and A. Babakhani, "Coherent radiation from a swarm of wirelessly powered and synchronized sensor nodes," *IEEE Sensors Journal*, vol. 20, no. 19, pp. 11 608–11 616, 2020.

[2] H. Rahmani and A. Babakhani, "An integrated battery-less wirelessly powered rfid tag with clock recovery and data transmitter for uwb localization," in *2020 IEEE/MTT-S International Microwave Symposium (IMS)*, 2020, pp. 460–463.

[3] H. Elayan, O. Amin, B. Shihada, R. M. Shubair, and M. Alouini, "Terahertz band: The last piece of rf spectrum puzzle for communication systems," *IEEE Open Journal of the Communications Society*, vol. 1, pp. 1–32, 2020.

[4] M. Tamosiunaite, S. Tamosiunas, M. Zilinskas, and G. Valusis, "Atmospheric attenuation of the terahertz wireless networks," in *Broadband Communications Networks*, A. Haidine and A. Aqqal, Eds. Rijeka: IntechOpen, 2018, ch. 9. [Online]. Available: https://doi.org/10.5772/intechopen.72205

[5] J. Jang, I. Habibagahi, H. Rahmani, and A. Babakhani, "Wirelessly powered, battery-less closed-loop biopotential recording ic for implantable leadless cardiac monitoring applications," in *2021 IEEE Biomedical Circuits and Systems Conference (BioCAS)*, 2021, pp. 1–4.

[6] N. Akter, M. M. Hasan, and N. Pala, "A review of thz technologies for rapid sensing and detection of viruses including sars-cov-2," *Biosensors*, vol. 11, no. 10, 2021. [Online]. Available: https://www.mdpi.com/2079-6374/11/10/349

[7] T. C. Bowman, M. El-Shenawee, and L. K. Campbell, "Terahertz imaging of excised breast tumor tissue on paraffin sections," *IEEE Transactions on Antennas and Propagation*, vol. 63, no. 5, pp. 2088–2097, 2015.

[8] M. M. Assefzadeh and A. Babakhani, "Broadband thz spectroscopic imaging based on a fully-integrated 4×2 digital-to-impulse radiating array with a full-spectrum of 0.03–1.03thz in silicon," in *2016 IEEE Symposium on VLSI Technology*, 2016, pp. 1–2.

[9] S. Razavian *et al.*, "Thz micro-doppler measurements based on a silicon-based picosecond pulse radiator," in *IEEE MTT-S Int. Microw. Symp. Dig.*, Jun. 2019, pp. 309–311.

[10] S. Razavian and A. Babakhani, "Multi-spectral thz micro-doppler radar based on a silicon-based picosecond pulse radiator," in *IEEE MTT-S Int. Microw. Symp. Dig.*, Aug. 2020, pp. 787–790.

[11] S. Razavian, J. Han, B. Jamali, P. Pribyl, M. Hosseini, Y. Mehta, M. Forghani, W. Gekelman, and A. Babakhani, "Plasma characterization using a silicon-based terahertz frequency comb radiator," *IEEE Sensors Letters*, vol. 4, no. 9, pp. 1–4, 2020.

[12] S. Razavian and A. Babakhani, "Silicon integrated thz comb radiator and receiver for broadband sensing and imaging applications," *IEEE Transactions on Microwave Theory and Techniques*, vol. 69, no. 11, pp. 4937–4950, 2021.

[13] M. M. Assefzadeh and A. Babakhani, "An 8-psec 13dbm peak eirp digital-to-impulse radiator with an on-chip slot bow-tie antenna in silicon," in *2014 IEEE MTT-S International Microwave Symposium (IMS2014)*, 2014, pp. 1–4.

[14] M. Forghani and A. Babakhani, "A cmos terahertz pulse radiator with zero dc power consumption based on nonlinear transmission line sharpening effect," in *2021 46th International Conference on Infrared, Millimeter and Terahertz Waves (IRMMW-THz)*, 2021, pp. 1–2.

[15] P. Chen, M. M. Assefzadeh, and A. Babakhani, "A nonlinear q-switching impedance technique for picosecond pulse radiation in silicon," *IEEE Transactions on Microwave Theory and Techniques*, vol. 64, no. 12, pp. 4685–4700, 2016.

[16] R. Han and E. Afshari, "A high-power broadband passive terahertz frequency doubler in cmos," *IEEE Transactions on Microwave Theory and Techniques*, vol. 61, no. 3, pp. 1150–1160, 2013.

[17] S. Razavian and A. Babakhani, "A thz pulse radiator based on pin diode reverse recovery," in *IEEE BiCMOS Compound Semicond. Integr. Circuits Technol. Symp.*, Nov. 2019, pp. 1–4.

[18] S. Razavian and A. Babakhani, "A fully integrated coherent 50–500-ghz frequency comb receiver for broadband sensing and imaging applications," in *Radio Freq. Integr. Circuits Symp.*, Aug. 2020, pp. 231–234.

[19] S. Razavian and A. Babakhani, "A highly power efficient 2×3 pin-diode-based intercoupled thz radiating array at 425ghz with 18.1dbm eirp in 90nm sige bicmos," in *2022 IEEE International Solid- State Circuits Conference (ISSCC)*, vol. 65, 2022, pp. 1–3.

[20] R. Jain, P. Hillger, J. Grzyb, and U. R. Pfeiffer, "A 0.42thz 9.2dbm 64-pixel source-array soc with spatial modulation diversity for computational terahertz imaging," in *Proc. IEEE Int. Solid-State Circuits Conf.*, Feb. 2020, pp. 440–442.

[21] H. Saeidi, S. Venkatesh, X. Lu, and K. Sengupta, "Thz prism: One-shot simultaneous multi-node angular localization using spectrum-to-space mapping with 360-to-400ghz broadband transceiver and dual-port integrated leaky-wave antennas," in *Proc. IEEE Int. Solid-State Circuits Conf.*, vol. 64, Feb. 2021, pp. 314–316.

[22] H. Saeidi, S. Venkatesh, X. Lu, and K. Sengupta, “Thz prism: One-shot simultaneous localization of multiple wireless nodes with leaky-wave thz antennas and transceivers in cmos,” *IEEE Journal of Solid-State Circuits*, vol. 56, no. 12, pp. 3840–3854, 2021.

[23] S. Hara *et al.*, “300-ghz cmos transceiver for terahertz wireless communication,” in *Asia-Pacific Microwave Conference (APMC)*, Nov. 2018, pp. 429–431.

[24] A. Standaert and P. Reynaert, “A 410 ghz ook transmitter in 28 nm cmos for short distance chip-to-chip communications,” in *2018 IEEE Radio Frequency Integrated Circuits Symposium (RFIC)*, 2018, pp. 240–243.

[25] A. D’Arco, M. Di Fabrizio, V. Dolci, M. Petrarca, and S. Lupi, “Thz pulsed imaging in biomedical applications,” *J. Phys., Condens. Matter*, vol. 5, no. 2, Apr. 2020.

[26] K. Schmalz, N. Rothbart, P. F. . Neumaier, J. Borngräber, H. Hübers, and D. Kissinger, “Gas spectroscopy system for breath analysis at mm-wave/thz using sige bicmos circuits,” *IEEE Trans. Microw. Theory Techn.*, vol. 65, no. 5, pp. 1807–1818, 2017.

[27] Y. Mehta, S. Razavian, K. Schwarm, R. M. Spearrin, and A. Babakhani, “Terahertz gas-phase spectroscopy of co using a silicon-based picosecond impulse radiator,” in *Proc. CLEO, Sci. Innov.*, May. 2020, pp. 1–2.

[28] D. Headland, R. Zatta, P. Hillger, and U. R. Pfeiffer, “Terahertz spectroscope using cmos camera and dispersive optics,” *IEEE Trans. THz Sci. Technol.*, vol. 10, no. 5, pp. 513–523, Sep. 2020.

[29] H. Saeidi, S. Venkatesh, C. R. Chappidi, T. Sharma, C. Zhu, and K. Sengupta, “29.9 a 4×4 distributed multi-layer oscillator network for harmonic injection and thz beamforming with 14dbm eirp at 416ghz in a lensless 65nm cmos ic,” in *2020 IEEE International Solid- State Circuits Conference - (ISSCC)*, 2020, pp. 256–258.

[30] E. Öjefors, B. Heinemann, and U. R. Pfeiffer, “Active 220- and 325-ghz frequency multiplier chains in an sige hbt technology,” *IEEE Trans. Microw. Theory Techn.*, vol. 59, no. 5, pp. 1311–1318, May. 2011.

[31] C. Wang and R. Han, “Rapid and energy-efficient molecular sensing using dual mm-wave combs in 65nm cmos: A 220-to-320ghz spectrometer with 5.2mw radiated power and 14.6-to-19.5db noise figure,” in *Proc. IEEE Int. Solid-State Circuits Conf.*, Feb. 2017, pp. 302–303.

[32] C. Jiang *et al.*, “A fully integrated 320 ghz coherent imaging transceiver in 130 nm sige bicmos,” *IEEE J. Solid-State Circuits*, vol. 51, no. 11, pp. 2596–2609, Nov. 2016.

[33] S. Matsuura, M. Tani, and K. Sakai, “Generation of coherent terahertz radiation by photomixing in dipole photoconductive antennas,” *Appl. Phys. Lett.*, vol. 70, no. 5, pp. 559–561, 1997.

[34] N. Chimot, J. Mangeney, L. Joulaud, P. Crozat, H. Bernas, K. Blary, and J. F. Lampin, "Terahertz radiation from heavy-ion-irradiated $in_{0.53}ga_{0.47}as$ photoconductive antenna excited at 1.55μm," *Appl. Phys. Lett.*, vol. 87, no. 19, p. 193510, 2005.

[35] B. Salem *et al.*, "Pulsed photoconductive antenna terahertz sources made on ion-implanted gaas substrates," *J. Phys., Condens. Matter*, vol. 17, no. 46, pp. 7327–7333, Nov. 2005.

[36] B. Jamali, S. Razavian, and A. Babakhani, "Fully electronic silicon-based THz pulse sources and detectors," in *Terahertz Photonics*, vol. 11348, International Society for Optics and Photonics. SPIE, 2020, pp. 41 – 48.

[37] F. Khoeini, B. Hadidian, K. Zhang, and E. Afshari, "Reflection-based short pulse generation in cmos," *IEEE Solid-State Circuits Lett.*, vol. 3, pp. 318–321, Aug. 2020.

[38] R. Han and E. Afshari, "A 260ghz broadband source with 1.1mw continuous-wave radiated power and eirp of 15.7dbm in 65nm cmos," in *Proc. IEEE Int. Solid-State Circuits Conf.*, Feb. 2013, pp. 138–139.

[39] M. M. Assefzadeh and A. Babakhani, "Broadband oscillator-free thz pulse generation and radiation based on direct digital-to-impulse architecture," *IEEE J. Solid-State Circuits*, vol. 52, no. 11, pp. 2905–2919, Nov. 2017.

[40] L. Liu and G. Fang, "A novel uwb sampling receiver and its applications for impulse gpr systems," *IEEE Geoscience and Remote Sensing Letters*, vol. 7, no. 4, pp. 690–693, May. 2010.

[41] A. W. DiVergilio, J. J. Pekarik, and V. Jain, "An electrothermal pin diode model with substrate injection," in *IEEE Bipolar/BiCMOS Circuits and Technol. Meeting*, Sep./Oct. 2014, pp. 207–210.

[42] M. Hosseini and A. Babakhani, "A fully integrated 20-500-ghz coherent detector with 2-hz frequency resolution," in *2020 IEEE BiCMOS and Compound Semiconductor Integrated Circuits and Technology Symposium (BCICTS)*, 2020, pp. 1–4.

[43] B. Jamali, S. Razavian, and A. Babakhani, *Fully Electronic Generation and Detection of THz Picosecond Pulses and Their Applications.* Cham: Springer International Publishing, 2022, pp. 457–459.

[44] W. Knap *et al.*, "Plasma wave detection of sub-terahertz and terahertz radiation by silicon field-effect transistors," *Appl. Phys. Lett.*, vol. 85, no. 4, pp. 675–677, Jul. 2004.

[45] B. Jamali and A. Babakhani, "A fully integrated 50–280-ghz frequency comb detector for coherent broadband sensing," *IEEE Trans. THz Sci. Technol.*, vol. 9, no. 6, pp. 613–623, Nov. 2019.

[46] K. Statnikov, J. Grzyb, B. Heinemann, and U. R. Pfeiffer, “160-ghz to 1-thz multi-color active imaging with a lens-coupled sige hbt chip-set,” *IEEE Trans. Microw. Theory Techn.*, vol. 63, no. 2, pp. 520–532, 2015.

[47] V. Jain *et al.*, “Schottky barrier diodes in 90nm sige bicmos process operating near 2.0 thz cut-off frequency,” in *IEEE Bipolar/BiCMOS Circuits and Technol. Meeting*, Sep./Oct. 2013, pp. 73–76.

[48] R. Han, Y. Zhang, Y. Kim, D. Y. Kim, H. Shichijo, E. Afshari, and K. K. O, “Active terahertz imaging using schottky diodes in cmos: Array and 860-ghz pixel,” *IEEE J. Solid-State Circuits*, vol. 48, no. 10, pp. 2296–2308, Oct. 2013.

[49] P. Song, R. L. Schmid, A. Ç. Ulusoy, and J. D. Cressler, “A high-power, low-loss w-band spdt switch using sige pin diodes,” in *Radio Freq. Integr. Circuits Symp.*, Jun. 2014, pp. 195–198.

[50] C. Veerappan and E. Charbon, “A low dark count p-i-n diode based spad in cmos technology,” *IEEE Trans. Electron Devices.*, vol. 63, no. 1, pp. 65–71, Jan. 2016.

[51] K. Schunemann and J. Muller, “A charge-control model of the pin diode,” *IEEE Trans. Electron Devices.*, vol. 23, no. 10, pp. 1150–1158, Oct. 1976.

[52] I. Coddington, N. Newbury, and W. Swann, “Dual-comb spectroscopy,” *Optica*, vol. 3, no. 4, pp. 414–426, Apr. 2016.

[53] S. Wang, A. Niknejad, and R. Brodersen, “Circuit modeling methodology for uwb omnidirectional small antennas,” *IEEE J. Sel. Areas Commun.*, vol. 24, no. 4, pp. 871–877, Apr. 2006.

[54] H. Jalili and O. Momeni, “A 0.46-thz 25-element scalable and wideband radiator array with optimized lens integration in 65-nm cmos,” *IEEE Journal of Solid-State Circuits*, vol. 55, no. 9, pp. 2387–2400, 2020.

[55] A. Muraviev, D. Konnov, and K. Vodopyanov, “Broadband high-resolution molecular spectroscopy with interleaved mid-infrared frequency combs,” *Sci. Rep.*, vol. 10, Oct. 2020.

[56] W. Stutzman, “Estimating directivity and gain of antennas,” *IEEE Antennas Propag. Mag.*, vol. 40, no. 4, pp. 7–11, Aug. 1998.

[57] A. Arbabian, S. Callender, S. Kang, M. Rangwala, and A. M. Niknejad, “A 94 ghz mm-wave-to-baseband pulsed-radar transceiver with applications in imaging and gesture recognition,” *IEEE Journal of Solid-State Circuits*, vol. 48, no. 4, pp. 1055–1071, 2013.

[58] X. Wu and K. Sengupta, “Dynamic waveform shaping for reconfigurable radiated periodic signal generation with picosecond time-widths,” in *2015 IEEE Custom Integrated Circuits Conference (CICC)*, 2015, pp. 1–4.

[59] C. Wang and R. Han, "Dual-terahertz-comb spectrometer on cmos for rapid, wide-range gas detection with absolute specificity," *IEEE Journal of Solid-State Circuits*, vol. 52, no. 12, pp. 3361–3372, 2017.

[60] T. Chi, M. Huang, S. Li, and H. Wang, "17.7 a packaged 90-to-300ghz transmitter and 115-to-325ghz coherent receiver in cmos for full-band continuous-wave mm-wave hyperspectral imaging," in *2017 IEEE International Solid-State Circuits Conference (ISSCC)*, 2017, pp. 304–305.

[61] Y. Zhu, H. Wang, K. Kang, and O. Momeni, "A low power sub-harmonic self-oscillating mixer with 16.8db conversion loss at 310ghz in 65nm cmos," in *2019 IEEE Custom Integrated Circuits Conference (CICC)*, 2019, pp. 1–4.

[62] Z. Hu, C. Wang, and R. Han, "A 32-unit 240-ghz heterodyne receiver array in 65-nm cmos with array-wide phase locking," *IEEE Journal of Solid-State Circuits*, vol. 54, no. 5, pp. 1216–1227, 2019.

[63] M. M. Assefzadeh, B. Jamali, A. K. Gluszek, A. J. Hudzikowski, J. Wojtas, F. K. Tittel, and A. Babakhani, "Terahertz trace gas spectroscopy based on a fully-electronic frequency-comb radiating array in silicon," in *2016 Conference on Lasers and Electro-Optics (CLEO)*, 2016, pp. 1–2.

[64] P. Hillger, J. Grzyb, R. Jain, and U. R. Pfeiffer, "Terahertz imaging and sensing applications with silicon-based technologies," *IEEE Transactions on Terahertz Science and Technology*, vol. 9, no. 1, pp. 1–19, 2019.

[65] B. Jamali, J. Zhou, and A. Babakhani, "Broadband spectroscopy of materials with an integrated comb-based millimeter-wave detector," in *2019 44th International Conference on Infrared, Millimeter, and Terahertz Waves (IRMMW-THz)*, 2019, pp. 1–2.

[66] R. Han and E. Afshari, "A cmos high-power broadband 260-ghz radiator array for spectroscopy," *IEEE Journal of Solid-State Circuits*, vol. 48, no. 12, pp. 3090–3104, 2013.

[67] R. Han, C. Jiang, A. Mostajeran, M. Emadi, H. Aghasi, H. Sherry, A. Cathelin, and E. Afshari, "25.5 a 320ghz phase-locked transmitter with 3.3mw radiated power and 22.5dbm eirp for heterodyne thz imaging systems," in *2015 IEEE International Solid-State Circuits Conference - (ISSCC) Digest of Technical Papers*, 2015, pp. 1–3.

[68] H. Jalili and O. Momeni, "17.10 a 318-to-370ghz standing-wave 2d phased array in 0.13µm bicmos," in *2017 IEEE International Solid-State Circuits Conference (ISSCC)*, 2017, pp. 310–311.

[69] H. Rahmani and A. Babakhani, "A 1.6mm^3 wirelessly powered reconfigurable fdd radio with on-chip antennas achieving 4.7 pj/b tx and 1 pj/b rx energy efficiencies

for medical implants," in *2020 IEEE Custom Integrated Circuits Conference (CICC)*, 2020, pp. 1–4.

[70] H. Rahmani and A. Babakhani, "A wirelessly powered reconfigurable fdd radio with on-chip antennas for multi-site neural interfaces," *IEEE Journal of Solid-State Circuits*, vol. 56, no. 10, pp. 3177–3190, 2021.

[71] G. Guimaraes and P. Reynaert, "29.6 a 660-to-676ghz 4×2 oscillator-radiator array with intrinsic frequency-filtering feedback for harmonic power boost achieving 7.4dbm eirp in 40nm cmos," in *2020 IEEE International Solid- State Circuits Conference - (ISSCC)*, 2020, pp. 450–452.

[72] H. Jalili and O. Momeni, "A 0.34-thz wideband wide-angle 2-d steering phased array in 0.13-μm sige bicmos," *IEEE Journal of Solid-State Circuits*, vol. 54, no. 9, pp. 2449–2461, 2019.

[73] Y. Tousi and E. Afshari, "A high-power and scalable 2-d phased array for terahertz cmos integrated systems," *IEEE Journal of Solid-State Circuits*, vol. 50, no. 2, pp. 597–609, 2015.

[74] C. Jiang, A. Cathelin, and E. Afshari, "A high-speed efficient 220-ghz spatial-orthogonal ask transmitter in 130-nm sige bicmos," *IEEE Journal of Solid-State Circuits*, vol. 52, no. 9, pp. 2321–2334, 2017.

[75] S. Kang, S. V. Thyagarajan, and A. M. Niknejad, "A 240 ghz fully integrated wideband qpsk transmitter in 65 nm cmos," *IEEE Journal of Solid-State Circuits*, vol. 50, no. 10, pp. 2256–2267, 2015.

[76] B. Hadidian, F. Khoeini, S. M. H. Naghavi, A. Cathelin, and E. Afshari, "A 220-ghz energy-efficient high-data-rate wireless ask transmitter array," *IEEE Journal of Solid-State Circuits*, pp. 1–1, 2021.

[77] L. Chen, S. Nooshabadi, A. Cathelin, and E. Afshari, "A compact 196 ghz fsk transmitter for point-to-point wireless communication with novel direct modulation technique," in *2021 IEEE Radio Frequency Integrated Circuits Symposium (RFIC)*, 2021, pp. 11–14.

[78] B. Jamali, D. Ramalingam, and A. Babakhani, "Intelligent material classification and identification using a broadband millimeter-wave frequency comb receiver," *IEEE Sensors Letters*, vol. 4, no. 7, pp. 1–4, July 2020.

[79] S. Jamison, J. Shen, D. Jones, R. Issac, B. Ersfeld, D. Clark, and D. Jaroszynski, "Plasma characterization with terahertz time–domain measurements," *Journal of applied physics*, vol. 93, no. 7, pp. 4334–4336, 2003.

[80] B. Kolner, R. Buckles, P. Conklin, and R. Scott, “Plasma characterization with terahertz pulses,” *IEEE Journal of Selected Topics in Quantum Electronics*, vol. 14, no. 2, pp. 505–512, 2008.

[81] I. H. Hutchinson, *Refractive-index measurements*, 2nd ed. Cambridge University Press, 2002, p. 104–154.

[82] T. N. Carlstrom, D. R. Ahlgren, and J. Crosbie, “Real-time, vibration-compensated co2 interferometer operation on the diii-d tokamak,” *Review of Scientific Instruments*, vol. 59, no. 7, pp. 1063–1066, 1988.

[83] M. A. Van Zeeland, R. L. Boivin, T. N. Carlstrom, T. Deterly, and D. K. Finkenthal, “Fiber optic two-color vibration compensated interferometer for plasma density measurements,” *Review of Scientific Instruments*, vol. 77, no. 10, p. 10F325, 2006.

[84] M. A. Van Zeeland, T. N. Carlstrom, D. K. Finkenthal, T. Akiyama, R. L. Boivin, A. Colio, D. Du, A. Gattuso, F. Glass, C. M. Muscatello, R. O’Neill, M. Smiley, J. Vasquez, M. Watkins, D. L. Brower, J. Chen, W. X. Ding, D. Johnson, P. Mauzey, M. Perry, C. Watts, and R. Wood, “Tests of a full-scale iter toroidal interferometer and polarimeter (tip) prototype on the diii-d tokamak (invited),” *Review of Scientific Instruments*, vol. 89, no. 10, p. 10B102, 2018.

[85] M. Heald and C. Wharton, *Plasma Diagnostics with Microwaves*, ser. Plasma Diagnostics with Microwaves. Wiley, 1965. [Online]. Available: https://books.google.com/books?id=SjBRAAAAMAAJ

[86] G. Neumann, U. Bänziger, M. Kammeyer, and M. Lange, “Plasma-density measurements by microwave interferometry and langmuir probes in an rf discharge,” *Review of Scientific Instruments*, vol. 64, no. 1, pp. 19–25, 1993.

[87] E. E. Scime, R. F. Boivin, J. L. Kline, and M. M. Balkey, “Microwave interferometer for steady-state plasmas,” *Review of Scientific Instruments*, vol. 72, no. 3, pp. 1672–1676, 2001.

[88] O. Tudisco, A. Lucca Fabris, C. Falcetta, L. Accatino, R. De Angelis, M. Manente, F. Ferri, M. Florean, C. Neri, C. Mazzotta, D. Pavarin, F. Pollastrone, G. Rocchi, A. Selmo, L. Tasinato, F. Trezzolani, and A. A. Tuccillo, “A microwave interferometer for small and tenuous plasma density measurements,” *Review of Scientific Instruments*, vol. 84, no. 3, p. 033505, 2013.

[89] W. Gekelman, P. Pribyl, Z. Lucky, M. Drandell, D. Leneman, J. Maggs, S. Vincena, B. Van Compernolle, S. K. P. Tripathi, G. Morales, T. A. Carter, Y. Wang, and T. DeHaas, “The upgraded large plasma device, a machine for studying frontier basic plasma physics,” *Review of Scientific Instruments*, vol. 87, no. 2, p. 025105, 2016.

[90] B. Jamali and A. Babakhani, “Wireless time transfer with subpicosecond accuracy based on a fully integrated injection-locked picosecond pulse detector,” *IEEE Transactions on Microwave Theory and Techniques*, vol. 68, no. 1, pp. 160–169, 2020.

[91] B. Jamali and A. Babakhani, “A fully integrated 30-to-160ghz coherent detector with a broadband frequency comb in 65nm cmos,” in *2019 14th European Microwave Integrated Circuits Conference (EuMIC)*, 2019, pp. 104–107.

[92] B. Jamali and A. Babakhani, “Sub-picosecond wireless synchronization based on a millimeter-wave impulse receiver with an on-chip antenna in 0.13μm sige bicmos,” in *2016 IEEE MTT-S International Microwave Symposium (IMS)*, 2016, pp. 1–4.

[93] J. Han, P. Pribyl, W. Gekelman, A. Paterson, S. J. Lanham, C. Qu, and M. J. Kushner, “Three-dimensional measurements of plasma parameters in an inductively coupled plasma processing chamber,” *Physics of Plasmas*, vol. 26, no. 10, p. 103503, 2019.

[94] J. Han, P. Pribyl, W. Gekelman, and A. Paterson, “Three-dimensional measurements of fundamental plasma parameters in pulsed icp operation,” *Physics of Plasmas*, vol. 27, no. 6, p. 063509, 2020.

[95] M. Gilmore, W. Gekelman, K. Reiling, and W. A. Peebles, “A reliable millimeter-wave quadrature interferometer,” 2020.

[96] J. S. Melinger, Y. Yang, M. Mandehgar, and D. Grischkowsky, “Thz detection of small molecule vapors in the atmospheric transmission windows,” *Opt. Express*, vol. 20, no. 6, pp. 6788–6807, Mar 2012.

[97] R. Wang, J. Q. Yao, D. G. Xu, J. L. Wang, and P. Wang, “The physical theory and propagation model of THz atmospheric propagation,” vol. 276, p. 012223, feb 2011.

[98] P. Baron, J. Mendrok, Y. Kasai, S. Ochiai, T. Seta, K. Sagi, K. Suzuki, H. Sagawa, and J. Urban, “Amaterasu: Model for atmospheric terahertz radiation analysis and simulation,” *Journal of the National Institute of Information and Communications Technology*, vol. 55, pp. 109–121, 03 2008.

[99] Y. Yang, M. Mandehgar, and D. R. Grischkowsky, “Understanding thz pulse propagation in the atmosphere,” *IEEE Transactions on Terahertz Science and Technology*, vol. 2, no. 4, pp. 406–415, 2012.

[100] M. Hosseini, M. Assefzadeh, S. Razavian, Y. Mehta, and A. Babakhani, “Terahertz channel characterization using a silicon-based picosecond pulse source,” in *2020 IEEE Radio and Wireless Symposium (RWS)*, 2020, pp. 76–79.

[101] S. Razavian, M. Hosseini, Y. Mehta, and A. Babakhani, “Terahertz channel characterization using a broadband frequency comb radiator in 130-nm sige bicmos,” *IEEE Transactions on Terahertz Science and Technology*, vol. 11, no. 3, pp. 269–276, 2021.

[102] A. Danylov, “Thz laboratory measurements of atmospheric absorption between 6% and 52% relative humidity,” *Submillimeter-Wave Technol. Lab., Univ. Massachusetts, Lowell, MA, USA*, pp. 1–7, 2006.

[103] E. Muehldorf, “The phase center of horn antennas,” *IEEE Transactions on Antennas and Propagation*, vol. 18, no. 6, pp. 753–760, 1970.

[104] J. F. Johansson and N. D. Whyborn, “The diagonal horn as a sub-millimeter wave antenna,” *IEEE Transactions on Microwave Theory and Techniques*, vol. 40, no. 5, pp. 795–800, 1992.

[105] I. Gordon, L. Rothman, C. Hill, R. Kochanov, Y. Tan, P. Bernath, M. Birk, V. Boudon, A. Campargue, K. Chance, B. Drouin, J.-M. Flaud, R. Gamache, J. Hodges, D. Jacquemart, V. Perevalov, A. Perrin, K. Shine, M.-A. Smith, and E. Zak, “The hitran2016 molecular spectroscopic database,” *Journal of Quantitative Spectroscopy and Radiative Transfer*, 07 2017.

[106] Y. Yang, M. Mandehgar, and D. R. Grischkowsky, “Broadband thz pulse transmission through the atmosphere,” *IEEE Transactions on Terahertz Science and Technology*, vol. 1, no. 1, pp. 264–273, 2011.

[107] G.-R. Kim, T.-I. Jeon, and D. Grischkowsky, “910-m propagation of thz ps pulses through the atmosphere,” *Opt. Express*, vol. 25, no. 21, pp. 25 422–25 434, Oct 2017.

[108] J. Ma, R. Shrestha, L. Moeller, and D. Mittleman, “Channel performance for indoor and outdoor terahertz wireless links,” *APL Photonics*, vol. 3, 02 2018.

[109] F. Moshirfatemi, “Communicating at terahertz frequencies,” Ph.D. dissertation, 2017.

[110] F. Kong, Y. Zhang, and R. Palmer, “Characterization of micro-Doppler radar signature of commercial wind turbines,” in *Radar Sensor Technology XVIII*, K. I. Ranney and A. Doerry, Eds., vol. 9077, International Society for Optics and Photonics. SPIE, 2014, pp. 349 – 356.

[111] L. Ren, Y. S. Koo, Y. Wang, and A. E. Fathy, “Noncontact heartbeat detection using uwb impulse doppler radar,” in *2015 IEEE Topical Conference on Biomedical Wireless Technologies, Networks, and Sensing Systems (BioWireleSS)*, 2015, pp. 1–3.

[112] H.-S. Cho, Y.-J. Park, and H.-K. Lyu, “Robust heart rate detection method using uwb impulse radar,” in *2016 International Conference on Information and Communication Technology Convergence (ICTC)*, 2016, pp. 1138–1142.

[113] H. Tabatabai, D. E. Oliver, J. W. Rohrbaugh, and C. Papadopoulos, “Novel Applications of Laser Doppler Vibration Measurements to Medical Imaging,” *Sensing and Imaging: An International Journal*, vol. 14, no. 1-2, pp. 13–28, Jun. 2013.

[114] J. Liu, C. Wang, Y. Chen, and N. Saxena, “Vibwrite: Towards finger-input authentication on ubiquitous surfaces via physical vibration.” New York, NY, USA: Association for Computing Machinery, 2017. [Online]. Available: https://doi.org/10.1145/3133956.3133964

[115] A. Jha, F. J. Azcona, and S. Royo, “Frequency-modulated optical feedback interferometry for nanometric scale vibrometry,” *IEEE Photonics Technology Letters*, vol. 28, no. 11, pp. 1217–1220, 2016.

[116] L. Scalise, Y. Yu, G. Giuliani, G. Plantier, and T. Bosch, “Self-mixing laser diode velocimetry: application to vibration and velocity measurement,” *IEEE Transactions on Instrumentation and Measurement*, vol. 53, no. 1, pp. 223–232, 2004.

[117] X. Cui, Q. Zhang, Y. Li, S. Li, D. Wu, C. Feng, and H. Ding, “Study of the temporal phase-shifting interferometry measurement under the Tokamak related vibration environment,” in *AOPC 2020: Optics Ultra Precision Manufacturing and Testing*, L. Kong, D. Zhang, and X. Luo, Eds., vol. 11568, International Society for Optics and Photonics. SPIE, 2020, pp. 404 – 409. [Online]. Available: https://doi.org/10.1117/12.2580207

[118] H. Song and J.-I. Song, “Terahertz-wave vibrometer using a phase-noise-compensated self-heterodyne system,” *IEEE Photonics Technology Letters*, vol. 28, no. 3, pp. 363–366, 2016.

[119] M. Geiger, D. Schlotthauer, and C. Waldschmidt, “Improved throat vibration sensing with a flexible 160-ghz radar through harmonic generation,” in *2018 IEEE/MTT-S International Microwave Symposium - IMS*, 2018, pp. 123–126.

[120] J. Guo, Y. He, C. Jiang, M. Jin, S. Li, J. Zhang, R. Xi, and Y. Liu, “Measuring micrometer-level vibrations with mmwave radar,” *IEEE Transactions on Mobile Computing*, pp. 1–1, 2021.

[121] X. Yi, C. Wang, X. Chen, J. Wang, J. Grajal, and R. Han, “A 220-to-320-ghz fmcw radar in 65-nm cmos using a frequency-comb architecture,” *IEEE Journal of Solid-State Circuits*, vol. 56, no. 2, pp. 327–339, 2021.

[122] F. Barbon, G. Vinci, S. Lindner, R. Weigel, and A. Koelpin, “A six-port interferometer based micrometer-accuracy displacement and vibration measurement radar,” in *2012 IEEE/MTT-S International Microwave Symposium Digest*, 2012, pp. 1–3.

[123] D. Molter, S. Weber, T. Pfeiffer, J. Klier, S. Bachtler, F. Ellrich, J. Jonuscheit, and G. von Freymann, “Interferometry-aided terahertz time-domain spectroscopy for robust measurements in reflection,” in *2018 43rd International Conference on Infrared, Millimeter, and Terahertz Waves (IRMMW-THz)*, 2018, pp. 1–2.

[124] J. Johnson, T. Dorney, and D. Mittleman, “Interferometric imaging with terahertz pulses,” *IEEE Journal of Selected Topics in Quantum Electronics*, vol. 7, no. 4, pp. 592–599, 2001.

[125] H. Rahmani, M. M. Archang, B. Jamali, M. Forghani, A. M. Ambrus, D. Ramalingam, Z. Sun, P. O. Scumpia, H. A. Coller, and A. Babakhani, “Towards a machine-learning-assisted dielectric sensing platform for point-of-care wound monitoring,” *IEEE Sensors Letters*, vol. 4, no. 6, pp. 1–4, 2020.

[126] M. Hosseini, M. Assefzadeh, S. Razavian, Y. Mehta, and A. Babakhani, “Terahertz channel characterization using a silicon-based picosecond pulse source,” in *2020 IEEE Radio and Wireless Symposium (RWS)*, 2020, pp. 76–79.

[127] D. Rodriguez and C. Li, “Sensitivity and distortion analysis of a 125-ghz interferometry radar for submicrometer motion sensing applications,” *IEEE Transactions on Microwave Theory and Techniques*, vol. 67, no. 12, pp. 5384–5395, 2019.

[128] X. Ma, Y. Wang, L. Lu, X. Zhang, Q. Chen, X. You, J. Lin, and L. Li, “Design of a 100-ghz double-sideband low-if cw doppler radar transceiver for micrometer mechanical vibration and vital sign detection,” *IEEE Transactions on Microwave Theory and Techniques*, vol. 68, no. 7, pp. 2876–2890, 2020.

[129] T. Jaeschke, C. Bredendiek, S. Küppers, and N. Pohl, “High-precision d-band fmcw-radar sensor based on a wideband sige-transceiver mmic,” *IEEE Transactions on Microwave Theory and Techniques*, vol. 62, no. 12, pp. 3582–3597, 2014.

[130] M. Pauli, B. Göttel, S. Scherr, A. Bhutani, S. Ayhan, W. Winkler, and T. Zwick, “Miniaturized millimeter-wave radar sensor for high-accuracy applications,” *IEEE Transactions on Microwave Theory and Techniques*, vol. 65, no. 5, pp. 1707–1715, 2017.

[131] T.-Y. J. Kao, A. Y.-K. Chen, Y. Yan, T.-M. Shen, and J. Lin, “A flip-chip-packaged and fully integrated 60 ghz cmos micro-radar sensor for heartbeat and mechanical vibration detections,” in *2012 IEEE Radio Frequency Integrated Circuits Symposium*, 2012, pp. 443–446.

[132] C. Zech, A. Hülsmann, M. Schlechtweg, S. Reinold, C. Giers, B. Kleiner, L. Georgi, R. Kahle, K.-F. Becker, and O. Ambacher, “A compact w-band lfmcw radar module with high accuracy and integrated signal processing,” in *2015 European Microwave Conference (EuMC)*, 2015, pp. 554–557.